EXPERIMENTAL ANALYSIS AND MODELING OF POROUS NiTi SHAPE MEMORY ALLOYS

by

Gülcan Özerim Bekiloğlu

B.S., Mechanical Engineering, Boğaziçi University, 2015

M.S., Mechanical Engineering, Boğaziçi University, 2017

Submitted to the Institute for Graduate Studies in
Science and Engineering in partial fulfillment of
the requirements for the degree of
Doctor of Philosophy

Graduate Program in Mechanical Engineering

Boğaziçi University

2022

ACKNOWLEDGEMENTS

First of all, I would like to express my sincere gratitude to my dear supervisor Prof. Günay Anlaş who guided me for my entire graduate life, and supported to realize this joint doctoral study. With many challenges and achievements, it was a great opportunity for my academic career. I would like to also thank my dear supervisor Prof. Ziad Moumni for his endless support during my doctoral project. It was an honor to work with them while being a part of this valuable collaboration between Boğaziçi University and Ensta Paris. I would like to thank Campus France, and their advisors, for their support to this collaboration.

I thank to the reviewers of my thesis Prof. Tarak Ben Zineb and Prof. Wael Zaki, and the jury members Prof. Hilmi Luş, Asst. Prof. Sertan Alkan, and Prof. Claude Stolz for their efforts and important contributions. It is an honor to receive the PhD degree by their consideration.

I am grateful to my colleagues Fatma Mutlu and Xiaofei Ju for their friendship and for sharing their experiences with me. I thank my friend Barış Telmen for his admirable solidarity that helped me a lot in many aspects of my project. I also thank our valuable research engineer, and friend, Nicolas Thurieau for guiding me during many experiments. I will always appreciate our departmental secretaries, Seher Yıldız and Özlem Ulufer Oral, for always being available and helpful. I would like to thank my lovely friends Gizem Aktaş, Betül Uysal and Adilhan Orta for making me feel their endless support although they were abroad. I also thank my friends Kübra Sekmen and Marine Bayard for making my life in France more valuable and memorable.

Finally, I would like to thank my lovely family. I thank my parents Zühre and Mehmet, my sisters Gökçen and Cansu, and my husband H. Eren Bekiloğlu a lot for always being supportive and understanding during the challenging Ph.D. period.

ABSTRACT

EXPERIMENTAL ANALYSIS AND MODELING OF POROUS NiTi SHAPE MEMORY ALLOYS

Porosity brings new features to NiTi SMAs, and raises its potential for biomedical applications. Although different techniques are provided in the literature for manufacturing porous NiTi samples, the subject is still open to further investigation to achieve superior shape memory characteristics. Based on this, the aim of the thesis is to analyze and model the mechanical behavior of porous NiTi SMAs. First, NiTi compacts were produced using spark plasma sintering. After sintering, because the samples did not show the expected pseudoelastic behavior, they were systematically subjected to heat treatment. The transformation behavior and the phase composition were analyzed using DSC and XRD. These characterization gave an insight to the micro-structure after heat treatment. Then, instrumented micro-indentation was carried out to measure the hardness that was altered by aging. Selected samples that were tested under uniaxial compression showed an enhancement in the pseudoelasticity of the SPSed NiTi that was heat-treated. In the modeling part, a macro-scale phenomenological model is proposed for the mechanical behavior of the porous NiTi by using poromechanics. The model considers the porous medium as a skeleton that consists of a solid matrix and connected porous space. The porosity is included as an internal state variable. Both the pseudoelastic and plastic deformations were considered. The phenomenological model was implemented into Abaqus through a UMAT, and validated using experimental results available in the literature, as well as the numerical results obtained from the unit cell (UC) technique used in this study. The model proposed in this thesis represents the mechanical behavior of porous SMAs with reasonable accuracy with a significant reduction in numerical cost when compared to the UC approach. The model can be especially useful in possible biomedical applications.

ÖZET

GÖZENEKLİ NiTi ŞEKİL HAFIZALI ALAŞIMLARININ DENEYSEL ANALİZİ VE MODELLENMESİ

Gözeneklilik, NiTi ŞHA'lara ek özellikler getirerek malzemenin biyomedikal uygulamalar için potansiyelini artırmıştır. Gözenekli NiTi parçaların üretimi için literatürde çeşitli teknikler sunulmakla birlikte şekil hafızası anlamında üstün özellikler elde etmek için daha fazla araştırmaya ihtiyaç vardır. Buna dayanarak, gözenekli NiTi ŞHA'ların mekanik davranışını analiz etmek ve modellemek amaçlanmıştır. İlk olarak, kıvılcım plazma sinterleme yöntemi ile sıkıştırılmış NiTi numuneleri üretilmiştir. Sinterlemeden sonra numuneler beklenen super-elastik davranışı göstermemiş ve sistematik olarak ısıl işleme tabi tutulmuşlardır. Faz dönüşüm özellikleri ve mikro bileşenler DSC ve XRD kullanılarak gözlemlenmiş, bu karakterizasyonlar mikro yapıya dair bir fikir vermiştir. Yaşlanma işlemi ile değişen malzeme sertliğini ölçmek için mikro sertlik ölçümü yapılmış ve belirli numuneler tek eksenli sıkıştırma altında test edilmiştir. Sinterlenmiş NiTi'nin süper-elastik davranışında bir iyileşme gözlemlenmiş ve de ısıl işlemin etkisi rapor edilmiştir. Tezin modelleme bölümünde, gözenekli ŞHA'ların mekanik davranışı için poromekanik yaklaşım kullanılarak makro ölçekli fenomenolojik bir model geliştirlmistir. Modelde, gözenekli ortam katı bir matris ve bağlantılı gözenekli boşluktan oluşan bir iskelet yapısı olarak kabul edilmiş ve gözeneklilik modele bir iç durum değişkeni olarak dahil edilmiştir. Hem süperelastik hem de plastik deformasyonlar modele dahil edilmiştir. Gözenekli ŞHA'ların davranışını Abaqus'te modellemek için bir kullanıcı tanımlı malzeme alt programı geliştirilmiştir. Model, literatürdeki deneysel sonuçlar ve bu çalışmada uygulanan birim hücre tekniğinden elde edilen sayısal sonuçlar kullanılarak doğrulanmış; gözenekli ŞHA'ların mekanik davranışı makul bir doğruluk ve birim hücre yaklaşımına kıyasla numerik maliyette önemli bir azalma ile temsil edilmiştir. Modelin ozellikle biyomedikal uygulamalarda oldukça yararlı olabileceği gösterilmiştir.

TABLE OF CONTENTS

LIST OF FIGURES

LIST OF TABLES

LIST OF SYMBOLS

A	Austenite
A_f	Austenite Finish Temperature
A_f^0	Austenite Finish Temperature at Zero Stress
A_s	Austenite Start Temperature
D	Dissipation
E	Elastic Modulus
E_A	Elastic Modulus of Austenite
E_M	Elastic Modulus of Martensite
F_i	Limit Functions
$\boldsymbol{I}$	Second Order Identity Tensor
$\boldsymbol{J}$	Jacobian Tensor
K	Bulk Modulus
$\boldsymbol{K}$	Stiffness Tensor
$\boldsymbol{K}_A$	Stiffness Tensor of Austenite
$\boldsymbol{K}_{eqv}$	Equivalent Stiffness Tensor
$\boldsymbol{K}_M$	Stiffness Tensor of Martensite
L	Lagrangian
M	Martensite
$\boldsymbol{M}$	Compliance Tensor
M_f	Martensite Finish Temperature
M_s	Martensite Start Temperature
s	Entropy
$\boldsymbol{s}$	Deviatoric Stress Tensor
T	Temperature
u	Internal Energy
T_0	Reference Temperature
V_0	Initial Volume
z	Martensite Volume Fraction

α	Thermal Expansion Coefficient
δ	Kronecker Delta
$\boldsymbol{\varepsilon}$	Strain Tensor
$\boldsymbol{\varepsilon}_A$	Local Strain Tensor of Austenite
$\boldsymbol{\varepsilon}_{el}$	Elastic Strain Tensor
$\boldsymbol{\varepsilon}_{eqv}$	Equivalent Strain Tensor
$\boldsymbol{\varepsilon}_M$	Local Strain Tensor of Martensite
$\boldsymbol{\varepsilon}_{ori}$	Orientation Strain Tensor
$\boldsymbol{\varepsilon}_{pl}$	Plastic Strain Tensor
$\boldsymbol{\varepsilon}_{tr}$	Transformation Strain Tensor
κ	Bulk Modulus
μ	Shear Modulus
ν	Poisson's Ratio
ρ	Density
$\boldsymbol{\sigma}$	Stress Tensor
$\boldsymbol{\sigma}^{'}$	Deviatoric Stress Tensor
σ_{AF}	Austenite Finish Stress
σ_{AS}	Austenite Start Stress
σ_{MF}	Martensite Finish Stress
σ_{MS}	Martensite Start Stress
σ_{RF}	Orientation Finish Stress
σ_{RS}	Orientation Start Stress
σ_{tr}	Transformation Stress
ϕ	Porosity
ϕ_0	Initial Porosity
ϕ_e	Eulerian Porosity
ϕ_l	Lagrangian Porosity
ψ	Helmholtz Free Energy
ψ_L	Constraint Potential

LIST OF ACRONYMS/ABBREVIATIONS

2D	Two Dimensional
3D	Three Dimensional
DSC	Differential Scanning Calorimetry
EDX	Energy Dispersive X-ray Spectroscopy
GSM	Generalized Standard Materials
HV	Vickers Hardness
ISV	Internal State Variable
MT	Mori-Tanaka
NiTi	Nitinol
PM	Powder Metallurgy
RMA	Return Mapping Algorithm
RVE	Representative Volume Element
SEM	Scanning Electron Microscopy
SLM	Selective Laser Melting
SMA	Shape Memory Alloy
SPS	Spark Plasma Sintering
UC	Unit-cell
UMAT	User Defined Material Subroutine
XRD	X-ray Diffraction

1. INTRODUCTION

1.1. Introduction and motivation

Shape memory alloys (SMAs) are a special group of materials that sustain large deformations through martensitic phase transformation between austenite (A) and martensite (M) solid phases. Among various compositions, Nickel-Titanium (NiTi) is the most widely used SMA [1, 2]. Similar to its dense form, the porous NiTi is expected to show a similar shape memory behavior. Therefore it is considered an attractive candidate for engineering applications such as aerospace and biomedical. In the literature, there is a particular interest in the biomedical applications of porous NiTi alloys. Bone fixation plates or screws, teeth root replacements, cervical and lumbar vertebral implantations are examples among numerous implant applications of porous NiTi alloys [3–7]. Figure 1.1 shows a commercial application of a cervical and a lumbar spine implants made of porous NiTi [7].

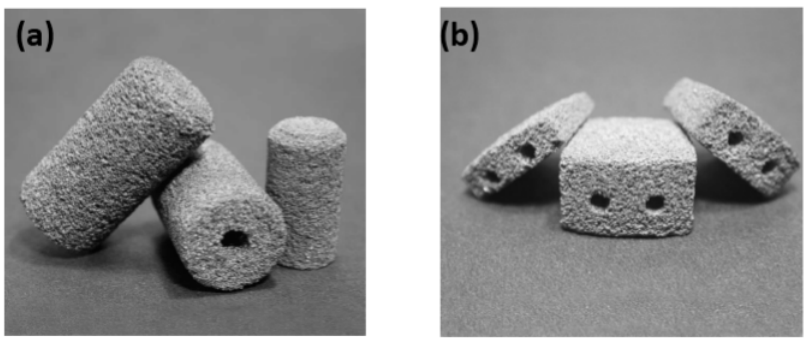

Figure 1.1: a) Cervical spine and b) lumbar spine implants made of porous NiTi [7].

An ideal material for a biomedical application must have mechanical properties that are similar to those of human body. Figure 1.2 shows the comparison of the stress-strain diagram of NiTi with human bone and tendon together with stainless steel, a widely used implant material. It is observed that NiTi's mechanical behavior is similar to the bone as a result of its pseudoelastic behavior. The pseudoelastic NiTi can sustain relatively large deofrmations and absorb a significant amount of energy.

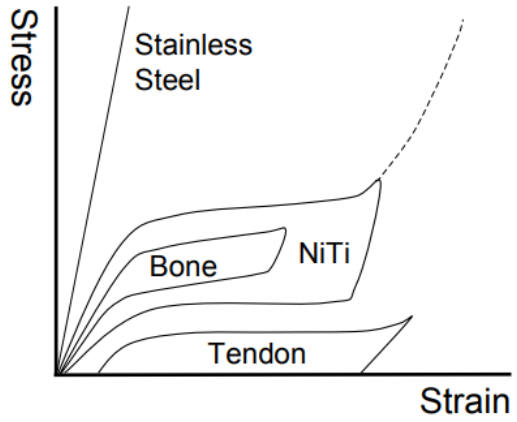

Figure 1.2: Stress-strain curves of stainless stell, NiTi, bone and tendon [7].

Porosity adds new features to the biocompatible NiTi, and increases its potential for hard-tissue implantation. The elastic modulus mismatch between a NiTi implant and the human bone may result in a severe problem that is called "stress shielding" (low transmission of the load from the implant to the bone tissue) and porosity is a way to overcome this problem. It also promotes cell in-growth and decreases the effective density, hence the mass of an implant body. Therefore, the mechanical performance of NiTi implants can be altered by controlling the amount of porosity, the size of the pores, shape, and distribution [4, 7].

NiTi alloys are manufactured using different techniques in either dense or porous form. Additive manufacturing is the cutting-edge technology to produce near net-shaped products, but, it is still possible to produce porous NiTis using conventional powder metallurgy (PM) techniques with a wide range of pore size and distribution [4, 8–11]. The most common techniques are Conventional Sintering (CS), Self-propagating High Temperature Synthesis (SHS), Hot Isostatic Pressing (HIP), Spark Plasma Sintering (SPS) and Metal Injection Molding (MIM) [4]. They differ from each other by the application of heat and pressure, and differences occur in the final microstructure. Powder metallurgy of NiTi alloys can be carried out from either elemental or pre-alloyed NiTi powder; the later one increasing the homogeneity of the final sample [4]. Despite its many advantages, the powder metallurgy processing of

NiTi also has some disadvantages such as the formation of a brittle oxide layer or the difficulty of producing dense samples. Although different techniques are available for manufacturing porous NiTi, the subject is still open to further investigation to achieve superior shape memory behavior. For example, obtaining the pseudoelastic behavior from a porous NiTi is important for biomedical applications. Based on this, the aim of the PhD thesis is to investigate and model the mechanical behavior of powder processed porous NiTi shape memory alloys, especially the pseudoelastic one. In this study, NiTi samples are manufactured using the powder metallurgy technique and they are subjected to various heat treatments to obtain the expected pseudoelastic behavior. The microstructure of the samples is analyzed and their mechanical behavior is studied. Based on the experimental observations obtained in this study and other studies in the literature, a new constitutive model is proposed to study the mechanical behavior of porous NiTi alloys.

1.2. Martensitic Transformation and Shape Recovery

Martensitic phase transformation is the origin of the unique behavior of NiTi shape memory alloys. It is a diffusionless thermoelastic transformation between austenite and martensite solid phases which have different crystal arrangements. Therefore, the shape change and recovery are the results of the change in the material's crystal structure [1].

Figure 1.3 is a good representation of the transformation paths between the parent austenite and the low-symmetry martensitic phases [12]. The martensite is the low temperature phase whereas the austenite is more stable above a certain temperature (A_f^0). The stress-free transformation from austenite to martensite under a thermal load is known as self-accommodation of martensite (path 1) in which all variants of martensite may coexist. This transformation does not create any macroscopic shape change. The martensite variants orient into a favorable direction if a mechanical load is applied, and return into the self-accommodated shape by unloading as shown by the paths 2 and 3. The stress or temperature values in the figure show the critical values

at which the austenite or martensite phases are thermodynamically stable. [1].

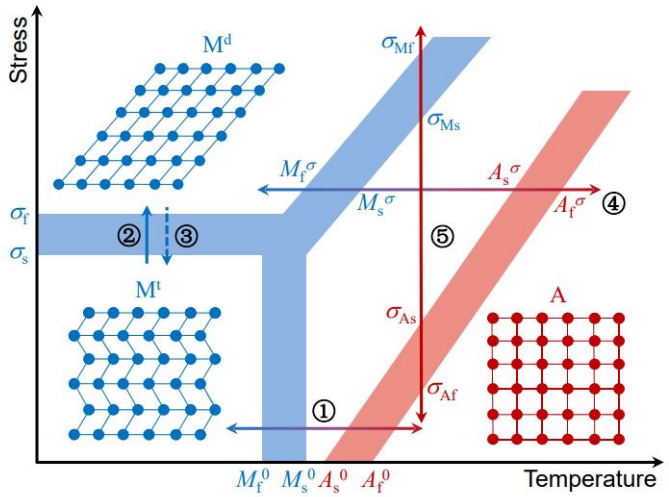

Figure 1.3: Schematic diagram of phase transformation [12].

The shape memory effect (SME) happens through a series of thermal or mechanical loading/unloading (paths 1-2-3-1 in Figure 1.3). An originally austenitic SMA is transformed into the self-accommodated martensite by decreasing the temperature without any macroscopic shape change (1). The self-accommodated martensite is then transformed into the oriented (detwinned) martensite above a certain stress (2) and then unloaded elastically where a macroscopic shape change is observed (3). If in this unloaded state, the temperature is increased above a critical value known as austenite finish temperature A_f^0, the oriented martensite is transformed back into the parent austenitic phase by recovering the whole deformation (1). This phenomenon is known as one-way shape memory effect. There is another phenomenon called two-way shape memory effect (path 4 in Figure 1.3) for which the material is trained to remember its shape in the martensitic phase as well. The two-way shape memory effect is not studied in this thesis, however, further information can be found in the literature [1, 13–15].

Another important behavior of the NiTi SMA is the pseudoelastic one (path 5 in Figure 1.3) which is observed through a stress induced martensitic transformation given that the temperature of the material is higher than or around A_f^0. Above A_f^0, the initially austenitic material starts to deform elastically up to a certain stress value after

which the phase transformation starts and continues gradually until full martensite is achieved. The martensitic phase can further be deformed elastically; if the material is unloaded before reaching the yield point, the deformation is totally recovered although the loading and unloading paths differ from each other as shown in Figure 1.4. σ^{Ms}, σ^{Mf}, σ^{As} and σ^{Af} represent the start and the finish stresses of forward (from A to M) and reverse (from M to A) martensitic transformations, respectively.

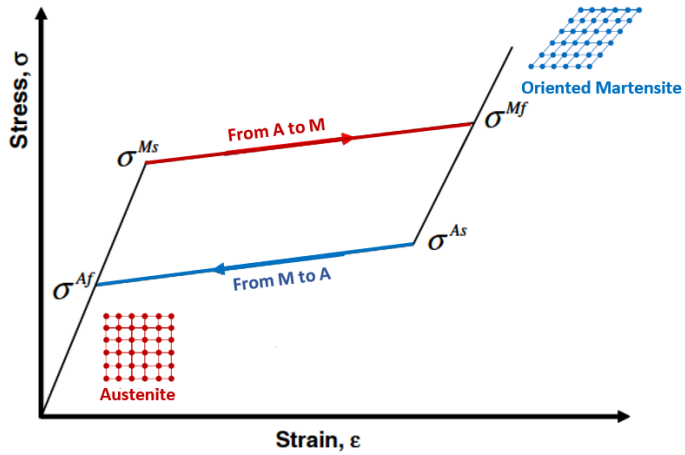

Figure 1.4: Representation of pseudoelastic stress-strain diagram.

It must be noted that the pseudoelastic behavior is not readily observed in NiTi alloys. There are two important factors that affect the pseudoelastic behavior. One is the austenite finish temperature, and the other one is the yield strength of the alloy. The yield strength must be high enough to prevent the material from plastic deformation before the martensitic transformation takes place [16]. It is shown in the literature, and in this study that plastic deformation may accompany the martensitic transformation. Therefore, NiTi alloys are post-processed by different techniques such as cold work, annealing, or aging to control [1,16] to increase the resistance of the alloy to plastic deformation.

1.3. Mechanical Behavior of Porous NiTi Alloys

Pores have significant effects on the mechanical properties of NiTi alloys such as stiffness or strength. The main reason behind this is attributed to the stress concentration and the reduced loading area due to pores [7,17]. In a porous SMA, the martensitic transformation takes place in some micro-regions around pores, hence resulting in early transformation of the austenite and martensite. There are several experimental studies showing the differences in the effective stiffness and the strength [17–25]. Figure 1.5 provides experimental results from the literature for the Young's modulus and compressive strength of porous NiTis compared to human bone. Both decreases with increasing porosity and approaches to the elastic modulus and the strength of the bone. Experimental and numerical studies have shown that the relationship between the porosity and the stiffness and strength can be represented by a polynomial fit.

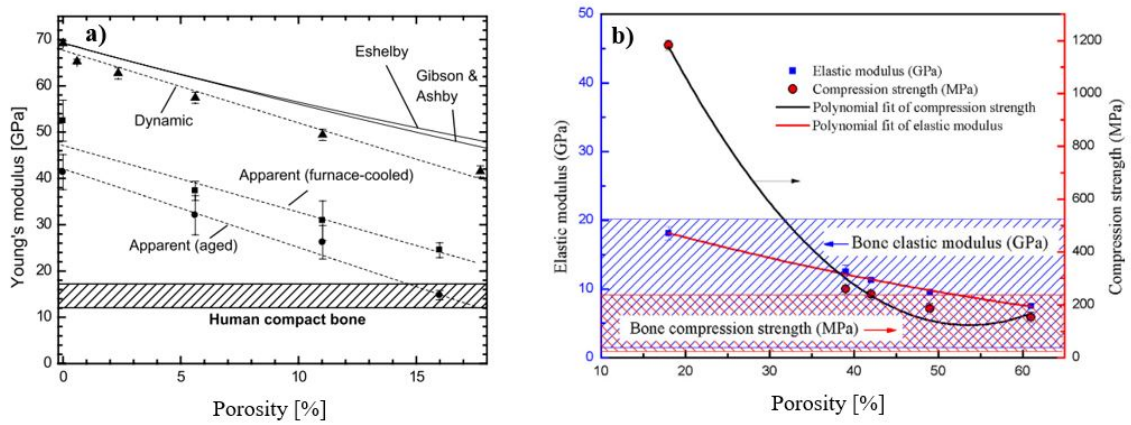

Figure 1.5: Effect of porosity on the elastic modulus and the compressive strength of NiTi alloys studied by a) Greiner et al. [25] and b) Zhang et al. [30].

Porous SMAs are generally investigated under uniaxial compression because they are mainly exposed to compressive loading in biomedical applications. Zhao et al. [19] performed the pioneering works, and studied the mechanical behavior of 13% and 25% porous NiTi samples produced by spark plasma sintering. The samples were tested under uniaxial compression. The stress plateau shifted down and the slope of the elastic portion decreased with increasing porosity. It is also stated that the amount of

phase transformation decreases with increasing porosity due to a weak interconnection between NiTi powders. Similarly, Greiner et al. [25] reported a pseudoelastic behavior in 6-16% porous NiTi alloys that depended on heat treatment. Lagoudas et al. [24] investigated NiTi samples with 40-50% porosity under uniaxial compression, a gradual phase transformation was observed from austenite to martensite which manifested itself by a gradual change in the tangent modulus of the stress-strain curve. Chen et al. [26] fabricated NiTi samples of different porosity (%2.7-%36) by using conventional sintering and they reported a non-linearity in pseudoelastic loops and attributed this to the elastic buckling of cell walls. A similar result was achieved by Li et al. [27] for the uni-axial compression of the %37.3 and %44.5 porous samples which were produced by conventional sintering using temporary space holders; there was no stress plateaus during forward and reverse transformations.

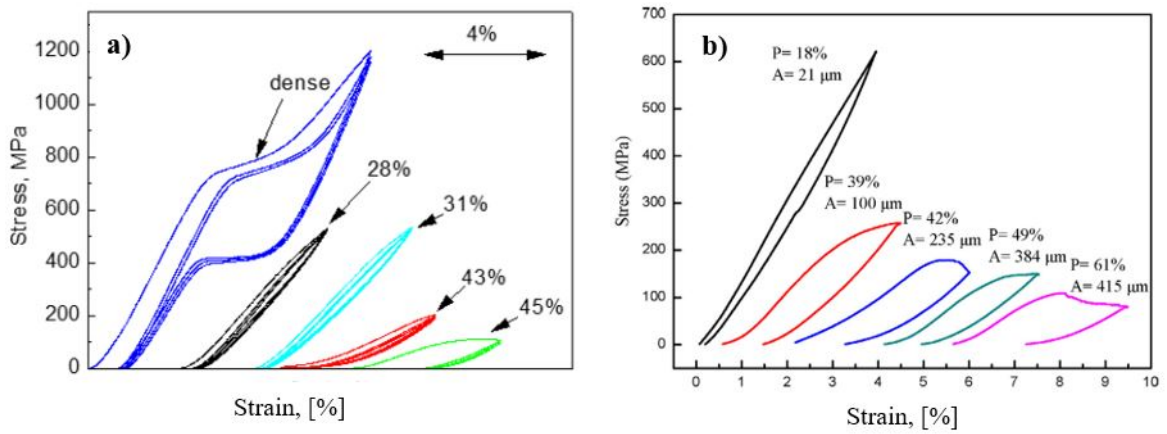

Figure 1.6: Uni-axial compression of NiTi alloys obtained by a) Yuan et al. [7], b) Zhang et al. [30].

In addition to the martensitic transformation, porous SMAs may undergo simultaneous plastic deformation at lower nominal stresses compared to dense SMAs [20, 21, 25, 28, 29]. Figure 1.6 shows the stress-strain diagrams of NiTi specimens with varying porosity [7, 30]. The recoverable strain decreases with increasing porosity and applied loading: for example, the 30% porous material recovers around 4% strain which significantly reduces when the porosity is increased to 45%.

In the literature, there are different approaches to model the effective (equivalent) behavior of porous SMAs. Some researchers have used micro-mechanical averaging techniques by considering pores as inclusions in the dense SMA matrix [31–35]. They approximated the constitutive behavior by different homogenization techniques. In some studies, finite element method is employed; a unit-cell consisting of an empty space and a SMA matrix is loaded [28, 36–38]. The matrix part is modeled using previously developed constitutive models for the SMAs. Different boundary conditions are applied depending on the symmetry of the problem. A single unit cell or series of unit cells are used to represent global behavior. Some researchers performed a numerical reconstruction of porous structures to represent random distribution of pores [39–41]. The pores are introduced into the finite element models as low or almost zero-stiffness elements or as voids with specific geometries. These techniques give good estimates of the global stress-strain, and they are especially useful to observe the deformation around pores. However, the UC models bring a significant computational cost depending on the UC geometry and the number of elements [38].

There are a few phenomenological models that investigate the mechanical behavior of porous SMAs. In general, the phenomenological models that are originally developed for metallic foams are modified [42, 43]. Yield functions are derived by considering a macroscopic, inelastic volumetric strain which is observed due to the effect of hydrostatic pressure. Deshpande et al. [42] are the early researchers who experimentally studied the yielding of metallic foams and who proposed a new yield criterion that depends on the first two stress invariants, namely the equivalent and mean stresses. Ashrafi et al. [44] implemented the yield function proposed by Deshpande et al. [42] into a phenomenological model for porous SMAs within the framework of irreversible thermodynamics. Their model was validated using computational results obtained from a 3D finite element analysis with low stiffness elements representing porosity. The model was later developed by including the plasticity, and the results were compared to some experimental results in the literature, and a good agreement was obtained [45]. Similarly, Olsen and Zhang [46] proposed the Gurson [47] type yield function for the phase transformation and the plastic deformation in porous SMAs. Cisse et al. [38]

developed a phenomenological constitutive model for architectured cellular iron based shape memory alloys (AC Fe-SMAs) in the framework of generalized standard materials with internal constraints [48]. The strain tensor is decomposed into hydrostatic and deviatoric components for both the phase transformation and the plastic deformations, and the yield functions are modified accordingly. More recently, Viet et al. [49] developed a phenomenological model based on the ZM SMA model [15]. Their model includes a damage parameter which introduces the effect of porosity on the stiffness and the hardening of the material.

1.4. Objectives and Outline

The potential of porous NiTi SMAs to be used in biomedical applications has been clearly studied in the literature. Their commercial applications are still limited when compared to applications of Titanium or stainless steel due to the complex thermo-mechanical behavior and/or high post-processing cost of NiTi alloys [50]. For this reason, the fabrication and processing of porous NiTi alloys have attracted great interest from scientists. In this study, the aim is to investigate the phase transformation characteristics of NiTi samples prepared by powder metallurgy and to develop a macroscopic phenomenological model which describes the mechanical behavior of porous NiTi alloys, especially the pseudoelastic one. The thesis is organized as follows:

Chapter 2 provides information about the fabrication of NiTi compacts through spark plasma sintering. The NiTi compacts are subjected to various heat-treatments to observe changes on their microstructure, hence to observe the phase transformation of the SPSed NiTi. A systematic investigation has been provided by using calorimetric and microscopic analyzes. It is shown that the SPSed NiTi samples respond to heat treatment similar to dense ones provided in the literature; the phase transformation temperatures and the sequence are altered by homogenization and aging. The experimental results provided in Chapter 2 provide a significant basis to understand the mechanical response of the material which is discussed in Chapter 3. In Chapter 3, the micro-indentation and uni-axial compression tests are presented, and the material

is analyzed from the pseudoelastic and the shape memory point of view. The SPSed and heat treated NiTi has shown very good SME while the pseudoelastic strain recovery was partial. The pseudoelastic behavior of the heat treated samples are compared in different categories, and the heat treatment-pseudoelasticity relation of the SPSed samples is discussed.

In Chapter 4, a new phenomenological model is proposed for the mechanical behavior of porous NiTi alloys. Starting from an SMA model developed by Zaki and Moumni [15,51] and by using the poromechanics approach developed by O. Coussy [52], the new effective model includes the porosity as an additional internal state variable. The phenomenological model accounts for phase transformation and plasticity; it is implemented into Abaqus through a user-defined material subroutine (UMAT), and used to study the uni-axial stress-strain response of porous NiTi samples from literature. The global response is captured in a great extent, and further simulation is performed to show model capabilities.

In Chapter 5, the uni-axial behavior of the porous NiTi alloys is studied with the unit-cell method. The phenomenological SMA model of Zaki and Moumni [15, 51] is implemented into Abaqus to model the solid part of the unit-cells. The simulations obtained with the unit-cell method are then used to make a numerical validation of the effective (equivalent) phenomenological model which is developed in this study. In addition, the modeling approaches presented in Chapter 4 and Chapter 5 are compared. Chapter 6 outlines conclusions of the present work and suggestions for future direction.

2. FABRICATION, HEAT TREATMENT AND CHARACTERIZATION OF SPARK PLASMA SINTERED NiTi ALLOY

This chapter presents the fabrication, heat treatment and characterization of NiTi compacts. The samples were prepared using spark plasma sintering and then were subjected to a wide range of heat treatment to observe the changes in the microstructure and the phase transformation. The transformation characteristics were obtained from differential scanning calorimetry (DSC); phase composition was identified using X-ray diffraction (XRD), and the results were supported with scanning electron microscopy (SEM) and energy dispersive X-ray analysis (EDX). In general, the SPSed NiTi responded to homogenization and aging similar to the bulk NiTi in the literature. Transformation temperatures were altered and different transformation paths among austenite, martensite and R-phases were observed as a results of heat treatment.

2.1. Introduction

In the literature, most of the works on the SPS processed NiTi alloys focus on densification and microstructural (phase) evaluation [53–57] while studies on the mechanical behavior, especially on the pseudoelasticity and shape memory effect, are limited. For the pseudoelastic response, NiTi must be loaded at a temperature around its critical austenite finish temperature (A_f), and the yield strength must be high enough to prevent plastic deformation [16]. Both criteria depend on the phase composition. After sintering, NiTi compacts are cooled in a large temperature interval which results in uncontrolled formation of secondary phases such as Ti_2Ni, Ti_3Ni_4 or $TiNi_3$, and an important contribution to the pseudoelastic behavior comes from the precipitation of Ti_3Ni_4 [1, 58]. Homogeneous and coherent precipitation of Ti_3Ni_4 increases the resistance against plastic deformation by the internal stress field generated around precipitates [1,16,59–62]. Therefore, SPSed NiTi samples need post thermal treatment to control the microstructure, hence the phase transformation characteristics.

In the literature, there are a few studies in which the pseudoelastic behavior of spark plasma sintered NiTi alloys is shown. Zhao et al. [19] have produced NiTi samples using SPS starting from pre-alloyed Ti-50.9 at.% Ni powders. Their dense and 13% porous samples showed a pseudoelastic stress-strain loop under uniaxial compression after a short time aging (30 minutes at 320°C then water quenched). Similar sintering and heat treatment processes were repeated by Nemat-Nasser et al. [63] who observed similar results with 12% porous sample. Later, Butler et al. [64] produced highly dense NiTi wires through spark plasma sintering and extrusion starting from fine elemental powders. Although their as-SPSed samples showed transformation peaks in differential scanning calorimetry (DSC), they applied 15 minutes of aging at 500°C which resulted in the expected pseudoelastic behavior under tension. Soba et al. [65] sintered elemental Ni-Ti powders by mixing them with TiO_2 powders to increase the strength. The sintered compacts with 99.9% relative density were then hot extruded, solutionized at 1000°C, and aged at 500°C for an hour. The heat treated bars were then tested under uniaxial tension up to 3% maximum strain; although there were no clear stress plateau during unloading, a 100% strain recovery was achieved. Lately, Salvetr et al. [66] studied the influence of heat treatment on the microstructure and the mechanical properties of a spark plasma sintered NiTi alloy, testing the specimens under high strain rate compression, and comparing their ultimate compressive strengths; but there was no discussion of the pseudoelastic behavior.

Previous works show that spark plasma sintered NiTi is expected to show a pseudoelastic loop similar to the one seen from bulk NiTi up to $12-13\%$ porosity [19, 63–65]. With increasing porosity, however, the pseudoelastic response starts to differ and the recovery from deformation decreases [21, 22, 30, 67–69]. Either highly dense or porous, the SPSed NiTi is heat treated to enhance its pseudoelastic behavior, and there is a need to discuss the effect of heat treatment on its pseudoelastic behavior. The pseudoelastic behavior of NiTi alloys processed by hot isostatic pressing (HIP) and selective laser melting (SLM) has been studied by McNeese et al. [70] and Saedi et al. [71] respectively. But there is no work in the literature on the heat-treatment-pseudoelasticity relation of SPSed NiTi, especially the effect on the full recovery from

strain. In this chapter, the characterization of heat treated NiTi compacts are provided while the heat treatment-pseudoelasticity relation is discussed in Chapter 3.

2.2. Spark Plasma Sintering

When spark plasma sintering (SPS) is applied to metallic powders it provides rapid fabrication compared to other sintering techniques such as conventional sintering (CS), hot isostatic pressing (HIP) or self-propagating high temperature synthesis (SHS) [4]. During SPS, powders are consolidated through simultaneous application of heat and pressure; the temperature is uniformly increased through pulsed DC current along with uniaxial pressure applied through graphite dies [55, 72]. In this work, pre-alloyed Ti-50.7 at.% Ni powder of 100-150 µm nominal diameter (purchased from TLS Technik GmbH, Bitterfeld Germany) was consolidated using DR SINTER Fuji 515-S LAB Spark Plasma Sintering as shown in Figure 2.1. The powder was placed in a graphite die covered with graphite paper, heated in a vacuumed chamber at 100°C/min rate, held at the target temperature for 5 minutes, and then cooled down to room temperature.

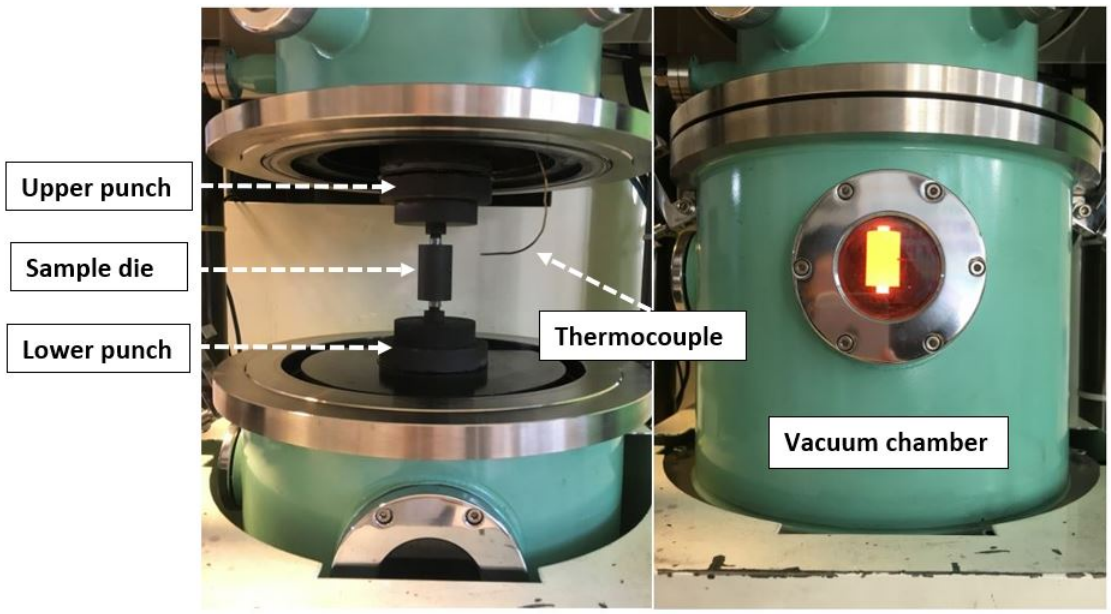

Figure 2.1: Spark plasma sintering setup.

Table 2.1 shows sintering parameters, the range of final dimensions and porosity. Average porosity, f_p, of cylindrical compacts were calculated using $f_p = 1 - m/(\rho V)$ where m is the powder mass, $\rho_{NiTi} = 6.45$ g/cm^3 is the theoretical density of bulk NiTi, and V is the end volume of a cylinder.

Table 2.1: Sintering parameters, resulting dimension and porosity of cylindrical compacts.

	High density compact	Low density compacts			
Powder mass (g)	5.50	5.00	4.55	4.13	6.45
Mold diameter (mm)	8	8	8	8	10
Punch pressure (MPa)	60	60	60	60	38
Target temperature (°C)	1000	850	700	560	560
Duration at target temp. (min)	5	5	5	5	5
Final Length (mm)	17	16	15.3	15.9	18
Average porosity (%)	< 1	3.58	8.23	19.84	29.23

The sintering temperature and pressure were determined from the literature: Zhao et al. [19] have reported dense compacts by sintering NiTi powders of similar size at 850°C, 50 MPa for 5 minutes. However, when compared to the sintering parameters and the resulting porosity provided by Zhao et al. [19], in this work, remarkably higher temperature and pressure (1000°C, 60 MPa) were required to decrease the porosity in this work. Zhao et al. [19] did not share the dimensions of the sintering mold which are known to affect the sintering parameters, resulting porosity and microstructure [73].

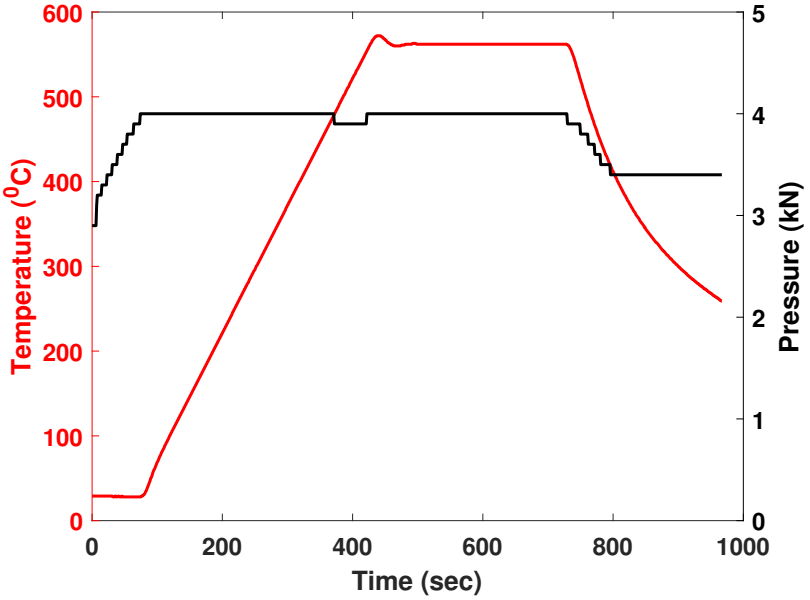

Figure 2.2: Sample pressure and temperature profile recorded during sintering.

The average porosity increases significantly by decreasing the temperature or pressure: a porosity level up to 29% was achieved by changing the sintering parameters as shown in Figure 2.2. Figure 2.3 shows the optical microscope image of the sample with 29% average porosity. Boundaries of the powders are still visible as a result of weak sintering at low temperature and pressure.

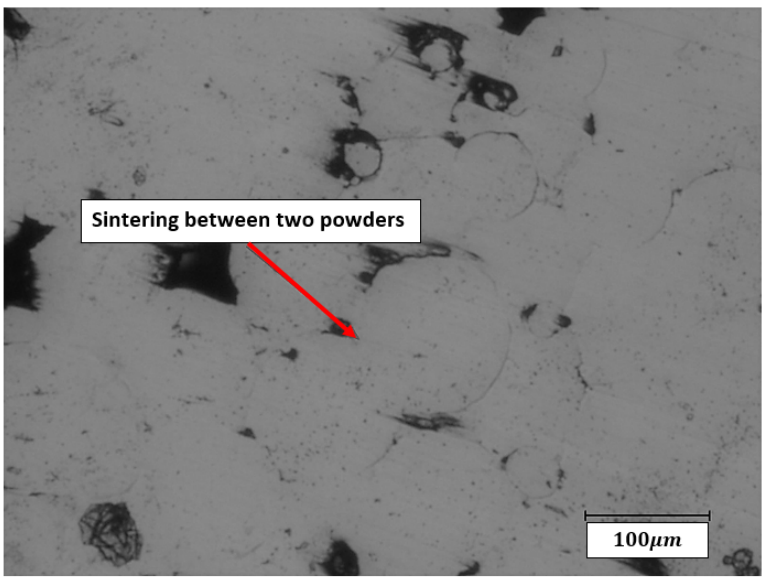

Figure 2.3: Optical microscope image of the sintered NiTi with 29% global porosity.

2.3. Heat Treatment and Calorimetric Analysis

Heat treatment is a series heating and cooling processes applied on metals and alloys to achieve desired properties by altering the microstructure. For NiTi alloys, heat treatment is an effective way of controlling the phase transformation characteristics and the strength, hence the mechanical behavior of the alloy. Figure 2.4 shows the phase diagram of Ni-Ti binary system. The main interest is around the center region where the equi-atomic composition is bounded by Ti_2Ni and $TiNi_3$ phases. It is also shown that there is a meta-stable intermediate phase, Ti_3Ni_4, which appears after a short time aging of NiTi between $300 - 600°C$, and plays a significant role on NiTi's pseudoelastic behavior [1].

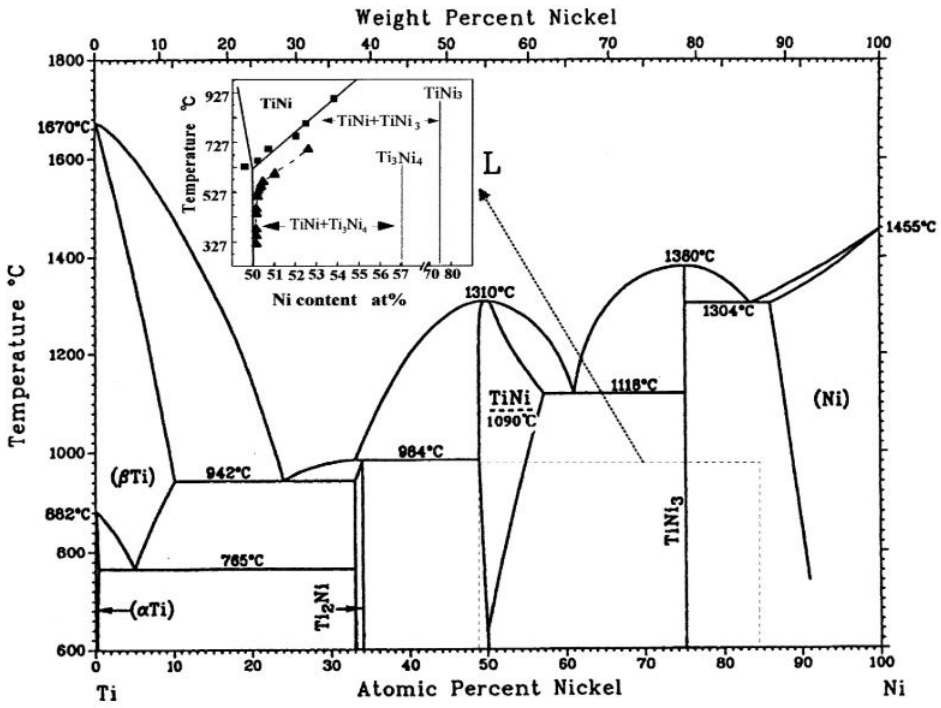

Figure 2.4: Phase diagram of Ni-Ti alloy [1].

In this study, high density NiTi samples were subjected to different combinations of homogenization and aging to observe the changes on phase transformation characteristics and the pseudoelastic behavior. The target of **homogenization** is to dissolve possible secondary phases or precipitates (e.g. Ti_2Ni, $TiNi_3$ and Ti_3Ni_4) that may

form during sintering, thereby better controlling the aging process. Subsequent **aging** of NiTi alloys enhances the pseudoelastic behavior if a coherent precipitation of Ti_3Ni_4 in small sizes is achieved [59, 62].

From NiTi compacts, $20-60$ mg samples were cut for heat treatment and calorimetric tests. They were either first homogenized at 1000°C and then aged, or directly aged between $320-600$°C in an oven operated under air. The heat treatment categories that were used for the calorimetric analyzes are listed below:

- 1 h of direct aging in $320-500$°C temperature range,
- 2 h of homogenization and then 1 h of aging in $350-600$°C temperature range, 2 h of homogenization and then aging from 30 minutes to 3.5 h at 500°C,
- 5 h of homogenization and then 24 h of aging at 350°C.

After either homogenization or aging, the samples were water quenched using tap water, and then mechanically polished using 500 grit silicon-carbide papers. Effect of heat treatment on transformation temperatures and paths were studied with a Setaram-131 differential scanning calorimeter at 10°C/min heating and cooling rate according to ASTM F2004-17 [74].

First, DSC plot of powders is plotted in Figure 2.5 where multi step transformation is observed during both heating and cooling. A literature survey made for multi-step transformation of NiTi powders showed that it was encountered by many researchers, and it was attributed to differences in the powder size or uneven composition [75–79]. It is known that a small deviation in the Ni concentration for NiTi alloys with more than 50.5 at.% Ni results in significant changes in transformation temperatures [1, 80]. In our study, Ni concentration of the powder was 50.7 at.%, and the powder size differed between 100-150 micrometers. The transformation peak which is observed around $25°C$ during heating may also result from an R-phase transformation, however it was not detected by the X-ray diffraction analysis of the powders performed around that temperature; the XRD spectrum of the powders matched perfectly with

austenite and martensite phases (see in section 2.4). Therefore, this multi-step transformation of powders is attributed to sources of heterogeneity as outlined above. The powders are expected to be a mixture of austenite and martensite phases around room temperature.

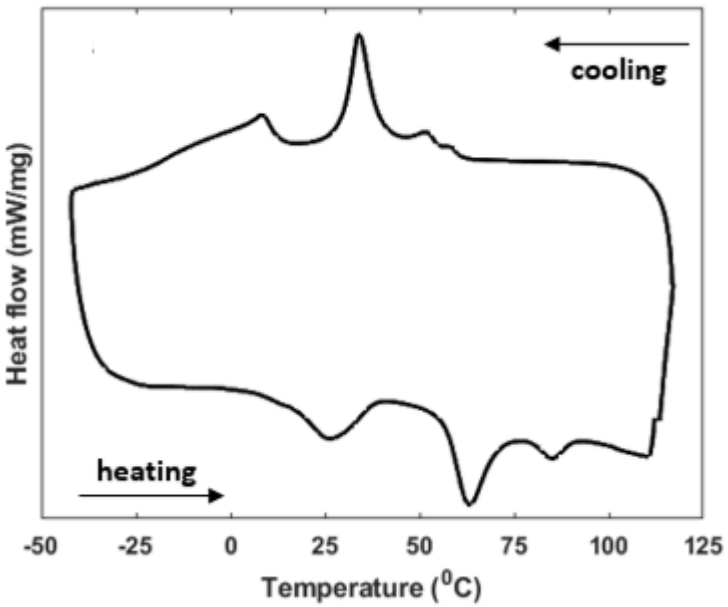

Figure 2.5: DSC plot of powders.

DSC plots of sintered and heat treated samples are shown in Figures 2.6, 2.7 and 2.8. The alloy that was not heat treated exhibited weak transformation peaks as shown in Figure 2.6; the austenite finish temperature was expected to be higher than 80°C. The sintered alloy was subjected to a 30 min. of direct aging. Zhao et al. [19] and Nemat-Nasser et al. [63] observed the full pseudoelastic behavior from a similarly heat treated spark plasma sintered pre-alloyed Ti-50.9 at.% Ni powder under uniaxial compression. As seen in Figure 2.6, the material tested in this study did not show any clear transformation peak after the same treatment. Figure 2.6 shows the evolution in the DSC plots up to 1 h aging at different temperatures. The phase transformation peaks become visible by 1 h aging at 350°C. When the aging temperature was increased from 350°C to $400 - 500$°C, the phase transformation was more pronounced. The transformation curve is wavy and continues gradually in a large temperature interval when compared to the DSC plots of the samples that were first homogenized and then

aged as presented in Figure 2.7. This type of multi-step transformation of NiTi was explained by a inhomogenous distribution of Ti_3Ni_4 precipitates and other phases in the literature [59, 61].

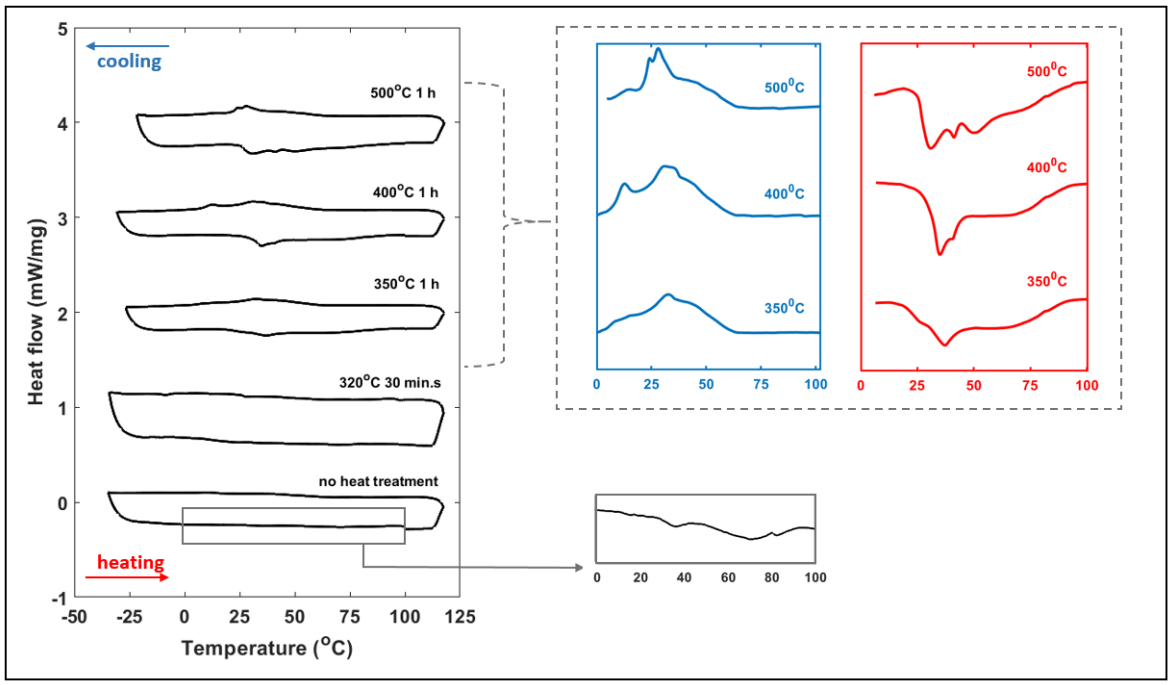

Figure 2.6: DSC plots of the samples subjected to direct aging treatment. (Curves of no heat-treated sample and the material after aging for 30 min. at 320°C are shown for comparison).

DSC plots of the samples that were first homogenized for 2 h and then aged for an hour in a 350-600°C temperature range are provided in Figure 2.7. After 2 h of homogenization, two distinct transformation peaks (one in the heating range, another one in the cooling range) were observed in the DSC plot which is typical for bulk NiTi alloys that are not subjected to aging treatment. Under certain temperature and duration, aging promotes the R-phase transformation that manifests itself with a small temperature hysteresis between forward and reverse transformation peaks on the DSC plot [59, 62, 81]. DSC results obtained from the samples which were aged between $350 - 500$°C after 2 h of homogenization exhibited the characteristic transformation peaks between austenite and R-phases which were more clearly visible on the DSC plot of the sample corresponding to aging at 500°C. The R-phase formation through

aging is expected until around 600°C according to the phase diagram of NiTi [1]. The DSC plot corresponding to 2 h of homogenization plus 1 h of aging at 600°C showed one-step transformation between austenite and martensite phases similar to the only homogenized one, (this result is consistent with the literature [1,62,81]). 350°C, 400°C and 450°C aging temperatures did not show significant changes in the DSC plots: their transformation peaks were found to be in the temperature range of $20-40$°C, and mainly one-step transformation between austenite and R-phases was observed. At 500°C aging temperature, a second transformation peak indicating the transformation from R-phase to martensite was detected near the lower temperature edge, however, the peak intensity was small to recognize in Figure 2.7.

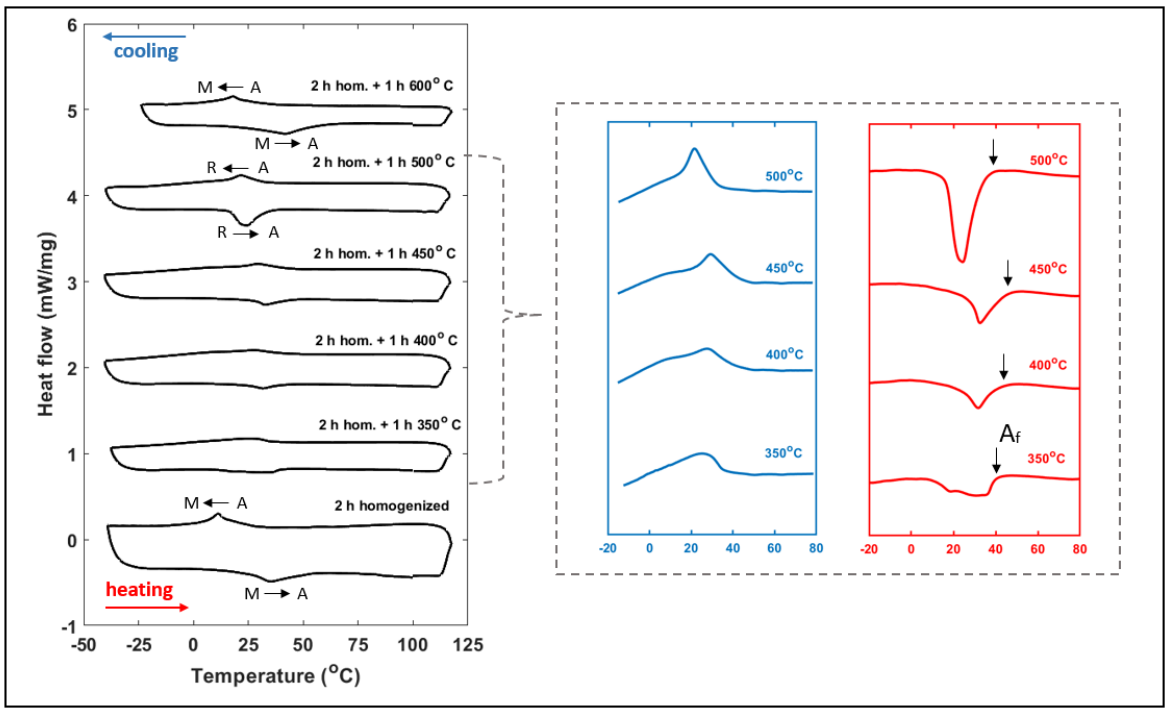

Figure 2.7: DSC plots of the samples subjected to 2 h of homogenization and then 1 h of aging treatment. The small vertical arrows indicate the austenite finish temperature (A_f).

Figure 2.8 shows the evolution of transformation peaks with time while keeping the aging temperature at 500°C. After 2 h of aging, the second transformation peak from R-phase to martensite became more pronounced. This two stage transformation

behavior that was initially observed in cooling also appeared in heating by increasing the aging time to 3.5 h. In addition, the A_f temperature significantly increased by 3.5 h of aging (around 25 °C) at 500°C. This result was attributed to a possible decrease in the Ni concentration of the matrix due to the growing size of Ti_3Ni_4 precipitates by increasing the aging time. The increase in the precipitate size when aging NiTi alloys at 500°C was reported by Gall et al. [60] and Aboutalebi et al. [81] earlier.

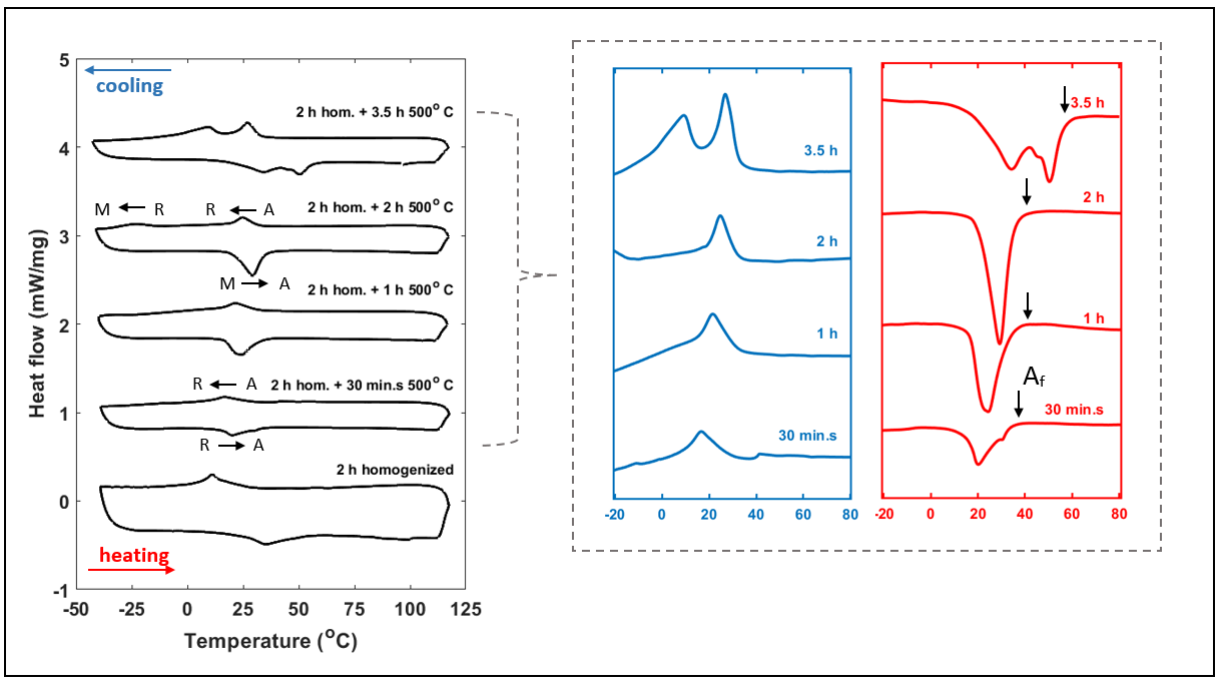

Figure 2.8: DSC plots of the samples subjected to 2 h of homogenization and then aging at 500°C by varying time. The small vertical arrows indicate the austenite finish temperature (A_f).

It is known that more secondary phases may dissolve into the matrix by increasing the homogenization time [82]. In some studies, longer homogenization or aging of NiTi alloys are performed [82–84]. After 5 h of homogenization, transformation peaks disappeared from the DSC plot as shown in Figure 2.9 and the material did not undergo any phase transformation in the studied temperature range. Figure 2.9 also shows the DSC plot obtained from the sample that was aged for 24 h at 350°C after homogenization. The A_f temperature was found to be around 55°C which is significantly higher than the ones obtained from the samples subjected to short time homogenization and

aging treatments. The evolution of the phases by increasing the aging time from 1 to 24 h is discussed in the following sections.

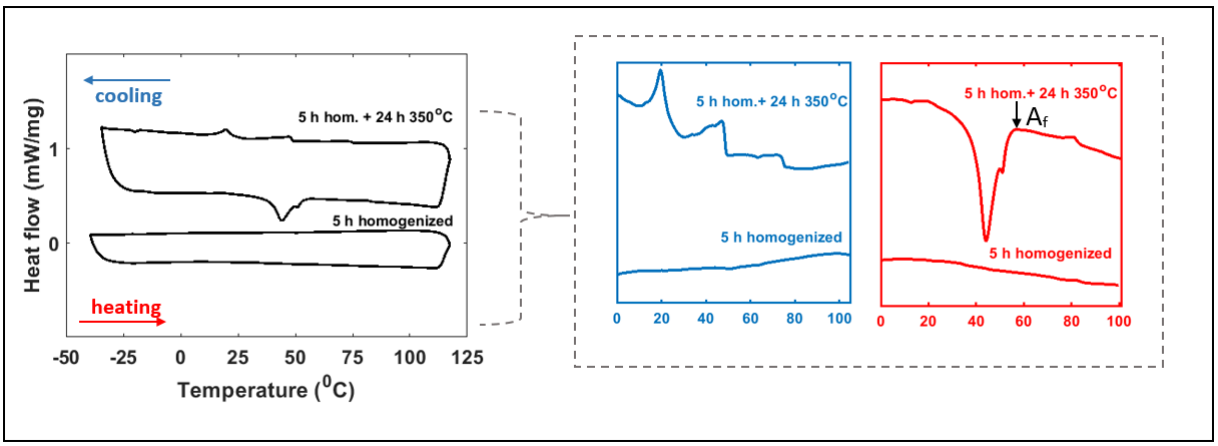

Figure 2.9: DSC plots of the samples subjected to 5 h of homogenization and then 24 h of aging at 350°C (The fluctuation around 75°C on the upper DSC plot in blue was attributed to an experimental noise that has been observed a few other times with the same DSC equipment.).

2.4. Phase Identification Through X-Ray Diffraction, SEM and EDX

Phase composition of the samples were further analyzed using X-ray diffraction, scanning electron microscopy (SEM) and energy dispersive X-ray analysis (EDX). A Rigaku D/MAX-Ultima X-ray diffraction (XRD) equipment with a Cu-K_α anode was used around room temperature (20-25°C) in the range of 0° to 90° 2θ. Figure 2.10 shows the X-ray diffraction pattern of the initial powder. A mixture of the austenite-martensite phases was expected around room temperature according to the DSC plot in Figure 2.5. The XRD pattern of the powder matched perfectly with the theoretical austenite and martensite peaks; there was no impurity in the starting material.

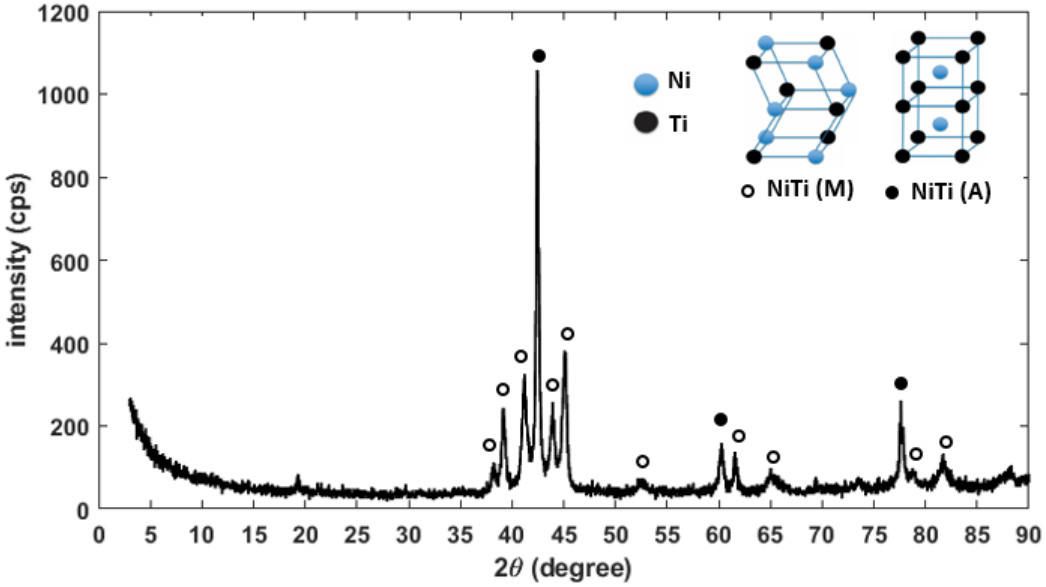

Figure 2.10: X-ray diffraction pattern of powder.

Figures 2.11 and 2.12 show the phase composition of the as-sintered sample by X-ray diffraction and scanning electron microscopy (SEM). Only the main peak area between 40-45 2θ was shown for a better focus. The XRD spectrum of the as-sintered sample revealed the presence of austenite and martensite phases together at room temperature. Twinned structure of the martensite was visible in the SEM image in Figure 2.12, dark gray spots observed under SEM were matched with Ti_2Ni ($Ti_4Ni_2O_x$) phase as presented in the literature [65, 70, 79, 85, 86] which was also supported by the results of energy dispersive X-ray analysis (EDX). The composition of the matrix was found to be Ti-49.8 at.% Ni while the composition of the dark gray spots was Ti-38at.%Ni which is very close to the theoretical atomic composition of Ti_2Ni. These regions were assumed to be a Ni-rich solution of Ti_2Ni phase. Ti_2Ni was also detected by XRD with a low intensity as shown in Figure 2.11, no Ti_3Ni_4 nor $TiNi_3$ phases were detected by XRD.

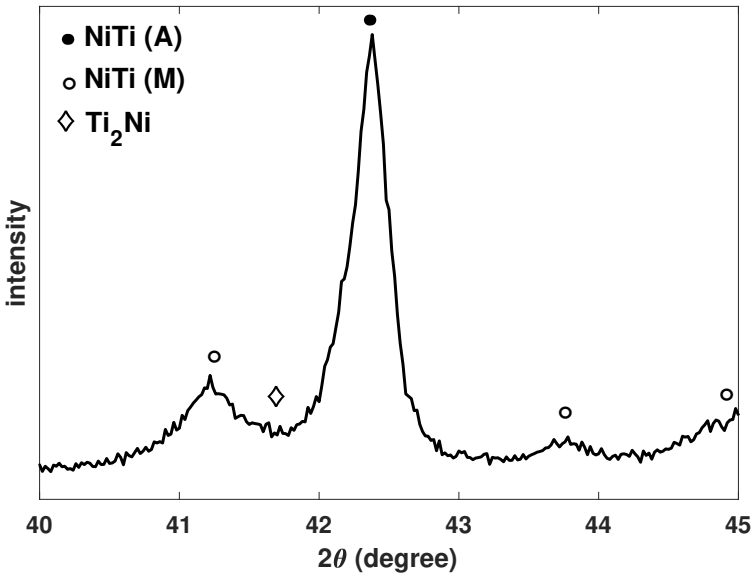

Figure 2.11: X-ray diffraction pattern of as-sintered sample.

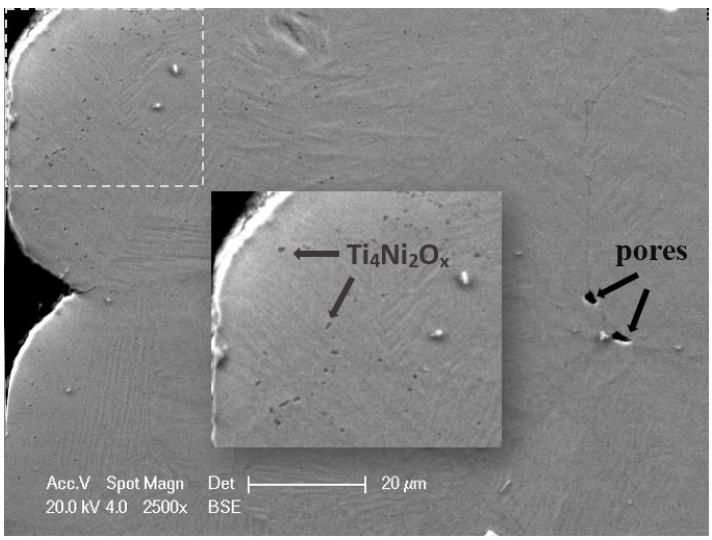

Figure 2.12: SEM image of as-sintered sample.

XRD results of the heat treated samples are presented in Figures 2.13-2.15. Figure 2.13 shows a sharp decrease in the main austenite peak after 1 h of direct aging when compared to the XRD spectrum of the as-sintered specimen. The DSC plots in Figure 2.6 show that the samples are expected to be a mixture of different phases (austenite, martensite and R-phases) at around room temperature, with a low austenite fraction. The slight XRD peak which showed up near 42° might be due to both a small fraction

of the austenite phase [87] or R-phase diffraction that occurs between 42-43° [88, 89]. On the other hand, there was not much difference in the XRD spectrum of the directly aged samples.

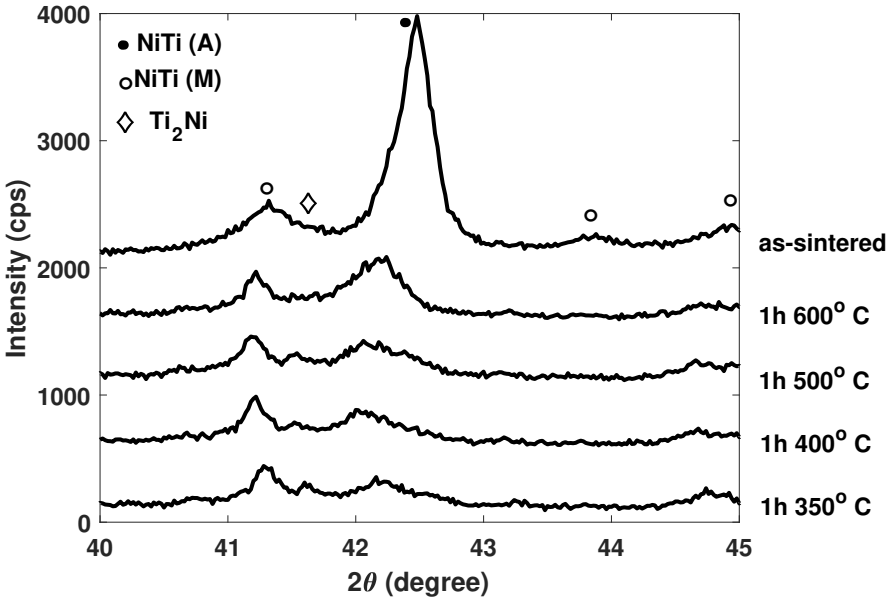

Figure 2.13: X-ray diffraction patterns of samples subjected to 1 h of direct aging.

Figure 2.14 shows XRD patterns obtained from the samples subjected to 2 h of homogenization plus 1 h of aging in the temperature range of $350 - 600$°C. The XRD spectrum of the sample that was only homogenized contains austenite and martensite main phases with a high austenite intensity. The sample that was first homogenized and then aged at 600°C yielded a similar XRD spectrum. It is consistent with the results obtained from the DSC study; both samples were mainly in the austenitic phase at room temperature. The samples that were subjected to aging between 350-500°C were expected to be a mixture of austenite and R-phases according to their DSC plots in Figure 2.7. The XRD analysis also detected martensite peaks. It was shown in the literature that XRD can detect smaller volume fraction of phases when compared to thermal analyzes [90]. In general, XRD spectrum of the samples that were homogenized and then aged by 1 h at $350 - 400 - 500$°C were close, there was no secondary phase detected other than Ti_2Ni.

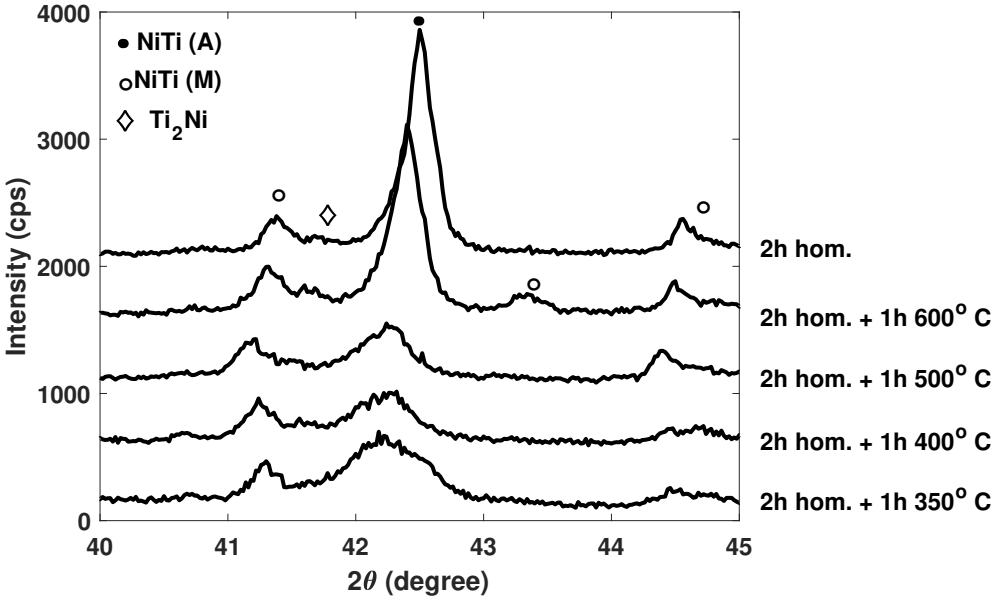

Figure 2.14: X-ray diffraction patterns of samples subjected to 2 h of homogenization and 1 h of aging.

Figure 2.15 shows evolution of the XRD spectrum by increasing the heat treatment duration at 350°C constant aging temperature. The samples were subjected to 5 h of homogenization and then aging for 1, 5, 18 and 24 h. After 5 h of homogenization, there were austenite and martensite phase peaks in the XRD spectrum. There was an evident increase in the intensity at the peak locations of free Ni element after 1-5 h of aging. The increase of the intensity and a relative angular shift of the peak location around 44.6° was attributed to a possible Ni release into the matrix. By increasing the aging time to 18-24 h, the intensity decreased, and a peak splitting was observed between 42-43° indicating the R-phase formation, a possible outcome of Ti_3Ni_4 precipitation in Ni-rich NiTi alloys achieved by heat treatment [59, 88].

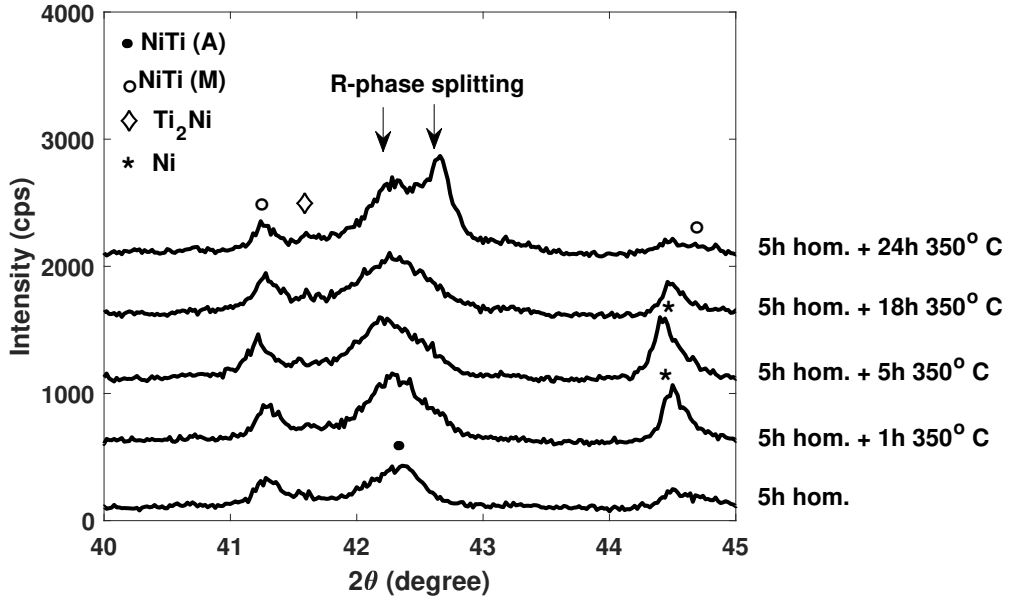

Figure 2.15: X-ray diffraction patterns of samples subjected to 5 h of homogenization and aging at 350°C for different duration.

2.4.1. Surface Oxidation

For biomedical applications of NiTi alloys, the release of Ni is an important concern since it may cause toxic or allergic reactions in the human body. Generally, a thin surface oxide layer prevents excessive Ni release into the body and protects the NiTi structure from corrosion [91]. Thermal oxidation in the air or water results in such an oxide layer over the NiTi surface. In the literature, formation of the oxide layer, and its effects on the corrosion behavior of the NiTi are studied by some researchers [91–93]. It is shown that oxidation takes place at both elevated temperatures around 1000°C and around 300-600°C at which shape setting of NiTi SMAs is performed [92, 94, 95].

In addition to the corrosion resistance, surface oxidation has other outcomes. Figure 2.16 shows the SEM image of the cross-section of a sintered sample after it was subjected to a thermal treatment (5 h of homogenization at 1000°C and 24 h aging at 350°C). EDX analysis reveals the Ti-based oxidation, and resulting composition layers along the sample's edge. A significant oxidation due to the long-time heat treatment

resulted in Ti depletion through the sample. The thin layer of Ni-rich $TiNi_3$ phase is explained by this mechanism.

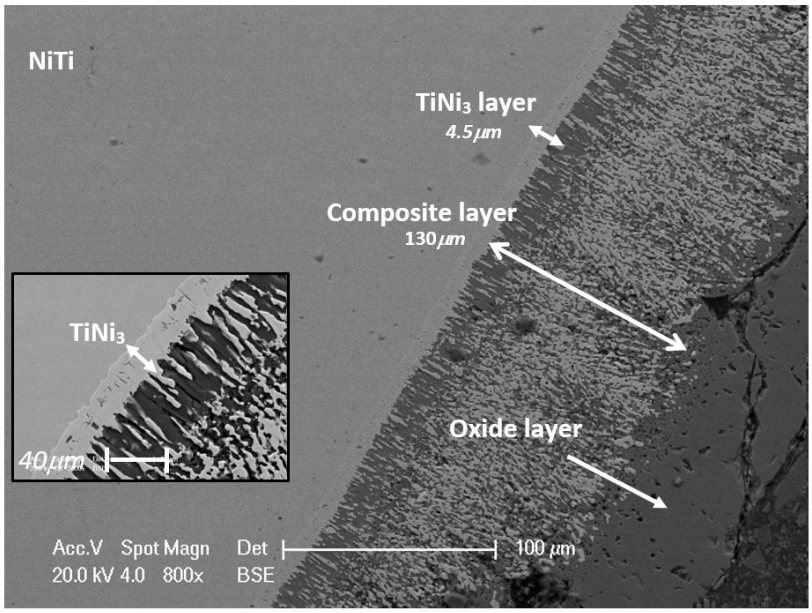

Figure 2.16: Cross-section of the sample subjected to 5 h of homogenization and 24 h aging at 350°C. Image taken from SEM.

SEM and EDX analyzes reveal the presence of a composite layer between the inner $TiNi_3$ and the outer oxide layers. Figure 2.17 shows EDX measurements at different points inside the composite layer. EDX has detected Ti_2Ni (point A) which is usually found in oxide form, and solid solution of Ni with Ti (point B: ∼92 at.% Ni and ∼6 at.% Ti). These results are found in accordance with the results provided by Mahmud et al. [93]. Different compositions around the NiTi matrix due to heat treatment were also presented in their work.

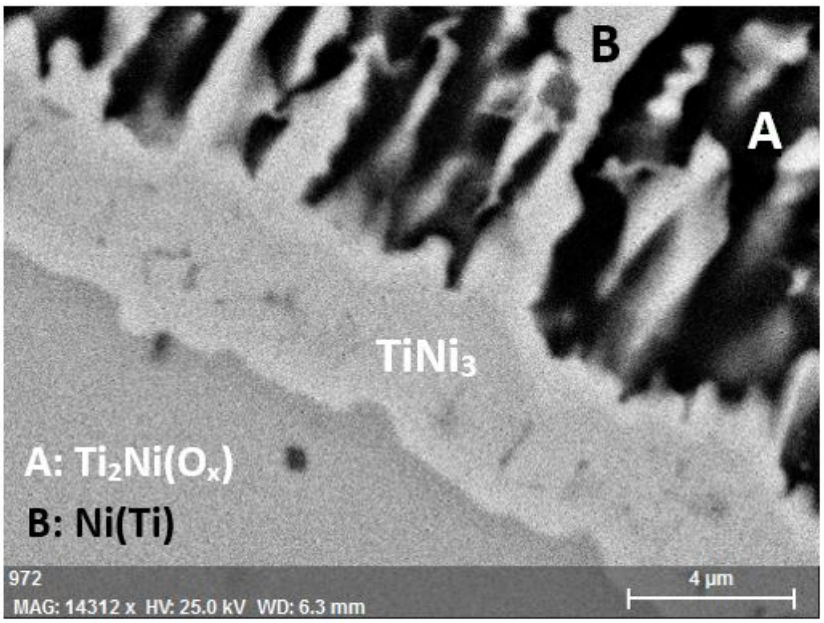

Figure 2.17: Composition changes near the composite layer of the sample subjected to 5 h of homogenization and 24 h aging at 350°C.

Although the oxide, composite and $TiNi_3$ layers are very thin when compared to the NiTi matrix, Mahmud et al. [93] has shown that Ti depletion may continue gradually through the center of the matrix depending on the time and the temperature of thermal exposure. They showed that after 24 h of heating at 1000°C, there were no phase transformation. Although it was not investigated in this thesis, the sample that was homogenized at 1000°C for 5 h is susceptible to have a significant zone affected by the oxidation.

2.5. Conclusions

In this chapter, a systematic study to observe the effects of thermal treatment on the microstructure of NiTi samples fabricated by spark plasma sintering was provided. The SPSed NiTi responded to homogenization and aging similar to bulk NiTi; changes in the transformation sequence among austenite, martensite and R-phases were observed in the results of DSC and XRD. The DSC plots showed significant heterogeneity for the samples subjected to direct aging without prior homogenization. The

homogenized samples resulted in more distinct transformation peaks.

In general, DSC plots of the samples that were subjected to short time homogenization and aging treatments showed typical R-phase transformation peaks that are observed in aged hardened NiTi alloys. The R-phase formation was clearly detected by the XRD plot of the sample which was subjected to 5 h of homogenization and then 24 h of aging at 350 °C. Studies in the literature show that Ti_3Ni_4 precipitation is an expected outcome of aging in Ni-rich NiTi alloys. Although the X-ray diffraction could not detect Ti_3Ni_4 precipitates, the form of the DSC plots supported the R-phase formation which is a natural outcome of precipitation by aging. According to other works found in the literature, XRD may not detect the precipitates when they are in a very small size. The age hardening mechanism is also investigated in Chapter 3. The experimental results presented in this chapter provide a significant basis to understand the mechanical response of the alloy which is presented in Chapter 3.

3. MECHANICAL BEHAVIOR OF THE SPARK PLASMA SINTERED NiTi ALLOY

After the heat treatment and microscopic evaluation, the NiTi samples are further analyzed in terms of the mechanical behavior: they are tested under instrumented micro-indentation and uni-axial compression. The psesudoelastic strain recovery of the samples increased after heat treatment, but in general the material has shown partial-pseudoelastic behavior which is associated to low Ni concentration of the matrix. On the other hand, a very good shape memory effect was observed from each category of heat treatment. The residual strain at the end of the martensitic orientation experiment was mostly recovered by heating up the specimens above A_f. The indentation measurements have shown that the age hardening mechanism was effective on the SPSed NiTi samples when there is prior homogenization.

3.1. Introduction

High yield strength is one of the criteria for the pseudoelastic behavior of NiTi alloys [1, 16]. Hardness measurements through instrumented micro-indentation are used to observe the effect of heat treatment on the strength of the SPSed NiTi alloy. According to the results found in literature, aging has an effect on the hardness of NiTi alloys by two main reasons. First, Ti_3Ni_4 precipitates alter the transformation temperatures by changing the Ni concentration of the matrix. As the difference between martensite start temperature and the test temperature increases, the resistance to martensitic transformation is enhanced, hence the increase of hardness. On the other hand, hardness is maximum at a small precipitate size. Therefore, assessment of hardness measurements must be done by considering both the martensitic phase transformation and the age hardening mechanisms [60, 62, 96].

In this chapter, SPS processed and heat-treated NiTi samples are investigated in terms of their mechanical behavior. The samples were subjected to instrumented micro-

indentation to observe the effect of heat treatment on the hardness which is known to have a significant effect on the pseudoelastic behavior. Later, the samples were tested under uni-axial compression to observe the stress-strain responses during both the martensitic orientation and pseudoelastic deformation. The stress-strain response of the alloy as a result of different heat treatment is discussed in the following sections.

3.2. Instrumented Micro-indentation

Hardness measurements were carried out using a Ficherscope-HM2000 instrumented micro-indentation equipment with a diamond Vickers indentor. The sintered samples were cut into small sizes, hot mounted using an epoxy resin, and then mechanically polished starting with grit papers followed by diamond pastes until 1 µm final polish prior to testing. Indentation was performed at ambient temperature, around 27°C, where the samples were mostly in a mixed austenite - martensite or R-phase structure according to their DSC results. Load was increased from zero to 1000 mN in 20 s, and then decreased to zero at the same speed.

Figure 3.1 shows the indentation profile between edges of a sample which was subjected to 5 h of homogenization. The indents near the edges of the sample are visibly smaller than the interior ones; the reason might be the oxidation during long time homogenization of the sample in the air atmosphere. SEM-EDX observations presented in Chapter 2 reveal the changes in the composition near the sample edges. For that reason, the samples were indented at 10 random points; average Vickers hardness and percent of recovered energy were recorded. Measurements were performed in three categories: 1 h aged samples, 2 h homogenized and then 1 h aged samples, and finally the samples aged at 350°C for different duration. Hardness and energy recovery ratio are provided in Figures 3.2-3.4.

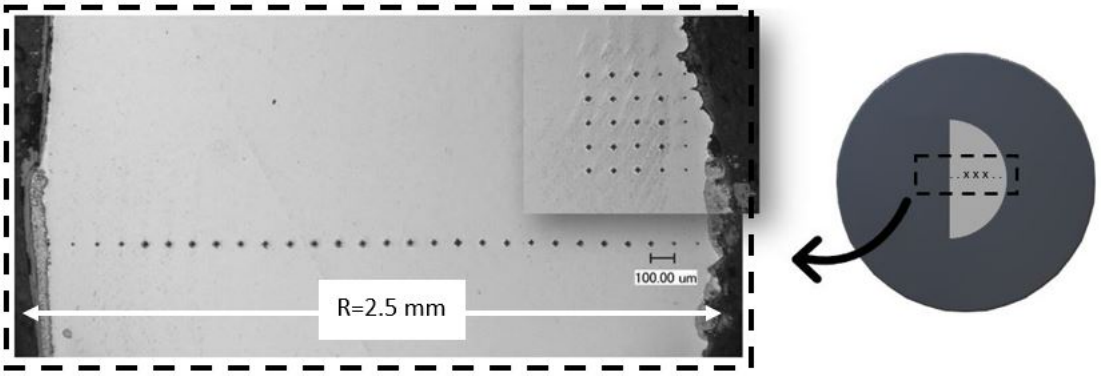

Figure 3.1: Indentation profile on 5 h homogenized sample.

As shown in Figures 3.2-3.4, hardness and energy recovery follow the same trend in every heat treatment category; higher hardness accompanies higher energy recovery ratio. In general, average Vickers hardness and energy recovery ratios were found to be in the range of 200-250 HV and $\%25-35$ respectively except for one sample which was subjected to long-time homogenization and aging at 350°C. Hardness of the as-sintered sample ($\sim$ 250 HV) was in the same order with NiTi alloys that were loaded to the same level in other studies. However, larger deviations were observed in the measurements of some specimens when compared to the ones provided in the literature [60, 71].

After 1 h of direct aging, there was no increase in the hardness compared to the as-sintered specimen as shown in Figure 3.2. It was at a maximum at 400°C aging temperature, as well as the percent of recovered energy. However, it is difficult to explain the differences in the hardness measurements of the samples in this group; first, it is unclear which phase was dominant during indentation of the samples by looking at their DSC plots, and their XRD spectrum were very close.

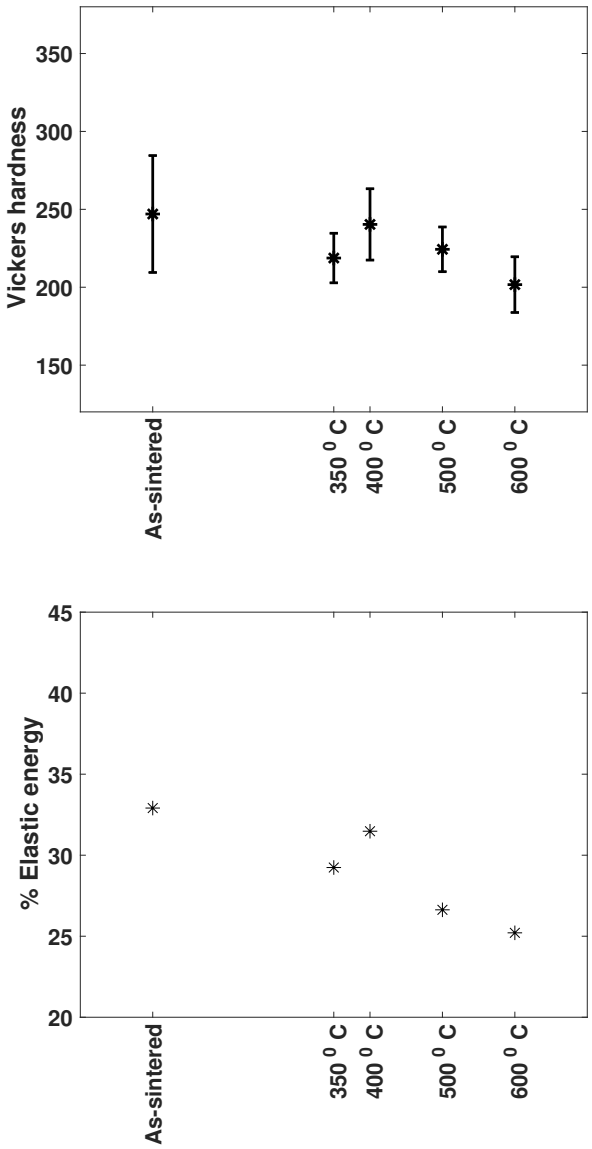

Figure 3.2: Vickers hardness and percentage of recoverable energy after 1 h direct aging at different temperatures. Error bars represent the standard deviations in 10 measurements.

Figure 3.3 shows that the hardness and the energy recovery ratio decreased considerably by 2 h of homogenization. Usually, homogenization treatment results in softening of NiTi alloys due to dissolution of secondary phases such as Ti_2Ni [82] as it was the case in this study. Further aging for an hour, in $350 - 600°C$ temperature range, did not result in a significant change in terms of hardness and energy recovery

ratio. A relatively higher energy recovery was achieved by aging at 600°C as shown in Figure 3.3. The DSC plots in Figure 2.7 and the XRD spectrum in Figure 2.14 show that the samples which were subjected to 2 h of homogenization, and 2 h of homogenization plus 1 h of aging at 600°C were mainly in the austenitic phase at the beginning of the indentation test. Therefore, higher deformation recovery was attributed to the reversible martensitic transformation instead of precipitation hardening.

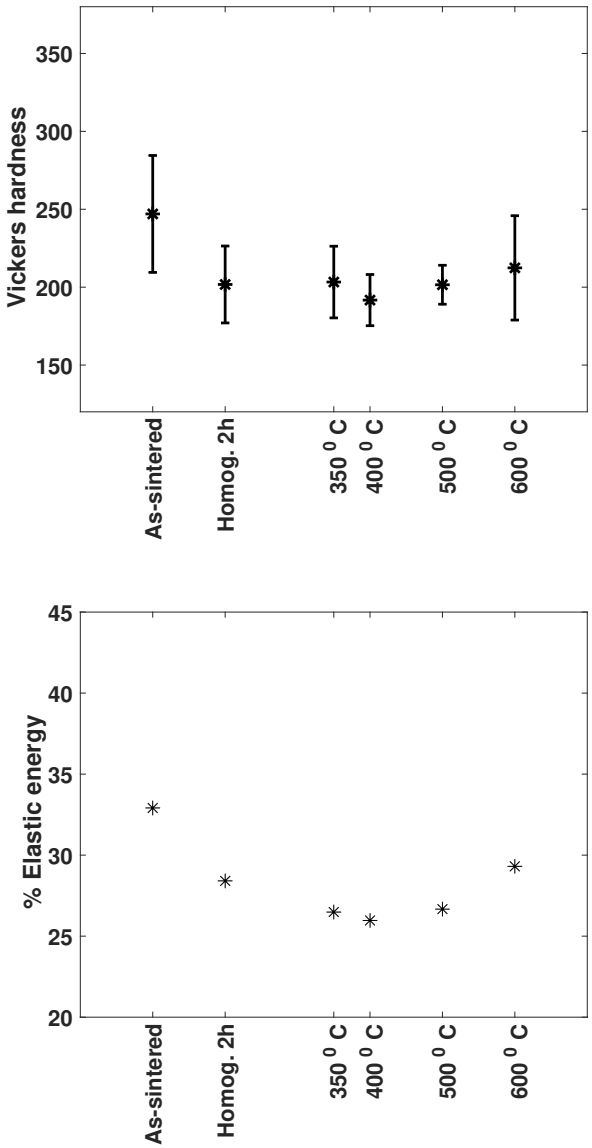

Figure 3.3: Vickers hardness and percentage of recoverable energy after 2 h homogenization at 1000°C and then 1 h aging at different temperatures. Error bars represent the standard deviations in 10 measurements.

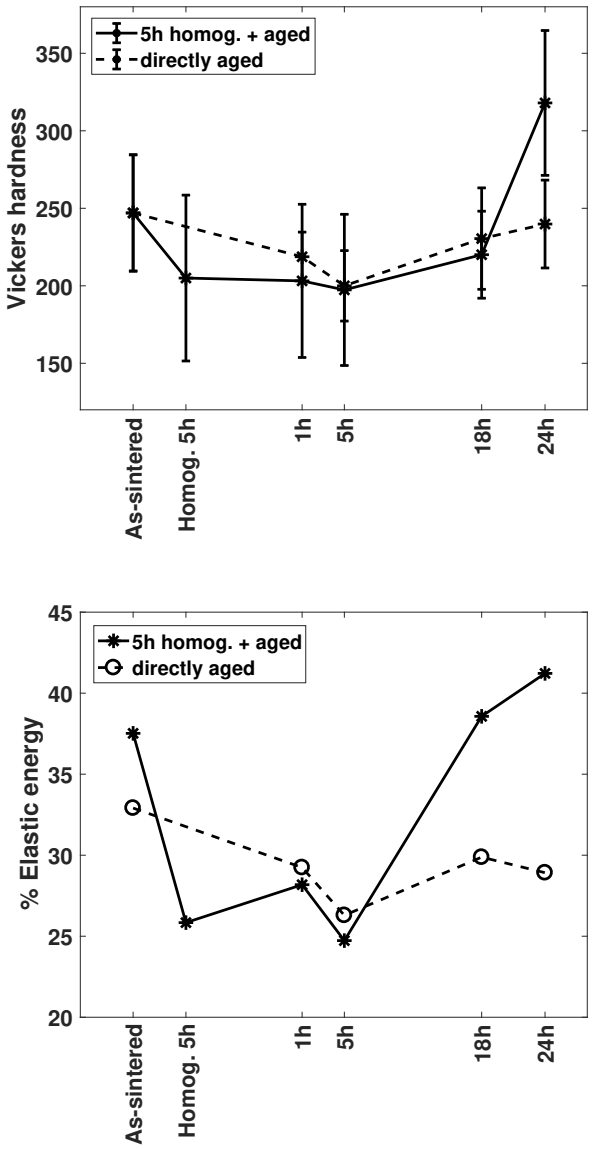

Figure 3.4: Vickers hardness and percentage of recoverable energy after aging at 350°C for different duration. Error bars represent the standard deviations in 10 measurements.

Strength of the alloy did not increase by the first two groups of heat treatments. In the third group of indentation analyzes, the material was subjected to aging at 350°C for various hours. The samples were either first homogenized for 5 h and then aged or directly aged from 1 to 24 h. The most significant enhancement in the hardness and the energy recovery ratio was achieved by increasing the aging time to 24 h as shown in Figure 3.4; the material that was first homogenized for 5 h and then aged for

24 h exhibited around 325 Vickers hardness, and %40 of energy recovery ratio. It is important that hardness and energy recovery ratio did not increase in the same way without homogenization prior to aging; the hardness achieved by 24 h of direct aging treatment was in the same level with the as-sintered one.

3.3. Uniaxial Compression

Cylindrical compression test specimens were machined from the sintered compacts with an L/d ratio of two (5 mm diameter, 10 mm length). The specimens were subjected to three different heat treatments to see the differences in their deformation under uniaxial compression: 1 h of direct aging; 2 h of homogenization and then 1 h of aging; 5 h of homogenization and then 24 h of aging, all samples being aged at 350°C. The samples were heated up to 100°C and then cooled down to the test temperature prior to uniaxial compression to increase the amount of austenite at the initial state. Compression tests were performed at 10^{-3} s^{-1} strain rate, until around 4% global strain, with a 30 kN Instron-5960 loading machine equipped with an environmental chamber controlling the temperature (see Figure 3.5). Each sample was compressed twice: first at a temperature 5°C above A_f to observe the pseudoelastic behavior. Second test was performed at room temperature (27°C), that is below A_f, to observe the shape memory effect. The displacement data were directly obtained from the machine and the correction for the setup compliance was obtained experimentally as suggested by Instron.

Figure 3.5: Instron setup for the compression tests (including oven).

3.3.1. Pseudoelastic Behavior

Figures 3.6-3.7 show the stress-strain responses of the samples which were tested above their A_f. In general, some residual strain was observed at the end of a partial-pseudoelastic loop which was not fully plastic. A significant portion of the residual strain was removed by re-heating the samples above A_f, and then cooling to the room temperature as shown by the red arrows on the stress-strain diagrams. It should be noted that the phase transformation of the sample which was subjected to 1 h of direct aging at 350°C continued gradually in a large temperature interval (see Figure 2.6). Therefore, that sample was loaded at 45°C which is 5°C above the temperature that corresponds to the end of the main transformation peak which is observed during heating. At that temperature, the alloy was expected to be in austenite-martensite mixed

structure. Therefore, the minimum strain recovery was achieved from the uniaxial compression of this specimen among all specimens that were tested in this study.

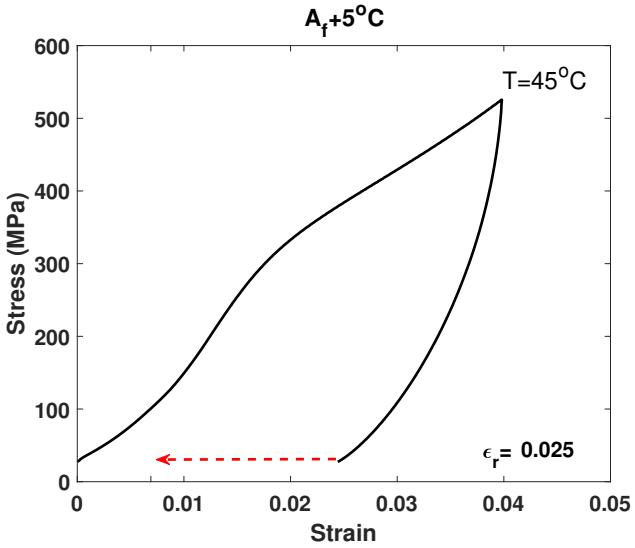

Figure 3.6: Stress-strain diagram at $A_f + 5$°C obtained from the sample subjected to 1 h of direct aging at 350°C. The residual strain at the end of unloading is presented inside the figure. Arrow represents the strain recovery by re-heating the sample until 100°C and then cooling to room temperature.

The specimen that was subjected to 2 h of homogenization and then 1 h of aging at 350°C was expected to be in complete austenite phase at 45°C according to its DSC plot. The strain recovery achieved from this specimen was higher than the one that was directly aged as shown in Figure 3.7. However, the maximum pseudoelastic strain recovery was achieved from the specimen that was subjected to 5 h of homogenization and then 24 h of aging at 350°C; around 50% of the deformation was recovered globally as shown in Figure 3.8.

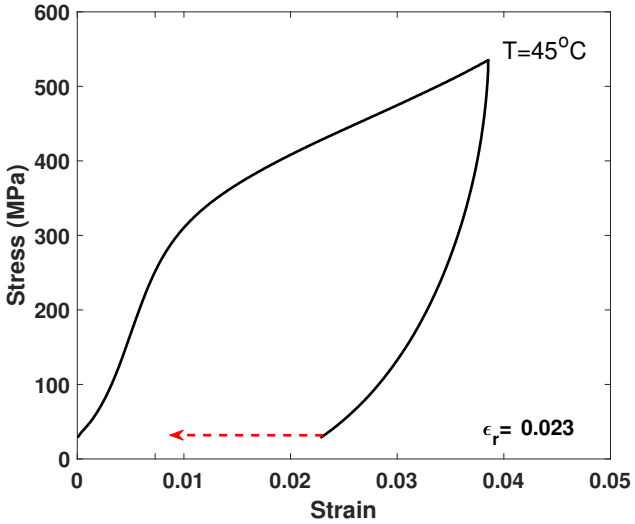

Figure 3.7: Stress-strain diagram at $A_f + 5°C$ obtained from the sample subjected to 2 h of homogenization and then 1 h of aging at 350°C. The residual strain at the end of unloading is presented inside the figure. Arrow represents the strain recovery by re-heating the sample until 100°C and then cooling to room temperature.

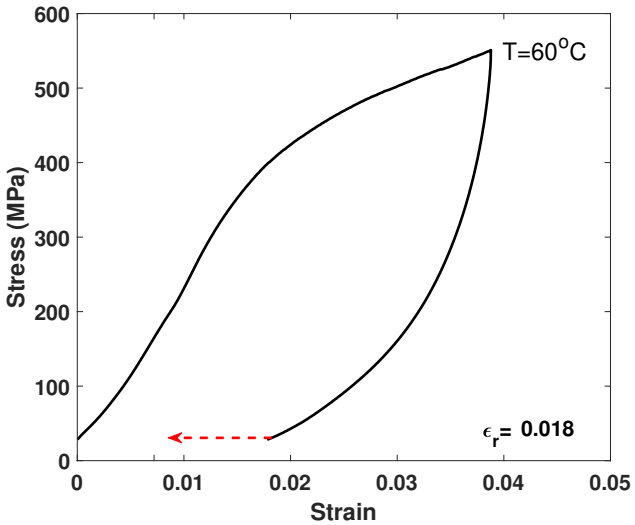

Figure 3.8: Stress-strain diagram at $A_f + 5°C$ obtained from the sample subjected to 5 h of homogenization and then 24 h of aging at 350°C. The residual strain at the end of unloading is presented inside the figure. Arrow represents the strain recovery by re-heating the sample until 100°C and then cooling to room temperature.

3.3.2. Shape Memory Effect

The shape memory effect of a spark plasma sintered NiTi alloy was previously studied by Samal et al. [97] in bending mode; around 3% strain recovery was achieved by heating up the specimens after unloading. In this study, the SME of the spark plasma sintered NiTi is observed under uni-axial compression; resulting stress-strain curves are presented in Figures 3.9-3.11.

At room temperature, the specimens were expected to be mostly in the martensite or R-phase, and the expected deformation mechanism was the martensitic reorientation. At the end of unloading, there was around 3% of residual strain which was almost completely recovered by reheating the specimens until around 100°C and then cooling back to room temperature. Although the pseudoelastic behavior was partial, the specimens from each category of heat treatments showed almost complete shape memory effect.

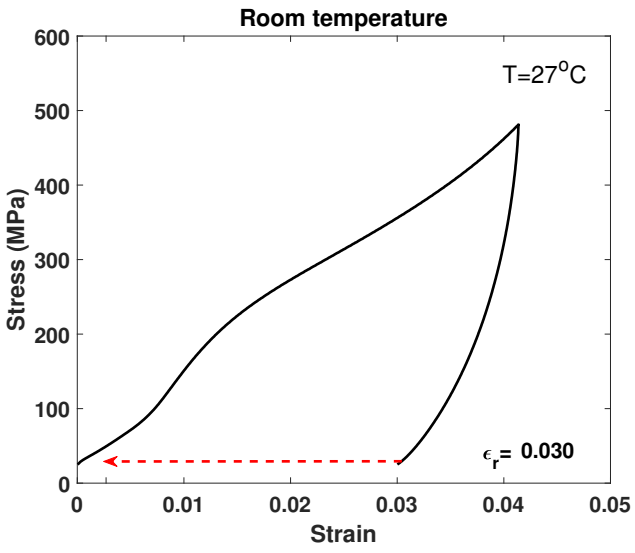

Figure 3.9: Stress-strain diagram at room temperature obtained from the sample subjected to 1 h of direct aging at 350°C. The residual strain at the end of unloading is presented inside the figure. Arrow represents the strain recovery by re-heating the sample until 100°C and then cooling to room temperature.

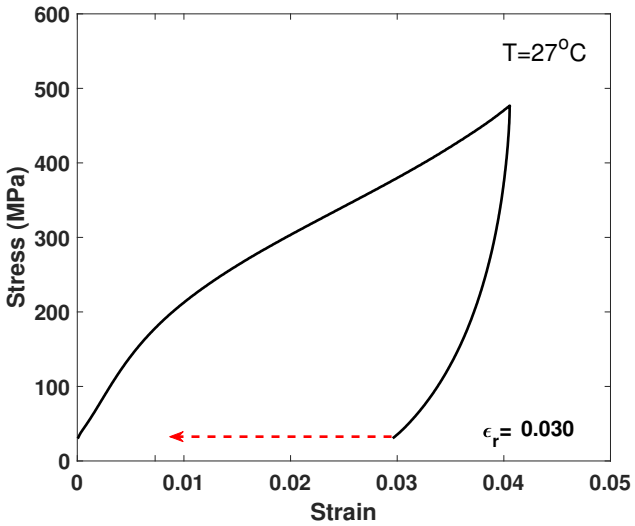

Figure 3.10: Stress-strain diagram at room temperature obtained from the sample subjected to 2 h of homogenization and then 1 h of aging at 350°C. The residual strain at the end of unloading is presented inside the figure. Arrow represents the strain recovery by re-heating the sample until 100°C and then cooling to room temperature.

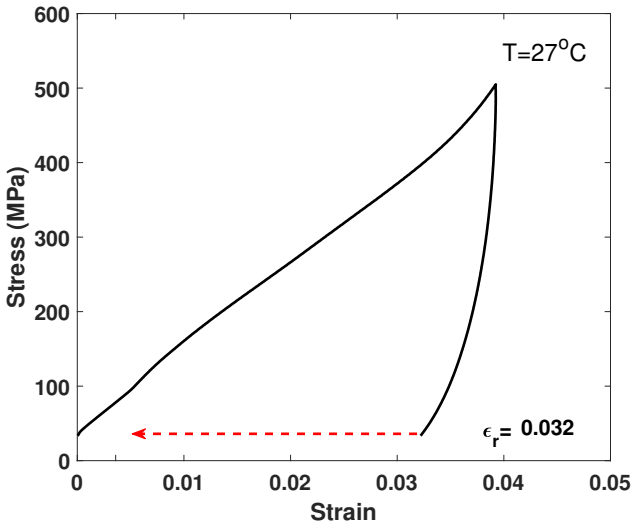

Figure 3.11: Stress-strain diagram at room temperature obtained from the sample subjected to 5 h of homogenization and then 24 h of aging at 350°C. The residual strain at the end of unloading is presented inside the figure. Arrow represents the strain recovery by re-heating the sample until 100°C and then cooling to room temperature.

3.4. Discussion and Conclusions

The effect of heat treatment on the mechanical behavior of the SPS processed NiTi alloy is discussed by using the experimental results provided in Chapters 2 and 3. The following conclusions are obtained:

The pseudoelastic experiments showed that the material did not fully recover from the deformation after compression; some of the deformation was recovered back by re-heating the samples above A_f and then cooling back to room temperature. Therefore, the residual strain might be due to some amount of blocked martensite plates in addition to a plastic deformation accompanying the phase transformation. In the literature, the full pseudoelastic behavior of NiTi alloys obtained through powder metallurgy was observed by a few researchers for alloys with either higher Ni concentration [19, 63] or produced with finer powders [64, 65]. A similar result was reported by McNeese et al. [70] for the uniaxial compression of NiTi samples processed by HIP. They observed significant residual strain after uniaxial compression of the samples tested above their A_f. The behavior was named as partial pseudoelastic, and it was attributed to the Ni concentration of the matrix (49 at.% Ni). In this study, the EDX analysis of the sample which has shown the maximum pseudoelastic strain recovery also revealed 49-50 at.% Ni concentration.

When the specimens were compared in three categories, the pseudoelastic strain recovery achieved by direct aging or short time homogenization and aging treatments were lower. The maximum recovery was achieved from the specimen that was subjected to 5 h of homogenization plus 24 h of aging at 350°C. Micro-indentation results showed that longer aging yielded the maximum hardness and energy recovery ratio, and it was the only case where the hardness increased considerably. DSC results in Figure 2.9 show that the sample was mostly in R-phase at the temperature when indentation was performed, therefore, the high energy recovery obtained from the micro-indentation test cannot be solely related to the reversible transformation between austenite and martensite phases. A certain amount of coherent Ti_3Ni_4 precipitation must be present

which enhances the resistance of the material against plastic deformation increasing the hardness and energy recovery. It is important that the long time aging treatment without prior homogenization did not result in the same age hardening mechanism showing the importance of increasing the homogeneity of the SPSed samples before aging.

4. CONSTITUTIVE MODELING OF POROUS SHAPE MEMORY ALLOYS USING POROMECHANICS

4.1. Introduction: Continuum Approach

Poromechanics is the area in which the mechanical behavior of porous materials is studied under the effect of a fluid saturating the porous space. Pioneering works were conducted especially in soil mechanics by considering the porous medium as a superposition of two continuous media: The first one is the skeleton made of a solid matrix comprising the empty porous space while the second one is the fluid saturating the porous space as shown in Figure 4.1 [52]. In this study, the poromechanics approach developed by O. Coussy [52] will be used as a fundamental reference when developing a macro-scale constitutive model describing the mechanical behavior of porous SMAs although there is no fluid in the porous space; only the skeleton particle will be modeled. The model can be improved by including state equations of a saturating fluid to study porous SMA structures placed in a fluid, e.g. SMA implants embedded in human bodies.

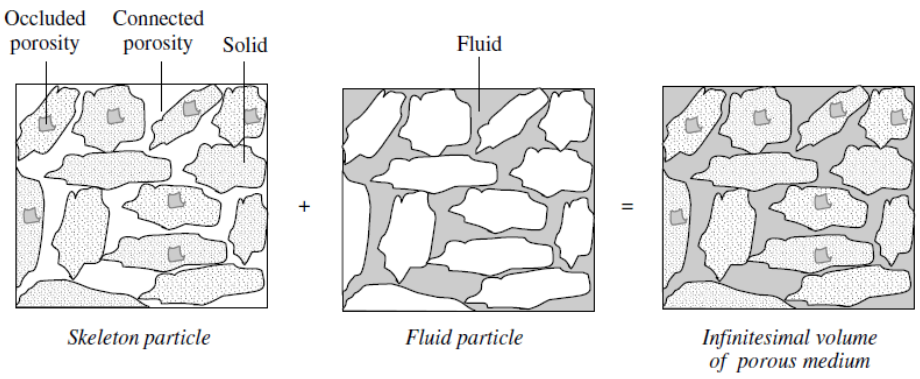

Figure 4.1: Porous medium: superposition of two continuous media [52].

4.2. Skeleton Deformation

The porosity of a material point, i.e. of a representative volume element (RVE), is defined as the ratio of the volume of the porous space to the total volume of the RVE. At that point, one can use the initial or the deformed volume of the RVE which leads to Lagrangian and Eulerian representation of the porosity [52]. Before proceeding with the formulas of skeleton deformation, the following definitions will be made:

ϕ_0 represents the porosity of the RVE in the undeformed (initial) state. It is calculated as the ratio of the volume of pores in the undeformed configuration to the total initial volume of the RVE. ϕ_0 is expressed as

$$\phi_0 = \frac{V_0^{pore}}{V_0^{tot}}. \tag{4.1}$$

On the other hand, ϕ_l represents the porosity of the RVE in the deformed (final) state. It is calculated as the ratio of the volume of pores in the deformed configuration to the total initial volume of the RVE. ϕ_l is expressed as

$$\phi_l = \frac{V_f^{pore}}{V_0^{tot}}. \tag{4.2}$$

ϕ_e also represents the porosity of the RVE in the deformed state. In contrast to ϕ_l, ϕ_e is calculated as the ratio of the volume of pores in the deformed configuration to the total volume of the deformed RVE. It is expressed as

$$\phi_e = \frac{V_f^{pore}}{V_f^{tot}}. \tag{4.3}$$

Note that

$$V_f = JV_0 \quad (J = det\boldsymbol{F}), \tag{4.4}$$

where V_0 and V_f are the total initial and total final volumes of the RVE. The superscript

"tot" will be omitted for simplicity.

By using Equation 4.4, one can obtain the relation

$$\begin{aligned} \frac{\phi_l}{\phi_e} &= \frac{V_f}{V_0} = J, \\ \Rightarrow \quad \phi_l &= J\phi_e \end{aligned} \tag{4.5}$$

between ϕ_l and ϕ_e . Under infinitesimal deformation,

$$J \simeq 1 + tr(\varepsilon). \tag{4.6}$$

Therefore,

$$V_f \simeq (1 + tr(\varepsilon))V_0. \tag{4.7}$$

Analogous to Eqn. 4.7, the following can be written for the skeleton volume

$$V_f^s = (1 + tr(\varepsilon)^s)V_0^s, \tag{4.8}$$

where the superscript 's' signifies solid (matrix). Using the definitions of porosity with respect to the initial and the final volumes, the volume of the solid (matrix) part can be related to the overall volume of the RVE as

$$\begin{aligned} V_f^s &= (1 - \phi_e)V_f \\ &= V_f - \phi_e V_f \\ &= V_f - \phi_l V_0, \end{aligned} \tag{4.9}$$

and

$$V_0^s = (1 - \phi_0)V_0. \tag{4.10}$$

Equations 4.8-4.10 yield the relation

$$tr(\varepsilon) = (1 - \phi_0)tr(\varepsilon)^s + \phi_l - \phi_0 \tag{4.11}$$

for the volume balance in the RVE. According to Equation 4.11, there are two sources of dilatation in the RVE: one is due to dilatation of the solid part while the other one is due to the change in the porosity. Equation 4.11 will act as a kinematic constraint on the RVE of a porous SMA, relating the strain tensor and the porosity. In the rest of the chapter, ϕ_l will be written as ϕ for simplicity.

4.3. Phenomenological Model

4.3.1. Generalized Constitutive Behavior of Shape Memory Alloys

As a first attempt, the constitutive behavior of the SMAs can be written as

$$\boldsymbol{\sigma} = \boldsymbol{K}_{eqv} : \boldsymbol{\varepsilon}^{el}, \tag{4.12}$$

where $\boldsymbol{K}_{eqv}$ is the equivalent elastic stiffness tensor of the SMA's representative volume element, and $\boldsymbol{\varepsilon}^{el}$ is the linear elastic part of the strain (the details of the inelastic constitutive relation is given in Appendix A.1).

An additive decomposition of the strain is done, and $\boldsymbol{\varepsilon}^{el}$ is obtained by subtracting the inelastic strain from the total one [98]. Here, the plastic slip and martensitic phase transformation are considered possible sources of inelastic deformation. As a result, the elastic strain is defined as

$$\boldsymbol{\varepsilon}^{el} = \boldsymbol{\varepsilon} - \boldsymbol{\varepsilon}^{pl} - \boldsymbol{\varepsilon}^{tr}, \tag{4.13}$$

where $\boldsymbol{\varepsilon}^{pl}$ and $\boldsymbol{\varepsilon}^{tr}$ represent the plastic and transformation strains, respectively. There-

fore, the stress-strain equation for the SMA is written as

$$\boldsymbol{\sigma} = \boldsymbol{K}_{eqv} : (\boldsymbol{\varepsilon} - \boldsymbol{\varepsilon}^{pl} - \boldsymbol{\varepsilon}^{tr}). \tag{4.14}$$

In the calculation of stress, $\boldsymbol{K}_{eqv}$, $\boldsymbol{\varepsilon}^{pl}$ and $\boldsymbol{\varepsilon}^{tr}$ are needed. In this work, a macro-scale phenomenological model is adopted to calculate them. First, an RVE is defined for the porous SMA medium (skeleton), and then a thermodynamic framework is provided. Details of the phenomenological approach are presented in the following sections.

4.3.2. Representative Volume Element and The Decomposition of Strain, $\boldsymbol{\varepsilon}$

The representative volume element is based on Reuss model as shown in Figure 4.2. It is composed of porous austenitic and martensitic regions under the effect of the same external stress. The porosity is assumed to be uniform in both the austenitic and the martensitic regions ($\phi^A = \phi^M = \phi$).

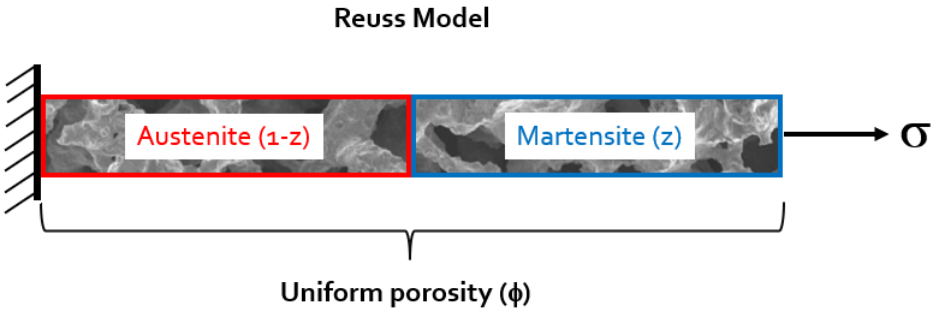

Figure 4.2: Reuss model for the porous RVE.

Deformation of the RVE, i.e. the SMA skeleton, is analyzed by considering both the deformation of its matrix and the porosity. The total deformation of the RVE can be divided into its austenitic and martensitic parts as

$$\boldsymbol{\varepsilon}_{RVE} = (1 - z)\boldsymbol{\varepsilon}_A + z\boldsymbol{\varepsilon}_M, \tag{4.15}$$

where $\boldsymbol{\varepsilon}_A$ and $\boldsymbol{\varepsilon}_M$ signifies the local strain tensors in the porous austenitic and martensitic regions including the volumetric change due to porosity. According to Equation 4.11, a strain tensor $\boldsymbol{\varepsilon}$ can be decomposed into its deviatoric and hydrostatic parts as

$$\begin{aligned} \boldsymbol{\varepsilon} &= \boldsymbol{\varepsilon}^{'} + \frac{tr(\varepsilon)}{3}\boldsymbol{I} \\ &= \boldsymbol{\varepsilon}^{'} + \frac{1}{3}\big[(1-\phi_0)tr(\varepsilon^s) + \phi - \phi_0\big]\boldsymbol{I}, \end{aligned} \tag{4.16}$$

where symbol $(^{'})$ signifies that the tensor is deviatoric. Therefore,

$$\boldsymbol{\varepsilon}_{RVE} = \big[(1-z)\boldsymbol{\varepsilon}^{'}_A + z\boldsymbol{\varepsilon}^{'}_M\big] + \frac{1}{3}\Big[(1-\phi_0)\big[(1-z)tr(\varepsilon^s_A) + ztr(\varepsilon^s_M)\big] + \phi - \phi_0\Big]\boldsymbol{I}. \tag{4.17}$$

Two parts of Equation 4.17 will constitute the kinematical constraints of the phenomenological model. They are expressed as

$$\boldsymbol{\varepsilon}^{'}_{RVE} = \big[(1-z)\boldsymbol{\varepsilon}^{'}_A + z\boldsymbol{\varepsilon}^{'}_M\big], \tag{4.18}$$

$$tr(\varepsilon_{RVE}) = \Big[(1-\phi_0)\big[(1-z)tr(\varepsilon^s_A) + ztr(\varepsilon^s_M)\big] + \phi - \phi_0\Big]. \tag{4.19}$$

z, $\boldsymbol{\varepsilon}^{'}_A$, $\boldsymbol{\varepsilon}^{'}_M$, $tr(\varepsilon^s_A)$, $tr(\varepsilon^s_M)$ and ϕ are naturally introduced into the phenomenological model as **internal state variables (ISVs)**. Based on the experimental results in the literature, and the ones provided in Chapter 3, plastic deformation and martensitic phase transformation are considered as the inelastic deformation mechanisms in the constitutive modeling of porous SMAs. Therefore, $\boldsymbol{\varepsilon}_{ori}$ and $\boldsymbol{\varepsilon}_{pl}$ are also introduced as ISVs. In addition, the total change in the porosity can be divided into elastic and plastic parts as

$$\phi - \phi_0 = \phi_{el} + \phi_{pl}, \tag{4.20}$$

where ϕ_{pl} represents the inelastic change in the porous volume [52]. Although there is no experimental data available to simulate the plastic deformation of pores, it is also included as an ISV in the formulation by considering future studies based on the

proposed model.

Incompressible Matrix Assumption:

If the volume change of the matrix is neglected when compared to the volume change of pores ($tr(\varepsilon)^s \cong 0$), it can be written that

$$tr(\varepsilon_{RVE}) = \phi - \phi_0. \tag{4.21}$$

Therefore, $\phi - \phi_0$ is the only source of the volumetric strain in the RVE. In this case, Equations 4.18 and 4.19 reduce to

$$\boldsymbol{\varepsilon}'_{RVE} = \left[(1-z)\boldsymbol{\varepsilon}'_A + z\boldsymbol{\varepsilon}'_M\right], \tag{4.22}$$

$$tr(\varepsilon_{RVE}) = \left(\phi - \phi_0\right). \tag{4.23}$$

From now on, the subscript RVE will be removed for simplicity, and $\boldsymbol{\varepsilon}$ will represent the total strain of the RVE.

4.3.3. Summary of Generalized Standard Materials

The generalized standard materials (GSM) framework [48] allows the calculation of the internal variables during inelastic deformation. In this thesis, the phenomenological SMA model of Zaki and Moumni [15,51], within the framework GSM with internal constraints is modified to model the mechanical behavior of porous SMAs (the original model is summarized in Appendix A). In the GSM framework, the mechanical behavior of a material is obtained using two potentials, namely a free energy potential (e.g. Helmholtz free energy) and a dissipation pseudo-potential. The free energy potential (ψ), which is a function of the external variables (like $\boldsymbol{\varepsilon}$ and T) and a set of dissipative (α) and/or non-dissipative (β) internal state variables (ISVs) is used in deriving the state equations and thermodynamic forces (A_α), as shown:

$$\sigma = \frac{\partial \psi}{\partial \varepsilon}, \quad A_\alpha = -\frac{\partial \psi}{\partial \alpha}, \quad 0 = \frac{\partial \psi}{\partial \beta}. \tag{4.24}$$

The dissipation pseudo-potential (D), a function of dissipative internal variables and their flux (α, $\dot{\alpha}$), relates the flux and the thermodynamic forces associated with the evolution of these variables. In the idea of generalized standard materials, the non-zero thermodynamic forces, A_α, are sub-gradients of the dissipation pseudo-potential. It is expressed as

$$A_\alpha \in \frac{\partial D}{\partial \dot{\alpha}}, \tag{4.25}$$

where D must be a non-negative, convex, lower semi-continuous function, and minimum at $\boldsymbol{\varepsilon} = 0$ to automatically satisfy the second law of thermodynamics.

Definition of the energy potentials and complete derivation of the phenomenological model are presented in the following sections. The details about the GSM framework can be found in [15, 48, 99].

4.3.4. State Equations

In the phenomenological modeling, state equations in 4.24 are derived from the Clausius-Duhem inequality [100]. For the skeleton deformation in the poromechanics formulation [52], the Clausius-Duhem inequality is formulated in the form of

$$\Phi_s = \boldsymbol{\sigma} : \frac{d\boldsymbol{\varepsilon}}{dt} + \boxed{p\frac{d\phi}{dt}} - s\frac{dT}{dt} - \frac{d\psi}{dt} \geq 0. \tag{4.26}$$

The second term in the inequality comes from the fluid-skeleton interaction through the fluid pressure p. By separating the strain into its deviatoric and hydrostatic parts, the dissipation inequality is written as

$$\Phi_s = \boldsymbol{\sigma}^{'} : \frac{d\boldsymbol{\varepsilon}^{'}}{dt} + \frac{1}{3}tr(\boldsymbol{\sigma})\frac{dtr(\varepsilon)}{dt} + p\frac{d\phi}{dt} - s\frac{dT}{dt} - \frac{d\psi}{dt} \geq 0. \tag{4.27}$$

The complete set of the external and internal state variables used in this model is given as

$$\psi = \psi\big(\boldsymbol{\varepsilon}^{'}, T, \boldsymbol{\varepsilon}^{'}_{A}, \boldsymbol{\varepsilon}^{'}_{M}, T, \phi, z, \boldsymbol{\varepsilon}_{ori}, \boldsymbol{\varepsilon}_{pl}, \phi_{pl}\big). \tag{4.28}$$

By taking partial derivatives of the Helmholtz free energy with respect to its variables, Equation 4.27 is written as

$$\begin{aligned}\Phi_s \;=\; & \frac{d\boldsymbol{\varepsilon}^{'}}{dt}\big[\boldsymbol{\sigma}^{'} - \frac{\partial\psi}{\partial\boldsymbol{\varepsilon}^{'}}\big] + \frac{dtr(\varepsilon)}{dt}\big[\frac{tr(\boldsymbol{\sigma})}{3} - \frac{d\psi}{dtr(\varepsilon)}\big] + \frac{d\phi}{dt}\big[p - \frac{d\psi}{d\phi}\big] + \frac{dT}{dt}\big[-s - \frac{\partial\psi}{dT}\big] \\ & -\frac{\partial\psi}{\partial\boldsymbol{\varepsilon}^{'}_{i}}\frac{\partial\boldsymbol{\varepsilon}^{'}_{i}}{\partial t} - \frac{\partial\psi}{\partial z}\frac{\partial z}{\partial t} - \frac{\partial\psi}{\partial\boldsymbol{\varepsilon}_{ori}}\frac{\partial\boldsymbol{\varepsilon}_{ori}}{\partial t} - \frac{\partial\psi}{\partial\boldsymbol{\varepsilon}_{pl}}\frac{\partial\boldsymbol{\varepsilon}_{pl}}{\partial t} - \frac{\partial\psi}{\partial\phi_{pl}}\frac{\partial\phi_{pl}}{\partial t} \geq 0, \end{aligned} \tag{4.29}$$

where $i = A, M$. From the inequality above, state equations and thermodynamic forces can be derived as

$$\boldsymbol{\sigma}^{'} = \frac{\partial\psi}{\partial\boldsymbol{\varepsilon}^{'}}, \tag{4.30}$$

$$\frac{tr(\boldsymbol{\sigma})}{3} = \frac{\partial\psi}{\partial tr(\varepsilon)}, \tag{4.31}$$

$$p = \frac{\partial\psi}{\partial\phi}, \tag{4.32}$$

$$s = -\frac{\partial\psi}{\partial T}, \tag{4.33}$$

$$0 = \frac{\partial\psi}{\partial\boldsymbol{\varepsilon}^{'}_{i}}, \quad i = A, M, \tag{4.34}$$

$$A_z = -\frac{d\psi}{dz}, \quad \boldsymbol{A}_{tr} = -\frac{d\psi}{d\boldsymbol{\varepsilon}_{ori}}, \quad \boldsymbol{A}_{\boldsymbol{\varepsilon}_{pl}} = -\frac{d\psi}{d\varepsilon_{pl}}, \quad A_{\phi_{pl}} = -\frac{d\psi}{d\phi_{pl}}. \tag{4.35}$$

The **incompressible matrix** assumption yields

$$\frac{dtr(\varepsilon)}{dt} = \frac{d\phi}{dt}. \tag{4.36}$$

Therefore, Equations 4.31 and 4.32 reduce into a single state equation in the form of

$$\frac{tr(\boldsymbol{\sigma})}{3} = \frac{d\psi}{d\phi}. \tag{4.37}$$

For the explicit derivation of the state equations and thermodynamic forces, a free energy potential and a dissipation pseudo-potential must be defined.

4.3.5. Free Energy and Lagrangian

Helmholtz free energy function, ψ, is constructed as a sum of the following energy contributions:

- Energy contributed by austenite as a result of its elastic deformation. It is proportional to the volume fraction of austenite $(1-z)$,
- Energy contributed by martensite as a result of its elastic deformation, and $C(T)$, the heat density of phase transformation. The sum is proportional to the volume fraction of martensite (z),
- Energy contributed due to total volumetric deformation of the RVE.
- Hardening energy due to the interaction between austenite-martensite or different variants of martensite,
- Hardening energy due to plastic deformation in the matrix,
- Hardening energy due to inelastic deformation of pores.

Experimental evidence shows that porosity has an effect on both the stiffness and the hardening of the material. Considering these effects, the proposed free energy function is given as

$$\begin{aligned}
\psi \;=\; & (1-z)\Big(\bar{\mu}_A(\phi)(\boldsymbol{\varepsilon}_A^{'}-\boldsymbol{\varepsilon}_{pl}):(\boldsymbol{\varepsilon}_A^{'}-\boldsymbol{\varepsilon}_{pl})\Big) \\
& +z\Big(\bar{\mu}_M(\phi)\big[(\boldsymbol{\varepsilon}_M^{'}-\boldsymbol{\varepsilon}_{pl}-\boldsymbol{\varepsilon}_{ori}):(\boldsymbol{\varepsilon}_M^{'}-\boldsymbol{\varepsilon}_{pl}-\boldsymbol{\varepsilon}_{ori})\big]\Big) \\
& +\left(\frac{1}{2}\bar{K}_{eq}(\phi,z)(\phi-\phi_0-\phi_{pl})^2\right) \\
& +\mathcal{F}(\phi)\Bigg(zC(T)+\left(G\frac{z^2}{2}+\frac{z}{2}\big[\alpha z+\beta(1-z)\big]\big[\frac{2}{3}\boldsymbol{\varepsilon}_{ori}:\boldsymbol{\varepsilon}_{ori}\big]\right) \\
& +\frac{H_1}{2}(\frac{2}{3}\boldsymbol{\varepsilon}_{pl}:\boldsymbol{\varepsilon}_{pl})+\frac{1}{2}H_2\phi_{pl}^2\Bigg),
\end{aligned} \tag{4.38}$$

where

$$C(T) = \zeta(T - A_{f_0}) + \kappa. \tag{4.39}$$

ζ, κ, α, β and G are material parameters related to phase transformation and orientation as explained in [15]. H_1 and H_2 are linear kinematic hardening coefficients corresponding to deviatoric and hydrostatic components of plastic deformation. $\bar{\mu}_A$, $\bar{\mu}_M$ and $\bar{K}_{eqv}$ are the effective shear modulus of the porous austenitic and porous martensitic regions and the overall effective bulk modulus of the RVE. $\mathcal{F}(\phi)$ is a function to be determined which will introduce the effect of porosity on the hardening. A function in the form of

$$\mathcal{F}(\phi) = (1 - \phi)^x \tag{4.40}$$

is proposed. Numerical simulations are found in accordance with the experimental results when $x = 2$ is used.

A constraints potential, ψ_L, is constructed with the following constraints

$$(1 - z)\boldsymbol{\varepsilon}_A{}' + z\boldsymbol{\varepsilon}_M{}' - \boldsymbol{\varepsilon}' = 0, \tag{4.41}$$

$$\varepsilon_0 - \sqrt{\frac{2}{3}\boldsymbol{\varepsilon}_{ori} : \boldsymbol{\varepsilon}_{ori}} \geq 0, \tag{4.42}$$

$$z \geq 0; \quad (1 - z) \geq 0, \tag{4.43}$$

$$\phi \geq 0; \quad (1 - \phi) \geq 0, \tag{4.44}$$

where ε_0 determines the limit of inelastic deformation through martensitic orientation. The constraint equations yield the constraints potential

$$\begin{aligned} \psi_L &= -\boldsymbol{\lambda} : \left[(1 - z)\boldsymbol{\varepsilon}_A' + z\boldsymbol{\varepsilon}_M' - \boldsymbol{\varepsilon}'\right] - \mu\left[\varepsilon_0 - \sqrt{\frac{2}{3}\boldsymbol{\varepsilon}_{ori} : \boldsymbol{\varepsilon}_{ori}}\right] - \nu_1 z - \nu_2(1 - z) \\ &\quad -\nu_3\phi - \nu_4(1 - \phi), \end{aligned} \tag{4.45}$$

where $\boldsymbol{\lambda}$, μ and ν_i are Lagrange multipliers. The unilateral constraints μ and ν_i must obey the following complementary conditions

$$\mu \geq 0, \quad \mu(\varepsilon_0 - \varepsilon_{ori}^{eqv}) = 0, \tag{4.46}$$

$$\nu_1 \geq 0, \quad \nu_1 z = 0, \tag{4.47}$$

$$\nu_2 \geq 0, \quad \nu_2(1-z) = 0, \tag{4.48}$$

which are known as Kuhn-Tucker conditions [98]. The sum of the free energy function and the constraints potential constructs the Lagrangian, $L = \psi + \psi_L$, which is then used to obtain the state equations and thermodynamic forces. As a result, deviatoric and hydrostatic parts of the stress-strain relation are obtained as

$$\boldsymbol{s} = 2\bar{\mu}_{eqv}(\boldsymbol{\varepsilon}^{'} - \boldsymbol{\varepsilon}_{pl} - z\boldsymbol{\varepsilon}_{ori}), \tag{4.49}$$

$$\frac{tr(\sigma)}{3} = \bar{K}_{eqv}(\phi - \phi_0 - \phi_{pl}) - P, \tag{4.50}$$

where $\boldsymbol{s}$ is the deviatoric part of the stress tensor. $\bar{\mu}_{eqv}$ and $\bar{K}_{eqv}$ are expressed as

$$\bar{\mu}_{eqv} = \left(\frac{1-z}{\bar{\mu}_A} + \frac{z}{\bar{\mu}_M}\right)^{-1} \quad , \quad \bar{K}_{eqv} = \frac{\bar{E}_{eqv}}{3(1-2\nu)}, \tag{4.51}$$

and,

$$\begin{aligned} P \;=\; & \left(\frac{(1-z)}{\bar{\mu}_A^2} + \frac{z}{\bar{\mu}_M^2}\right)\bar{\mu}_{eqv}^2(\boldsymbol{\varepsilon}^{'} - \boldsymbol{\varepsilon}_{pl} - z\boldsymbol{\varepsilon}_{ori}) : (\boldsymbol{\varepsilon}^{'} - \boldsymbol{\varepsilon}_{pl} - z\boldsymbol{\varepsilon}_{ori}) \\ & + \frac{1}{2}\frac{\partial \bar{K}_{eqv}}{\partial \phi}(\phi - \phi_0 - \phi_{pl})^2 + \frac{\partial \mathcal{F}}{\partial \phi}\Bigg(zC(T) + G\frac{z^2}{2} + \frac{z}{2}\big[\alpha z + \beta(1-z)\big]\big[\frac{2}{3}\boldsymbol{\varepsilon}_{ori} : \boldsymbol{\varepsilon}_{ori}\big] \\ & + \frac{H_1}{2}(\frac{2}{3}\boldsymbol{\varepsilon}_{pl} : \boldsymbol{\varepsilon}_{pl}) + \frac{1}{2}H_2\phi_{pl}^2\Bigg). \end{aligned} \tag{4.52}$$

Equations 4.49 and 4.50 are in a similar form with the stress-strain relations obtained by O. Coussy [52] for the porous elasto-plasticity. The term denoted by P is a pressure-like term similar to the fluid pressure in the poromechanics formulation. Since the RVE is emptied of fluid in this work, P is expected to be small as it is confirmed by numerical

observations.

The thermodynamic forces are explicitly written as

$$\begin{aligned} A_z &= \frac{1}{2}\frac{EL_{MA}}{(1-\phi)}\boldsymbol{s}:\boldsymbol{s}+\boldsymbol{s}:\boldsymbol{\varepsilon}_{ori}+(1-\phi)\Big(-C(T)-Gz-[\alpha z+\beta(\frac{1}{2}-z)][\frac{2}{3}\boldsymbol{\varepsilon}_{ori}:\boldsymbol{\varepsilon}_{ori}] \\ &\quad -\frac{1}{2}K_{eqv}^2\big(\frac{1}{K_A}-\frac{1}{K_M}\big)(\phi-\phi_0-\phi_{pl})^2\Big), \end{aligned} \tag{4.53}$$

where

$$EL_{MA}=(1+\nu)\left[\frac{1}{E_M}-\frac{1}{E_A}\right], \tag{4.54}$$

and,

$$\boldsymbol{A}_{\varepsilon_{pl}} = \boldsymbol{s}-\frac{2H_1}{3}(1-\phi)\boldsymbol{\varepsilon}_{pl}, \tag{4.55}$$

$$\boldsymbol{A}_{tr} = \boldsymbol{s}z-\frac{2}{3}z(1-\phi)(\alpha z+\beta(1-z))\boldsymbol{\varepsilon}_{ori}-\frac{2}{3}\mu\left[\frac{\boldsymbol{\varepsilon}_{ori}}{\sqrt{\frac{2}{3}\boldsymbol{\varepsilon}_{ori}:\boldsymbol{\varepsilon}_{ori}}}\right], \tag{4.56}$$

$$A_{\phi_{pl}} = \bar{K}_{eqv}(1-\phi)(\phi-\phi_0-\phi_{pl})-H_2(1-\phi)\phi_{pl}. \tag{4.57}$$

4.3.6. Dissipation Pseudo-potential and Limit Functions

The evolution of the dissipative internal variables will be obtained through the use of a dissipation pseudo-potential. The pseudo-potential for the bulk SMA in [51] is modified as

$$\begin{aligned} D &= D(\dot{z},\dot{\boldsymbol{\varepsilon}}_{ori},\dot{\boldsymbol{\varepsilon}}_{pl},\dot{\phi}_{pl}) \\ &= (1-\phi)^k\Bigg(\big[a(1-z)+bz\big]|\dot{z}|+z^2Y_{ori}\sqrt{\frac{2}{3}\dot{\boldsymbol{\varepsilon}}_{ori}:\dot{\boldsymbol{\varepsilon}}_{ori}} \\ &\quad +\big[(1-z)Y_{pl}^A+zY_{pl}^M\big]\sqrt{\frac{2}{3}\dot{\boldsymbol{\varepsilon}}_{pl}:\dot{\boldsymbol{\varepsilon}}_{pl}}+Y_{\phi_{pl}}|\dot{\phi}_{pl}|\Bigg), \end{aligned} \tag{4.58}$$

where k, a, b, Y_{ori}, ${Y_{pl}}^{A,M}$ and $Y_{\phi_{pl}}$ are positive materials constants. A simple formulation is adopted for the evolution of ϕ_{pl}; $Y_{\phi_{pl}}$ controls the critical value for the plastic deformation of pores under pure hydrostatic loading. The multiplier $(1-\phi)^k$ is proposed to introduce the effect of porosity on the onset of phase transformation and plastic deformation; $k = 2$ is used for the numerical calculations since experimental studies show that a polynomial fit of order two can represent the change in the compressive strength of the porous SMAs [25, 30].

Finally, limit functions are obtained using $A_\alpha \in \frac{\partial D}{\partial \dot{\alpha}}$ as outlined in section 4.3.3.

The limit function for forward phase transformation is

$$F_z^1 = A_z - (1-\phi)^k[a(1-z) + bz] \leq 0. \tag{4.59}$$

The limit function for reverse phase transformation is

$$F_z^2 = -A_z - (1-\phi)^k[a(1-z) + bz] \leq 0. \tag{4.60}$$

The limit function for martensite orientation is

$$F_{tr} = \left\| A_{tr} \right\|_{VM} - (1-\phi)^k z^2 Y_{ori}. \tag{4.61}$$

The limit function for plastic deformation in the matrix is

$$F_{pl} = \left\| A_{pl} \right\|_{VM} - (1-\phi)^k \left[(1-z)Y_{pl}^A + zY_{pl}^M\right]. \tag{4.62}$$

The limit function for plastic deformation in the pores due to expansion is

$$F_{\phi_{pl}}^1 = A_{\phi_{pl}} - (1-\phi)^k Y_{\phi_{pl}}. \tag{4.63}$$

Similarly, the limit function for plastic deformation in the pores due to shrinkage is

$$F^2_{\phi_{pl}} = -A_{\phi_{pl}} - (1-\phi)^k Y_{\phi_{pl}}. \tag{4.64}$$

In ZM model [15, 51], the limit function governing the martensite orientation is simplified as

$$\begin{aligned} F_{ori} &= \frac{F_{tr}}{z} = \left\| \boldsymbol{A}_{ori} \right\|_{VM} - (1-\phi)^k z Y_{ori} \qquad (4.65)\\ &= \left\| \boldsymbol{s} - \frac{2}{3}(1-\phi)(\alpha z + \beta(1-z))\boldsymbol{\varepsilon}_{ori} - \frac{2}{3}\frac{\mu}{z}\left[\frac{\boldsymbol{\varepsilon}_{ori}}{\sqrt{\frac{2}{3}\boldsymbol{\varepsilon}_{ori} : \boldsymbol{\varepsilon}_{ori}}}\right] \right\|_{VM} - (1-\phi)^k z Y_{ori}. \end{aligned}$$

During phase transformation, martensite is assumed to be completely oriented as soon as it is formed. In terms of modeling, it means

$$\varepsilon_0 = \sqrt{\frac{2}{3}\boldsymbol{\varepsilon}_{ori} : \boldsymbol{\varepsilon}_{ori}}. \tag{4.66}$$

In this case, the limit function for orientation is reduced to

$$F_{ori} = \left\| \boldsymbol{s} - \frac{2}{3\varepsilon_0^2}(1-\phi)(\boldsymbol{\sigma} : \boldsymbol{\varepsilon}_{ori})\boldsymbol{\varepsilon}_{ori} \right\|_{VM} - (1-\phi)^k z Y_{ori}. \tag{4.67}$$

Complementary laws:

Evolution of $\boldsymbol{\varepsilon}_{pl}$ and $\boldsymbol{\varepsilon}_{ori}$ must follow the normality rule as follows:

$$\dot{\boldsymbol{\varepsilon}}_{ori} = \eta \frac{\partial F_{ori}}{\partial \boldsymbol{X}^{ori}} = \frac{3}{2}\eta \frac{\boldsymbol{X}^{ori}}{X^{ori}_{VM}} = \eta \boldsymbol{N}_{ori}; \quad \eta \geq 0, \quad F_{ori} \leq 0, \quad \eta F_{ori} = 0, \tag{4.68}$$

and,

$$\dot{\varepsilon}_{pl} = \gamma \frac{\partial F_{pl}}{\partial \boldsymbol{X}^{pl}} = \frac{3}{2}\gamma \frac{\boldsymbol{X}^{pl}}{X^{pl}_{VM}}; = \gamma \boldsymbol{N}_{pl} \quad \gamma \geq 0, \quad F_{pl} \leq 0, \quad \gamma F_{pl} = 0, \tag{4.69}$$

and governed by the following set of complementary conditions, known as Kuhn-Tucker conditions [98]:

$$\dot{z} \geq 0, \quad F_z^1 \leq 0, \quad \dot{z}F_z^1 = 0, \tag{4.70}$$

$$\dot{z} \leq 0, \quad F_z^2 \leq 0, \quad \dot{z}F_z^2 = 0, \tag{4.71}$$

$$\eta \geq 0, \quad F_{ori} \leq 0, \quad \eta F_{ori} = 0, \tag{4.72}$$

$$\gamma \geq 0, \quad F_{pl} \leq 0, \quad \gamma F_{pl} = 0, \tag{4.73}$$

$$\dot{\phi}_{pl} \geq 0, \quad F_{\phi_{pl}}^1 \leq 0, \quad \dot{\phi}_{pl}F_{\phi_{pl}}^1 = 0, \tag{4.74}$$

$$\dot{\phi}_{pl} \leq 0, \quad F_{\phi_{pl}}^2 \leq 0, \quad \dot{\phi}_{pl}F_{\phi_{pl}}^2 = 0. \tag{4.75}$$

4.4. Equivalent Stiffness of Porous RVE

In reality, all the engineering materials are heterogeneous containing different sources of heterogeneity with different length scales. Therefore, homogeneity or heterogeneity of a material depends on the considered length scale. From the engineering point of view, bulk, in other words, average characteristics of a microscopically heterogeneous medium can be more meaningful for certain problems. In this connection, a material is called "macroscopically homogeneous" if the averages taken over a certain length scale are consistent with the overall behavior of the material [101].

4.4.1. Mori-Tanaka Homogenization

In this model, the Mori-Tanaka homogenization technique is used to estimate the effective properties of the porous RVE, namely $\bar{\mu}_{eqv}$ and $\bar{K}_{eqv}$. It is a common technique especially for the estimation of average properties of composite materials. It is based on Eshelby's equivalent inclusion theory. The M-T equivalent stiffness tensor for any

heterogeneous medium is derived as

$$\bar{\boldsymbol{C}}_{MT} = \sum_{r=0}^{N} f_r \boldsymbol{C}^r \boldsymbol{A}^r \left(\sum_{r=0}^{N} f_r \boldsymbol{A}^r \right)^{-1}, \tag{4.76}$$

where f_r and $\boldsymbol{C}^r$ represent the volume fraction and the stiffness tensor of individual phases in the medium, respectively. $\boldsymbol{A}^r$ is a strain concentration tensor; it is a function of the Eshelby tensor $\boldsymbol{S}^r$ which depends on the stiffness of matrix and the shape of inclusions [101, 102].

In the problem studied here, the pores are inclusions with zero stiffnesses. The RVE's equivalent stiffness estimation is done by averaging the bulk properties of austenite and martensite phases ($\bar{\mu}_i$, $\bar{\kappa}_i$) with the volume fraction of pores (ϕ). The model has an advantage of introducing the information of pore shape through Eshelby tensor. To simplify the derivation and the numerical implementation of analytical equations, spherical shape is assumed for the pore geometry. As a result, $\bar{\mu}_i$ and $\bar{K}_i$ are estimated as

$$\bar{\mu}_i = \frac{(1-\phi)(9\mu_i\kappa_i + 8\mu_i^2)}{\big(9\kappa_i + 8\mu_i + 6\phi(\kappa_i + 2\mu_i)\big)}, \tag{4.77}$$

$$\bar{K}_i = \frac{4\kappa_i\mu_i(1-\phi)}{4\mu_i + 3\phi\kappa_i}, \tag{4.78}$$

which are then used in Equation 4.51 to estimate $\bar{\mu}_{eqv}$ and $\bar{\kappa}_{eqv}$ of the RVE.

4.5. Numerical Implementation and Algorithmic Setup

To simulate the isothermal loading of a porous SMA body using ABAQUS finite elements package, the phenomenological model is implemented into a user-defined material subroutine (UMAT) using Fortran programming language. The loading history is divided into N increments; starting from the known initial state ($n = 0$), the problem is solved iteratively for $n = 1...N$ using the elastic predictor-plastic corrector method (return mapping algorithm-RMA). The problem is transformed into a discrete

formulation using implicit backward-Euler integration scheme [98]. In this thesis, $\boldsymbol{\varepsilon}_{ori}$ is assumed to be completely oriented as soon as it is formed and also assumed proportional to the stress deviator for the applications of uni-axial loading/unloading to reduce the number of test cases.

The numerical algorithm is summarized below. n represents the increment number while (k) is the number of iterations:

- Assume elastic increment and calculate the trial stress:

$$\begin{aligned} &z_{n+1}^{(0)} = z_n, \quad \boldsymbol{\varepsilon}_{pl}^{(0)}{}_{n+1} = \boldsymbol{\varepsilon}_{pl_n}, \quad \phi_{pl}{}_{n+1}^{(0)} = \phi_{pl_n}, \quad \bar{\boldsymbol{K}}_{eqv}{}_{n+1}^{(0)} = \bar{\boldsymbol{K}}_{eqv_n}, \\ &\boldsymbol{\sigma}_{n+1}^{(0)} = \bar{\boldsymbol{K}}_{eqv}{}_{n+1}^{(0)} : \left[\boldsymbol{\varepsilon}_{n+1} - z_{n+1}^{(0)}\boldsymbol{\varepsilon}_{n+1}^{ori} - \boldsymbol{\varepsilon}_{n+1}^{pl(0)} - \frac{\phi_{pl}{}_{n+1}^{(0)}}{3}\boldsymbol{I}\right]. \end{aligned} \tag{4.79}$$

- During an elastic loading, limit functions must satisfy

$$F_i\left(\boldsymbol{\sigma}_{n+1}^{(k)}, z_{n+1}^{(k)}, \boldsymbol{\varepsilon}_{pl}^{(k)}{}_{n+1}, \phi_{pl}{}_{n+1}^{(k)}\right) \leq 0, \tag{4.80}$$

  where F_i represents F_z, F_{pl} and $F_{\phi_{pl}}$ respectively. When an inelastic deformation mechanism is active, the limit function reduces to equality, and the stress increment must be corrected by calculating the increments of ISVs. To calculate the increments, the limit functions are approximated using first-order Taylor series expansions in the neighborhood of $\left(\boldsymbol{\sigma}_{n+1}^{(k-1)}, z_{n+1}^{(k-1)}, \boldsymbol{\varepsilon}_{pl}^{(k-1)}{}_{n+1}, \phi_{pl}{}_{n+1}^{(k-1)}\right)$. It is expressed as

$$F_i^{k-1} + \frac{\partial F_i}{\partial \boldsymbol{\sigma}}^{k-1} : \Delta\boldsymbol{\sigma}^k + \frac{\partial F_i}{\partial z}^{k-1} \Delta z^k + \frac{\partial F_i}{\partial \boldsymbol{\varepsilon}_{pl}}^{k-1} : \Delta\boldsymbol{\varepsilon}_{pl}^k + \frac{\partial F_i}{\partial \phi_{pl}}^{k-1} \Delta\phi_{pl}^k = 0. \tag{4.81}$$

  In equations above, the $n+1$ subscript is eliminated for better readability, and $\Delta\alpha^{(k)} = \alpha^{(k)} - \alpha^{(k-1)}$ is the increment of a variable α at iteration k.

The normality rule in discrete form can be written as

$$\Delta\boldsymbol{\varepsilon}_{pl}{}^{(k)} = \gamma^{(k)}\boldsymbol{N}_{pl}^{(k)}, \tag{4.82}$$

where $\gamma^{(k)}$ is the discrete inelastic multiplier used to express the discrete normality rule at iteration k. $\boldsymbol{N}_{pl}$ is approximated at iteration k by its value at the previous iteration, with the initial values corresponding to an elastic prediction. Therefore,

$$F_i^{k-1} + \frac{\partial F_i}{\partial \boldsymbol{\sigma}}^{k-1} : \Delta\boldsymbol{\sigma}^k + \frac{\partial F_i}{\partial z}^{k-1} \Delta z^k + \gamma^k \frac{\partial F_i}{\partial \boldsymbol{\varepsilon}_{pl}}^{k-1} : \boldsymbol{N}_{pl}^{k-1} + \frac{\partial F_i}{\partial \phi_{pl}}^{k-1} \Delta\phi_{pl}^k = 0. \tag{4.83}$$

Noting that $\Delta\phi = \Delta\boldsymbol{\varepsilon} = 0$ between two iterations, $\Delta\boldsymbol{\sigma}^k$ can be written as

$$\begin{aligned}
\Delta\boldsymbol{\sigma}^k &= \Delta\bar{\boldsymbol{K}}_{\boldsymbol{eqv}}{}^{k} : \boldsymbol{\varepsilon}_{el} + \bar{\boldsymbol{K}}_{\boldsymbol{eqv}} : \Delta\boldsymbol{\varepsilon}_{el}^k - \Delta P^k \boldsymbol{I} \\
&= \Delta z^k \frac{\partial \bar{\boldsymbol{K}}_{eqv}}{\partial z} : \boldsymbol{\varepsilon}_{el} + \bar{\boldsymbol{K}}_{eqv} : \left(- \Delta\boldsymbol{\varepsilon}_{pl}^k - \Delta z^k \boldsymbol{\varepsilon}_{ori} - \frac{\Delta\phi_{pl}^k}{3}\boldsymbol{I} \right) - \Delta P^k \boldsymbol{I} \\
&= \left(\frac{\partial \bar{\boldsymbol{K}}_{\boldsymbol{eqv}}}{\partial z} : \boldsymbol{\varepsilon}_{el} - \bar{\boldsymbol{K}}_{eqv} : \boldsymbol{\varepsilon}_{ori} \right) \Delta z^k - \bar{\boldsymbol{K}}_{eqv} : \Delta\boldsymbol{\varepsilon}_{pl}^k - \frac{1}{3}(\bar{\boldsymbol{K}}_{eqv} : \boldsymbol{I}) \Delta\phi_{pl}^k - \Delta P^k \boldsymbol{I}.
\end{aligned} \tag{4.84}$$

$\Delta z^{(k)}$, $\gamma^{(k)}$ and $\Delta\phi_{pl}^{(k)}$ are solved simultaneously by replacing Equation 4.84 into the equation set in (4.83).

- A continuous material Jacobian is derived as

$$\boldsymbol{J}_{n+1} = \left(\frac{d\boldsymbol{\sigma}}{d\boldsymbol{\varepsilon}} \right)_{n+1}, \tag{4.85}$$

where the time-continuous stress–strain relation is

$$\begin{aligned}
d\boldsymbol{\sigma} &= \bar{\boldsymbol{K}}_{eqv} : d\boldsymbol{\varepsilon}_{el} + d\bar{\boldsymbol{K}}_{eqv} : \boldsymbol{\varepsilon}_{el} - dP\boldsymbol{I} \\
&= \bar{\boldsymbol{K}}_{eqv} : \left(d\boldsymbol{\varepsilon} - dz\boldsymbol{\varepsilon}_{ori} - d\boldsymbol{\varepsilon}_{pl} - \frac{1}{3} d\phi_{pl} \boldsymbol{I} \right) \\
&\quad + \left(\frac{\partial \bar{\boldsymbol{K}}_{eqv}}{\partial \phi} (\boldsymbol{I} : d\boldsymbol{\varepsilon}) + \frac{\partial \bar{\boldsymbol{K}}_{eqv}}{\partial z} dz \right) : \boldsymbol{\varepsilon}_{el} - dP\boldsymbol{I}.
\end{aligned} \tag{4.86}$$

One needs to write dz, $d\gamma$ and $d\phi_{pl}$ in terms of $d\boldsymbol{\varepsilon}$ by using consistency enforcement

between two increments ($dF_z = dF_{pl} = dF_{\phi_{pl}} = 0$). It gives

$$\begin{aligned} \boldsymbol{J} &= \bar{\boldsymbol{K}}_{eqv} + \left(\frac{\partial \bar{\boldsymbol{K}}_{eqv}}{\partial \phi} : \boldsymbol{\varepsilon}_{el} \right) \otimes \boldsymbol{I} + \left(\left(\bar{\boldsymbol{K}}_{eqv,z} : \boldsymbol{\varepsilon}_{el} - \bar{\boldsymbol{K}}_{eqv} : \boldsymbol{\varepsilon}_{ori} \right) \otimes \boldsymbol{J_z} \right) \\ &\quad - \left((\bar{\boldsymbol{K}}_{eqv} : \boldsymbol{N}_{pl}) \otimes \boldsymbol{J_\gamma} \right) - \frac{1}{3} \left((\bar{\boldsymbol{K}}_{eqv} : \boldsymbol{I}) \otimes \boldsymbol{J_{\phi_{pl}}} \right), \end{aligned} \tag{4.87}$$

where

$$\boldsymbol{J}_z = (\boldsymbol{C}^{-1})_{1j} \boldsymbol{F}_j, \tag{4.88}$$

$$\boldsymbol{J}_\gamma = (\boldsymbol{C}^{-1})_{2j} \boldsymbol{F}_j, \tag{4.89}$$

$$\boldsymbol{J}_{\phi_{pl}} = (\boldsymbol{C}^{-1})_{3j} \boldsymbol{F}_j, \tag{4.90}$$

and,

$$\boldsymbol{F} = \left\{ \begin{array}{c} -\bar{\boldsymbol{K}}_{eqv} : \boldsymbol{F}_{z,\sigma} - (\boldsymbol{F}_{z,\sigma} : \frac{\partial \bar{\boldsymbol{K}}_{eqv}}{\partial \phi} : \boldsymbol{\varepsilon}_{el} + F_{z,\phi}) \boldsymbol{I} \\ -\bar{\boldsymbol{K}}_{eqv} : \boldsymbol{F}_{pl,\boldsymbol{\sigma}} - (\boldsymbol{F}_{pl,\boldsymbol{\sigma}} : \frac{\partial \bar{\boldsymbol{K}}_{eqv}}{\partial \phi} : \boldsymbol{\varepsilon}_{el} + F_{pl,\phi}) \boldsymbol{I} \\ -F_{\phi_{pl},\phi} \boldsymbol{I} \end{array} \right\}, \tag{4.91}$$

and ,

$$\boldsymbol{C} = \begin{pmatrix} \left(\boldsymbol{F}_{z,\sigma} : \left(\boldsymbol{K}_{,z} : \boldsymbol{\varepsilon}_{el} - \boldsymbol{K} : \boldsymbol{\varepsilon}_{ori} \right) + F_{z,z} \right) & \left(-\boldsymbol{F}_{z,\sigma} : \boldsymbol{K} : \boldsymbol{N}_{pl} \right) & \left(-\frac{1}{3} \boldsymbol{F}_{z,\sigma} : \boldsymbol{K} : \boldsymbol{I} + F_{z,\phi_{pl}} \right) \\ \left(\boldsymbol{F}_{pl,\boldsymbol{\sigma}} : \left(\boldsymbol{K}_{,z} : \boldsymbol{\varepsilon}_{el} - \boldsymbol{K} : \boldsymbol{\varepsilon}_{ori} \right) + F_{pl,z} \right) & \left(-\boldsymbol{F}_{pl,\boldsymbol{\sigma}} : \boldsymbol{K} : \boldsymbol{N}_{pl} + \boldsymbol{F}_{pl,\varepsilon_{pl}} : \boldsymbol{N}_{pl} \right) & \left(-\frac{1}{3} \boldsymbol{F}_{pl,\boldsymbol{\sigma}} : \boldsymbol{K} : \boldsymbol{I} \right) \\ \left(F_{\phi_{pl},z} \right) & \left(- \right) & \left(F_{\phi_{pl},\phi_{pl}} \right) \end{pmatrix} \tag{4.92}$$

The algorithm of the numerical model is summarized in Figure 4.3.

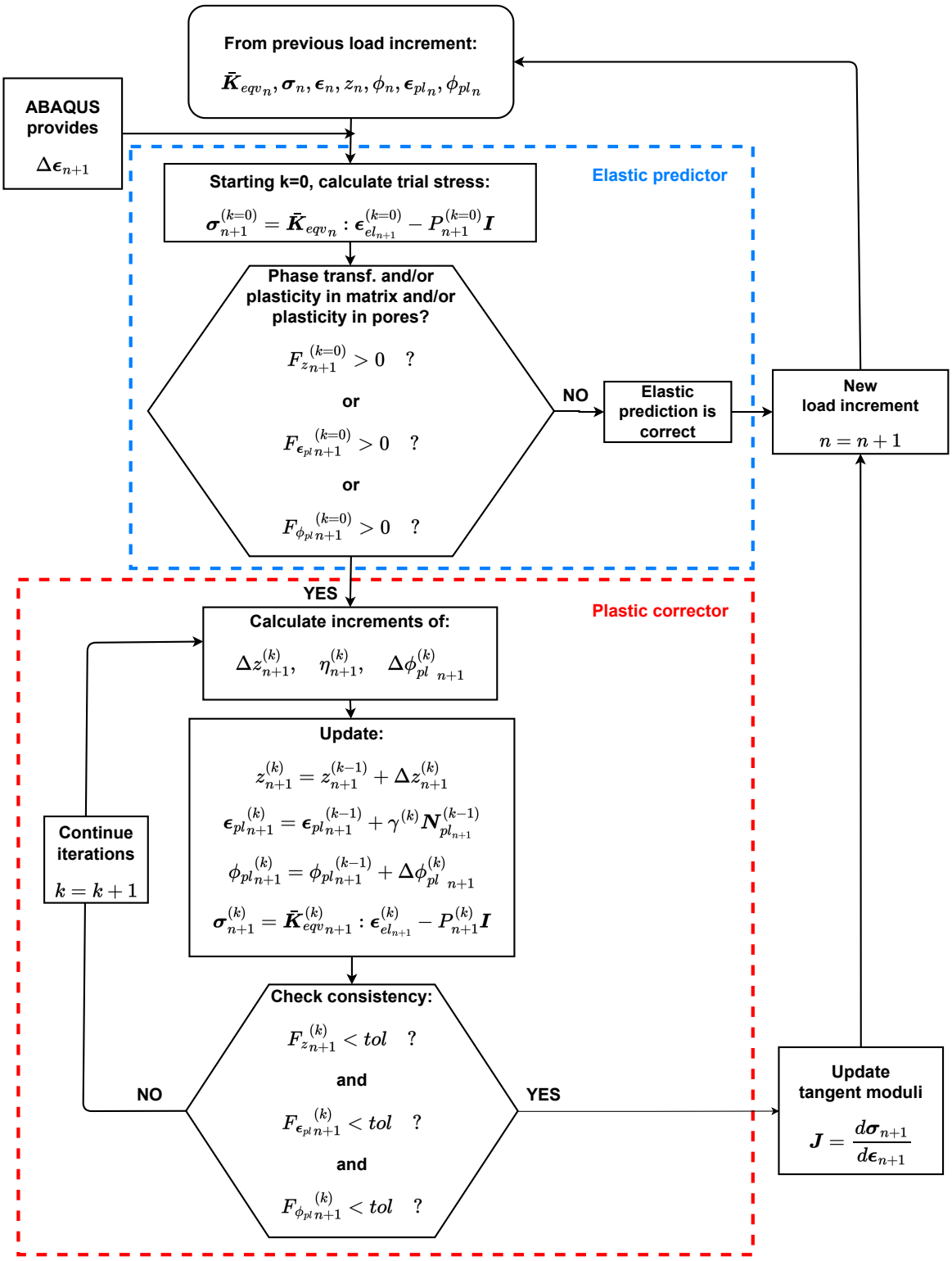

Figure 4.3: Return mapping algorithm for UMAT used in porous SMA modeling.

4.6. Results

In this section, the mechanical behavior of porous NiTi alloys from literature is simulated using the effective phenomenological model. The first simulation (Case-1) is performed for spark plasma sintered NiTi alloys produced by Zhao et al. [19]. And, the second simulation is performed for additively manufactured (selective laser melting) NiTi alloys produced by Saedi et al. [23]. A porosity range of 0-45% is studied numerically. The uniaxial stress-strain simulations are performed in Abaqus by using an 8-node hexahedral element with reduced integration; the element is fixed from one end, and subjected to displacement or force controlled loading-unloading at the other end. Stress-strain results are used to validate the phenomenological constitutive model, and further simulations are performed to show the model's capabilities.

4.6.1. Case-1: Uni-axial Compression of a Porous NiTi Alloy Produced by Spark Plasma Sintering

The first simulation is performed to obtain the stress-strain response of a 13% porous NiTi alloy tested by Zhao et al. [19] under uni-axial compression. The material parameters used for the model are listed in Table 4.1. Here, plasticity effects are not considered since the strain was totally recovered at the end of the experimental stress-strain curves in [19].

First, stress-strain response of the dense sample is simulated to validate selection of the material parameters used in the phenomenological model. The results provided in Figure 4.4 show that the pseudoelastic stress-strain loop can be simulated well using the material parameters listed in Table 4.1.

Table 4.1: Material parameters used for finite element simulations of the porous NiTi alloy produced by Zhao et al. [19].

Parameter	Value	Parameter	Value
E_A	66580 MPa	ν	0.3
E_M	54000 MPa	G	10 MPa
α	2000 MPa	ε_0	0.025
β	4000 MPa	ζ	0.0.2547 MPaK^{-1}
A_{f_0}	316.27 K	T	331.15 K
a	3.42 MPa	b	3.40 MPa
κ	2 MPa	H_1	-
Y_{pl}^A	-	Y_{pl}^M	-
H_2	-	$Y_{\phi_{pl}}$	-
x	2	k	2

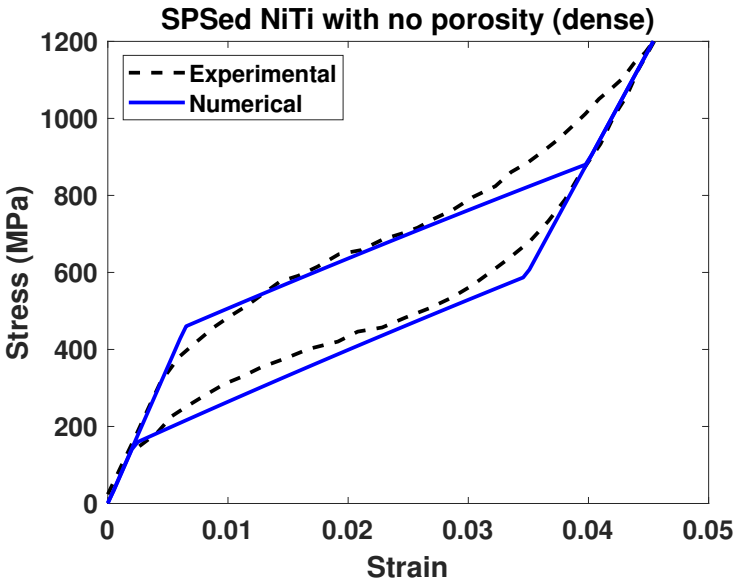

Figure 4.4: Simulation of the uni-axial stress-strain curve of the dense NiTi sample in [19] using phenomenological model.

Later, the initial porosity of the element is set to 13% and the stress-strain simulation is performed for the porous NiTi sample. The results are compared with the experimental ones as shown in Figure 4.5. The stress-strain curve obtained with the

effective model provides a very good match to the experimental results of Zhao et al. [19]. The model captures the changes in the pseudoelastic stress-strain loop of the NiTi alloy under the effect of porosity.

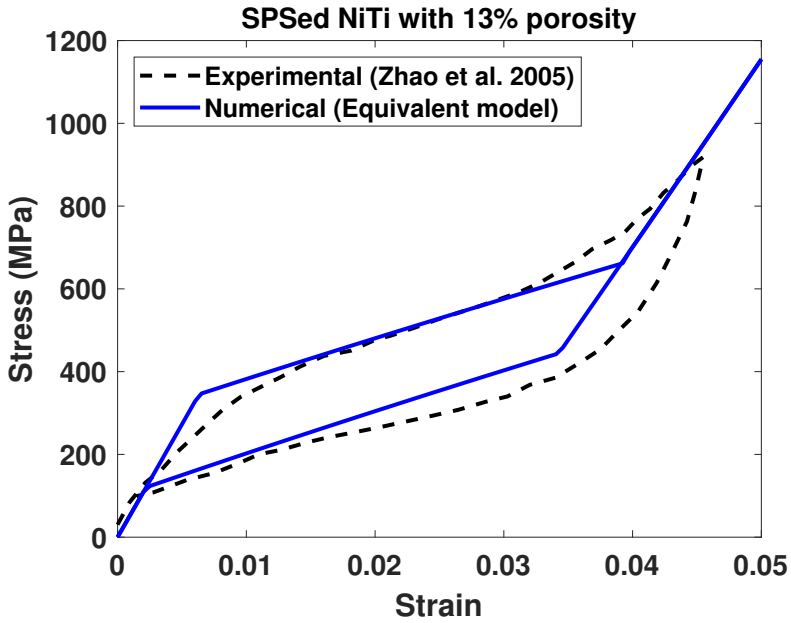

Figure 4.5: Simulation of the uni-axial stress-strain curve of 13% porous NiTi sample in [19] using the effective phenomenological model.

The effective model is further tested under multi-axial loading, specifically the combined tension/torsion loading. The butterfly shaped, strain controlled loading input is shown in Figure 4.6.a. Figures 4.6 b-d show numerical results in terms of axial and shear strains/stresses, volume fraction of martensite and porosity. The form of the stress-strain curves are similar to the ones of bulk SMAs provided by Gu et al. [103]. It is shown that the UMAT written for the effective phenomenological model of porous SMAs give reasonable results under multi-axial loading as well.

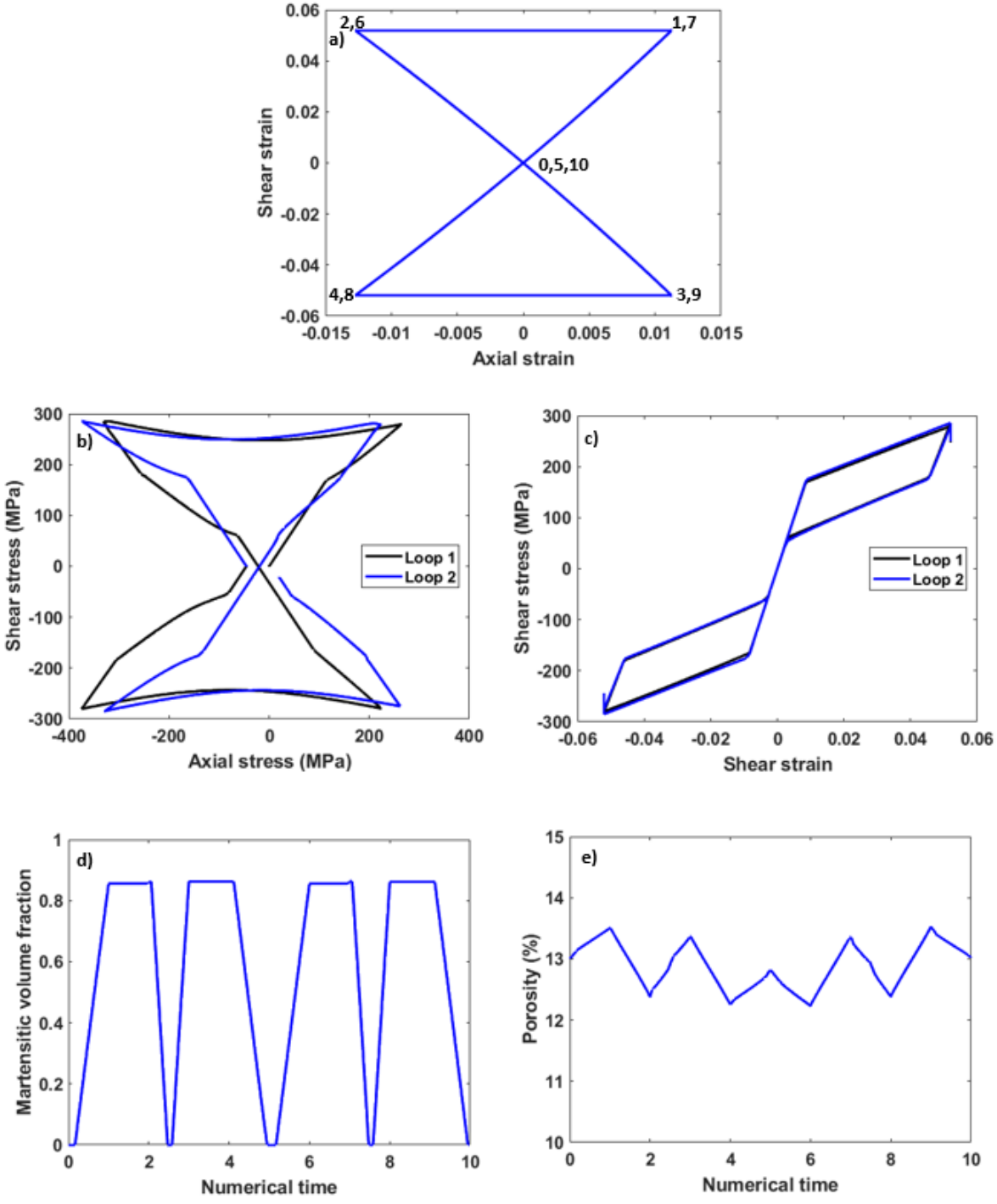

Figure 4.6: Numerical predictions of the model under strain controlled tension/torsion loading: a) Butterfly shape loading input (combination of axial and shear strains from 1 to 10), b) axial vs shear stress response, c) shear strain vs shear stress response, d) evolution of martensite volume fraction, e) evolution of porosity.

4.6.2. Case-2: Uni-axial Compression of a Porous NiTi Alloy Produced by Additive Manufacturing

32% and 45% porous SLM-processed NiTi alloys were tested by Saedi et al. [19] under uni-axial compression. The material parameters used for the SLM processed NiTi samples [28] are listed in Table 4.2; they are obtained from the experimental results provided in [28] and [49]. Since there is no distinct plastic region on the stress-strain curve of the dense sample, it is assumed that plastic deformation and phase transformation take place simultaneously as commonly accepted in the literature [104,105]. In [28], no data was provided regarding pure inelastic deformation of the material, therefore, yield strength and hardening parameters are assigned to obtain a good correlation between the experimental and numerical stress-strain curves of the dense sample. In addition, plasticity is considered only in the matrix because there is no data available in the literature to compare the plastic deformation of pores.

Table 4.2: Material parameters used for finite element simulations of the porous NiTi alloy produced by Saedi et al. [23].

Parameter	Value	Parameter	Value
E_A	43645 MPa	ν	0.3
E_M	378210 MPa	G	10 MPa
α	1785 MPa	ε_0	0.0385
β	2857 MPa	ζ	0.128 MPaK^{-1}
A_{f_0}	280.15 K	T	310.15 K
a	8.35 MPa	b	8.90 MPa
κ	4.27 MPa	H_1	25000 MPa
Y_{pl}^A	400 MPa	Y_{pl}^M	500 MPa
H_2	-	$Y_{\phi_{pl}}$	-
x	2	k	2

First, pseudoelastic response of the bulk sample is simulated to validate the selection of material parameters similar to Case-1. The simulation results are presented

in Figure 4.7 showing a good agreement with the experimental ones.

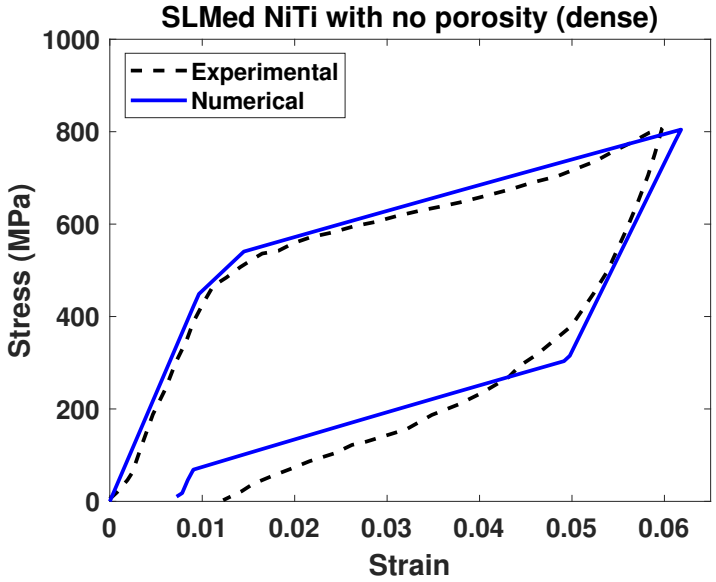

Figure 4.7: Simulation of the uni-axial stress-strain curve of the dense NiTi sample in [23] using phenomenological model.

Figure 4.8 shows the stress-strain simulation of the selective laser melted (SLMed) NiTi alloy with 32% porosity. Again, the numerical results obtained with the effective phenomenological model are very close to the experimental results. The only notable difference between the model results and the experimental one is observed around the start of reverse phase transformation; the simulation under-estimates the stress level for the reverse transformation. The gradual change in the stress during reverse transformation might be due to the effect of coupling between phase transformation and plasticity [105] which is not included in the current version of the phenomenological model.

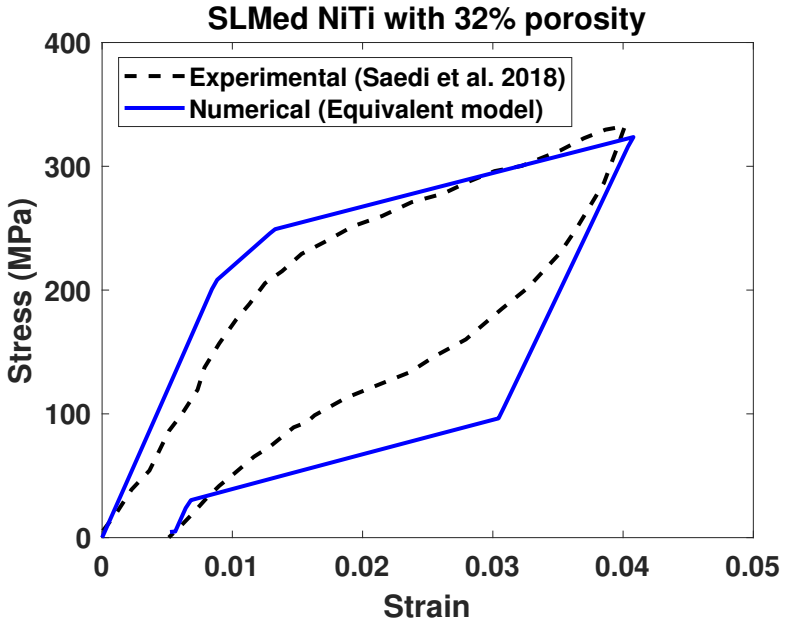

Figure 4.8: Simulation of the uni-axial stress-strain curve of 32% porous NiTi sample in [23] using the effective phenomenological model.

In addition to the global stress-strain simulation, internal variables can be observed throughout the loading history. Figure 4.9 shows the evolution of martensitic volume fraction and plastic strain along the loading axis in case-2. The model works for simultaneous evolution of phase transformation and plasticity. The austenite first transforms into martensite by around 50%, and then totally recovered by the reverse phase transformation during unloading. The evolution of porosity obtained from the simulations in case-2 is plotted in Figure 4.10. The porosity changes continuously; it first increases, and then decreases depending on the loading direction. There is a negative volumetric dilatation during loading part of the curve due to compression, it is totally recovered during unloading since the plastic deformation was only considered in the matrix due to lack of experimental data regarding plastic deformation of pores. In addition, the rate of change is slower when there is phase transformation or plastic deformation since there is no significant change in the stress in that time.

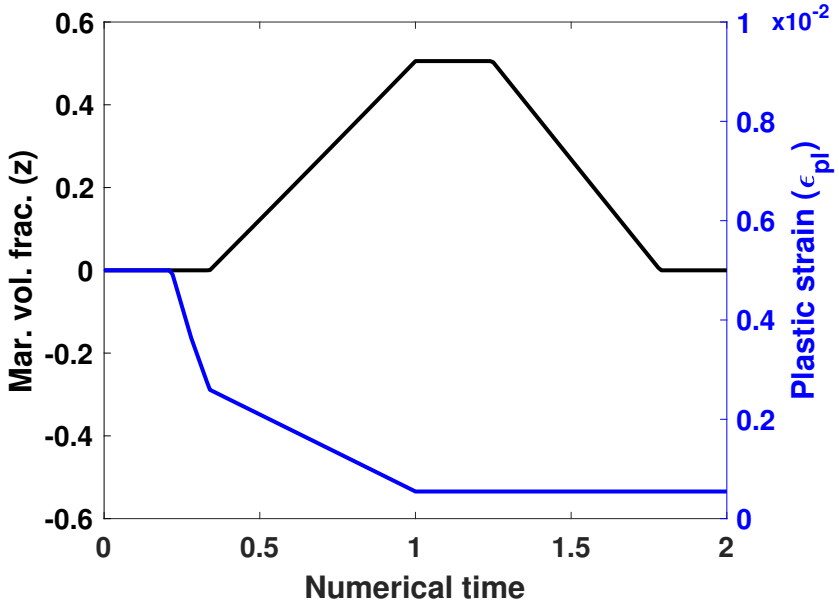

Figure 4.9: Numerical simulations of simultaneous evolution of phase transformation and plastic strain for 32% NiTi.

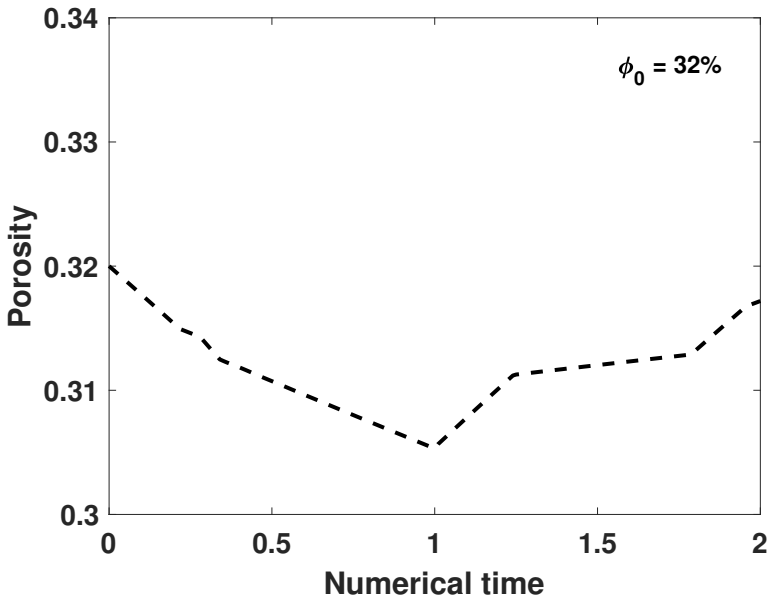

Figure 4.10: Numerical simulations of the evolution of porosity for 32% NiTi.

The effect of porosity level on the pseudoelastic loop of the NiTi alloy is presented through comparison of the stress-strain curves in Figure 4.11. It is shown that the model simulates the changes observed on the experimental stress-strain curve with

a good accuracy. The effective stiffness and the critical stresses for phase transformation decrease by increasing porosity, the simulations deviate from the experimental results when the porosity is large. The phenomenological model does not capture the stress-strain curve well for the 45% porous NiTi sample. A similar result was reported by Viet & Zaki [49] with their own phenomenological model for porous SMAs based on a scalar damage parameter, d. The model developed in this thesis provides stress-strain simulations very close to the ones provided by Viet & Zaki [49] with additional predictions of residual strains at the end of the unloading curves. It must be noted that the Mori-Tanaka homogenization is known to be more successful for smaller amounts of porosity. In addition, the effective model assumes a spherical pore shape for the simulations to simplify numerical application; the model can be improved by considering different pore shapes in the Mori-Tanaka homogenization. The possibility to change the pore shape in numerical calculations makes the phenomenological model very attractive for shape optimization studies of SMAs.

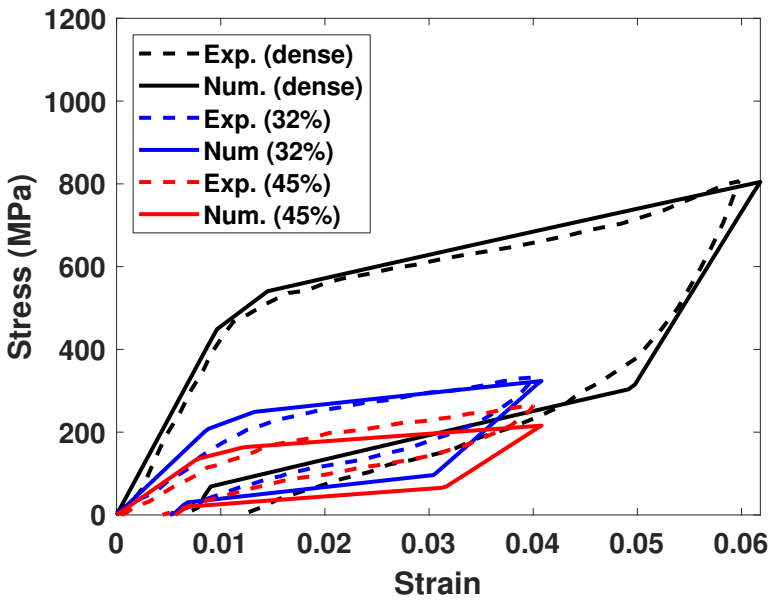

Figure 4.11: Pseudoelastic loops of the NiTi in [23] for different porosity.

A closer look at the effect of porosity on the compression strength and the elastic modulus is presented in Figures 4.12 and 4.13. The numerical results are obtained from the stress-strain curves given in Figure 4.11. Experimental and numerical results are

presented together to make a comparison. Additional simulations are performed with the effective phenomenological model by considering 10 and 25% initial porosity, and their results are included in Figures 4.12 and 4.13. The solid lines represent polynomial fits to the experimental results. It is shown that the second order polynomial, $(1-\phi)^2$, introduced in the dissipation pseudo-potential in Equation 4.58 is a reasonable selection to capture the onset of phase transformation. The numerical results are very close to the experimental ones even in the range of the compression strength of the human bone [30]. The critical stress is captured well for all porosity values. On the other hand, the stiffness predictions based on Mori-Tanaka homogenization are more successful for small amounts of porosity as shown in Figure 4.12. The model can be improved in terms of the stiffness estimation which is especially important when using porous NiTis for biomedical applications such as the human bone.

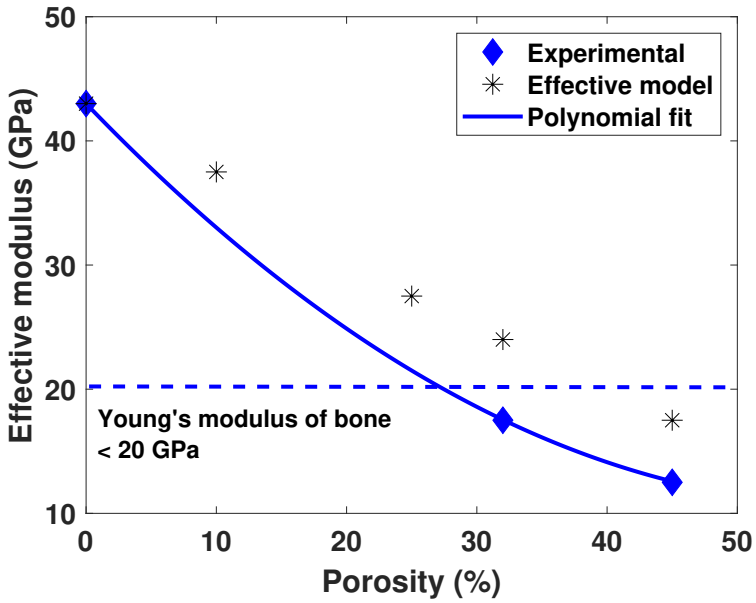

Figure 4.12: The effect of porosity on elastic modulus. Dotted lines indicate the thresholds for the human bone according to the literature.

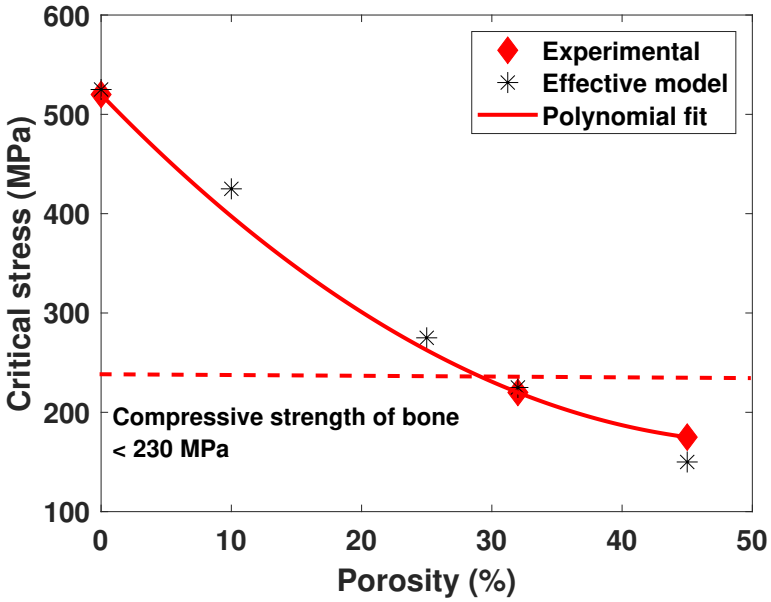

Figure 4.13: The effect of porosity on the the compressive strength. Dotted lines indicate the thresholds for the human bone according to the literature.

5. MODELING OF POROUS SHAPE MEMORY ALLOYS USING UNIT-CELLS

5.1. Introduction

A unit-cell (UC) is the smallest volume element that is used to represent the overall microstructure of a medium. For the porous materials or architectured cellular foams, a unit-cell geometry that consists of an empty space (void) in a solid SMA matrix is used as the representative element [28, 37–41]. The matrix part is modeled with a phenomenological constitutive model of bulk SMAs, and the effective (equivalent) material behavior is predicted from the volume-averaged properties of the UC. The UC can also be used as a sub-element in constructing a complex 3D structure. It can be useful to observe the local deformation of the structure while it is computationally tedious to create and simulate complex lattice structures.

In general, a unit-cell is used to represent a periodic microstructure with its repeating placements as shown in Figure 5.1. The same microstructure can be represented with different unit-cells, however, for finite element analyzes, it would be more preferable to use the smallest possible unit-cell and existing symmetry BCs. Li [106] details the selection of boundary conditions to obtain a correct representation of the micro-structure and the loading. For the periodic microstructure in Figure 5.1, which is under uni-axial loading, a suitable unit-cell, and necessary symmetry BCs are presented. A unit-cell without such reflection symmetries requires BCs in the form of equations relating displacements of opposite edges. It is then necessary to eliminate the rigid body motion by constraining the displacement of an arbitrary node [107].

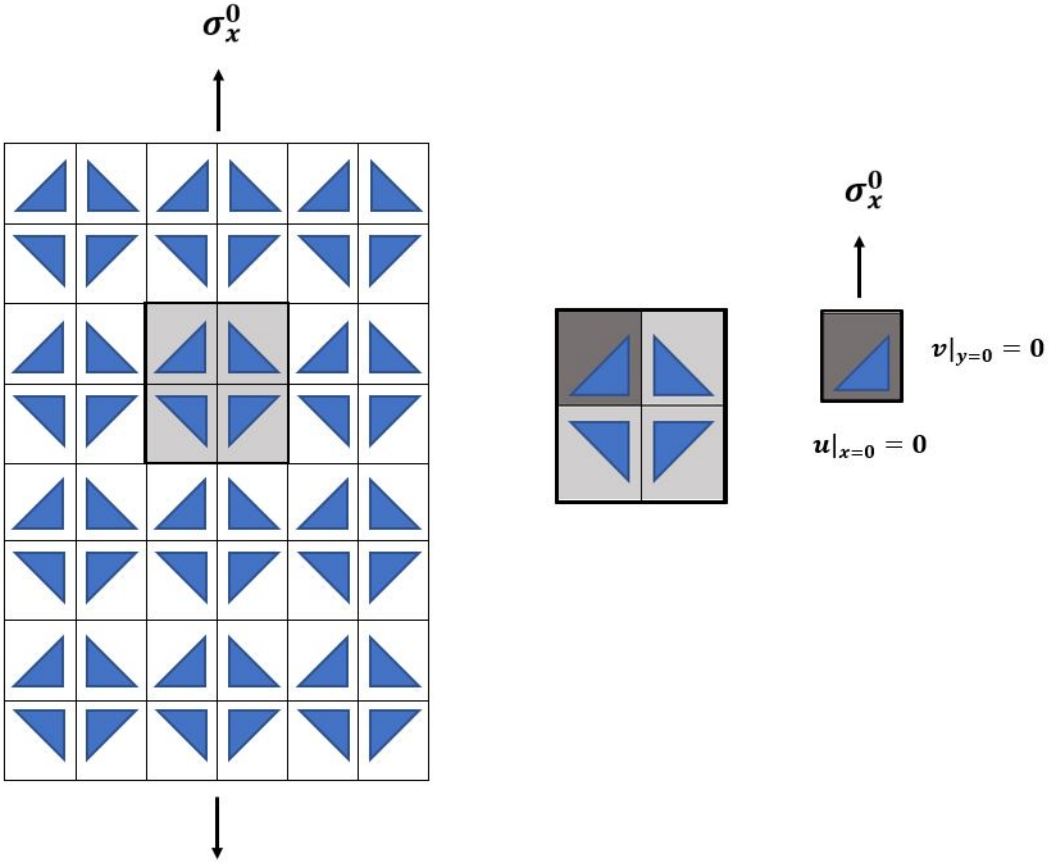

Figure 5.1: Schematic of a 2D periodic microstructure and unit-cell representation.

A unit-cell model can give good estimates of the deformation of architectured structures including SMAs. A pioneering work has been conducted by Cisse et al. [108] for architectured cellular Fe-based SMAs. The simulations obtained with the unit-cell approach is then used to make a numerical validation of their effective phenomenological model. A similar approach is performed in this chapter: The stress-strain response of the porous SMAs studied in Chapter 4 (Case-1 and Case-2) are simulated using the unit-cell method, and results are used to make a numerical validation of the newly developed effective (equivalent) phenomenological model. In addition, the modeling approaches are compared in terms of their advantages and disadvantages.

5.2. Simulation Using Unit-cell

Unit cell geometries are selected according to the specific microstructure of samples resulting from the powder metallurgy technique used. For each simulation, a single unit-cell is prepared using Abaqus, and appropriate symmetry boundary conditions are applied assuming periodic microstructure. Although the microstructure of sintered samples is not periodic, it will be shown that the unit-cell approach is still a good approximation, and gives good estimates of the effective mechanical behavior.

The solid part of the unit-cells is modeled using the phenomenological SMA model of Zaki and Moumni [15, 51] that includes phase transformation and plasticity phenomena. A summary of the phenomenological model can be found in Appendix A.

5.2.1. Case-1: Uni-axial Compression of a Porous NiTi Alloy Produced by Spark Plasma Sintering

To simulate the stress-strain response of the spark plasma sintered porous NiTi alloy [19], a unit-cell geometry is proposed by Karamooz et al. [37] by modeling the NiTi powders as spheres penetrated into each other through the sintering process. The unit-cell is modeled in Abaqus to obtain 13% porosity as shown in Figure 5.2. It has 3 symmetry planes; the normal translational degree of freedom is set to zero on $x = 0$, $y = 0$ and $z = 0$ planes, while $x = L$, $y = L$ and $z = L$ planes are forced to remain planar to supply periodic boundary conditions [37, 106]. The UC is loaded and unloaded with a pre-defined displacement to simulate the uni-axial compression test. C3D10M elements (10-node modified tetrahedron, with hourglass control) are used to mesh the UC geometry. The global stress is calculated by averaging the axial stress in each element over the unit-cell domain (including the porous space).

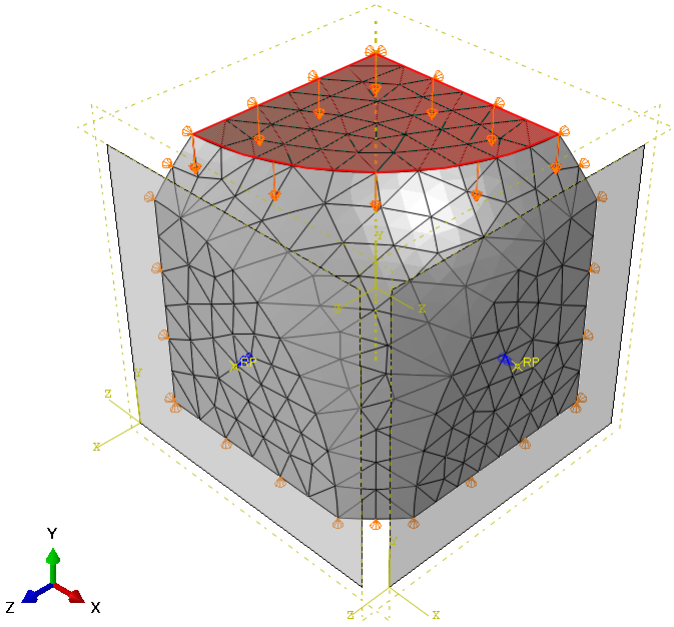

Figure 5.2: Geometry, boundary conditions and mesh on the UC used for case-1.

The material parameters needed for the unit cell model are listed in Table 5.1. These parameters are common to those listed in Table 4.1; there were additional parameters in Table 4.1 due to introduction of porosity as an internal state variable in the effective phenomenological model. Plasticity is not taken into account since there is no residual strain at the end of the stress-strain diagram obtained experimentally.

Table 5.1: Material parameters used for finite element simulations of the NiTi alloy produced by Zhao et al. [19]

Parameter	Value	Parameter	Value
E_A	66580 MPa	ν	0.3
E_M	54000 MPa	G	10 MPa
α	2000 MPa	ε_0	0.025
β	4000 MPa	ζ	0.0.2547 MPaK^{-1}
A_{f_0}	316.27 K	T	331.15 K
a	3.42 MPa	b	3.40 MPa
κ	2 MPa	H_1	-
Y_{pl}^A	-	Y_{pl}^M	-

Figure 5.3 shows the stress-strain diagram of 13% porous NiTi sample, and its simulation obtained with the unit-cell model. The numerical and experimental curves are found in good agreement. Although the unit-cells are designed for periodic microstructures, the numerical results showed that the unit cell approach can also provide reasonable predictions for the mechanical behavior of non-periodic structures (statistically homogeneous microstructures). It is important that the numerical results obtained using the unit-cell model are also very close to the numerical results obtained using the effective phenomenological model in Chapter 4. Both numerical approaches are found powerful in estimating the global stress-strain diagram of the NiTi sample with 13% porosity.

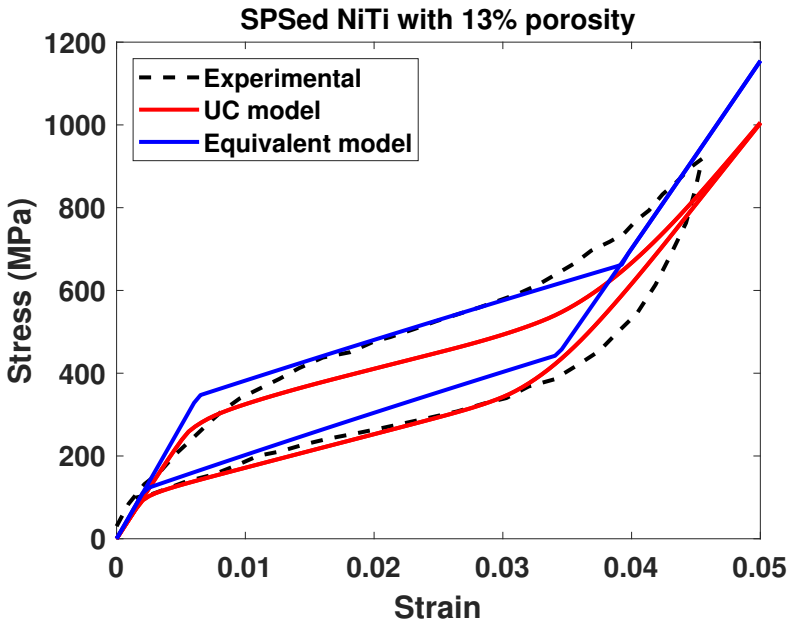

Figure 5.3: Simulation of the uni-axial stress-strain curve of 13% porous NiTi sample in [19] using UC model.

5.2.2. Case-2: Uni-axial Compression of a Porous NiTi Alloy Produced by Additive Manufacturing

A unit-cell geometry which is proposed by Saedi et al. [28] is used. Figure 5.4 shows the UC geometry of the SLMed NiTi with 32% porosity. Similar to Case-I, it has 3 symmetry planes; the normal translational degree of freedom is set to zero on $x = 0$,

$y = 0$ and $z = 0$ planes, while $x = L$, $y = L$ and $z = L$ planes are forced to remain planar to supply periodic boundary conditions. The UC is loaded and unloaded with a pre-defined pressure on the top surface. C3D10M elements are used by increasing the mesh density near curved edges. The global stress is calculated by dividing the applied stress with the projected area of the UC as performed by Saedi et al. [28].

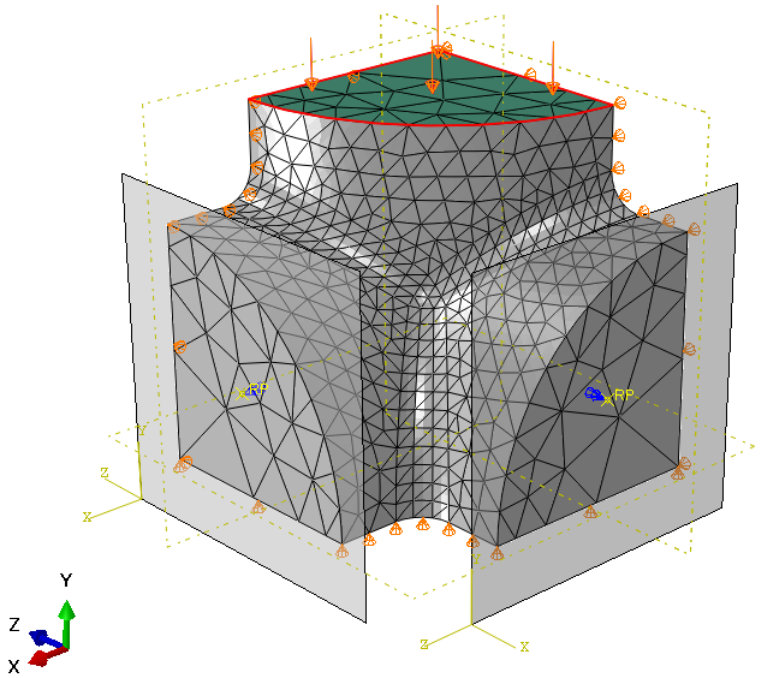

Figure 5.4: Geometry, boundary conditions and mesh on the UC used for case-2.

The material parameters used for the SLM processed NiTi samples [28] are listed in Table 5.2. Again, the parameters listed in Table 5.2 are common to those in Table 4.2 except for several additional parameters in Table 4.2.

Table 5.2: Material parameters used for finite element simulations of the NiTi alloy produced by Saedi et al. [23].

Parameter	Value	Parameter	Value
E_A	43645 MPa	ν	0.3
E_M	378210 MPa	G	10 MPa
α	1785 MPa	ε_0	0.0385
β	2857 MPa	ζ	0.128 MPaK^{-1}
A_{f_0}	280.15 K	T	310.15 K
a	8.35 MPa	b	8.90 MPa
κ	4.27 MPa	H_1	25000 MPa
Y_{pl}^A	400 MPa	Y_{pl}^M	500 MPa

The stress-strain simulation obtained with the UC model for 32% porous NiTi sample is shown in Figure 5.5. Again, the UC model has shown a good agreement with the experimental and the numerical results obtained using the effective model, even when there is plastic deformation. The only notable difference between the numerical and the experimental curves is observed around the start of reverse phase transformation; the unit-cell simulation under-estimates the stress level similar to the effective phenomenological model. The gradual change in the stress during reverse transformation might be due to the effect of coupling between phase transformation and plasticity [105] which is not included in the phenomenological models.

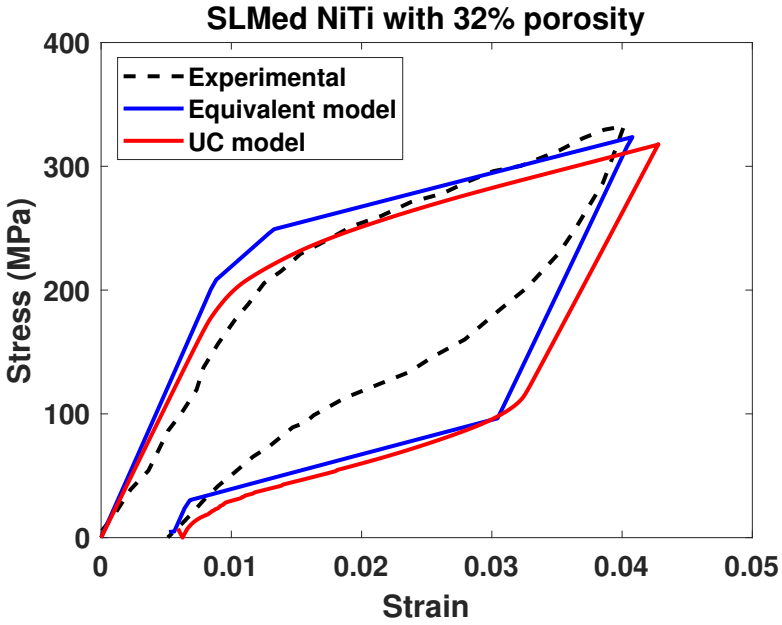

Figure 5.5: Simulation of the uni-axial stress-strain curve of 32% porous NiTi sample in [23] using UC model.

5.2.3. Comparison of Modeling Approaches: Effective Phenomenological Model vs Unit-Cell Model

In general, numerical results obtained using the effective phenomenological model and the unit-cell model are found very close. Both modeling techniques can be used when predicting the global stress-strain behavior of porous NiTi alloys. On the other hand, the unit-cell approach allows to observe local stress-strain distribution around pores. Figure 5.6 shows the distribution of the axial stress and the martensitic volume fraction on the UC of 13% porous NiTi sample at the end of the loading step. As shown in the figure, the stress, as well as the phase transformation, are locally at a minimum on the free surfaces of the RVE, i.e., on the pore walls. They are higher around the regions that represent contact surfaces of the powders during the sintering process. When compared to the unit-cell approach, the effective phenomenological model can only provide average results of the stress, or internal variables. However, there is a significant computational cost when using the UC model which makes the effective phenomenological model more advantageous for observations on bulk properties. The

effective model gives the simulation results in Figure 5.3 in 1-2 seconds with a single element while the unit-cell model gives the results in 567.50 seconds with 2730 elements (0.01 increment size is kept constant for both simulations). Complex geometries and the number of elements used in UC models increase the computation time while a very close and rapid simulation can be achieved using the effective phenomenological model.

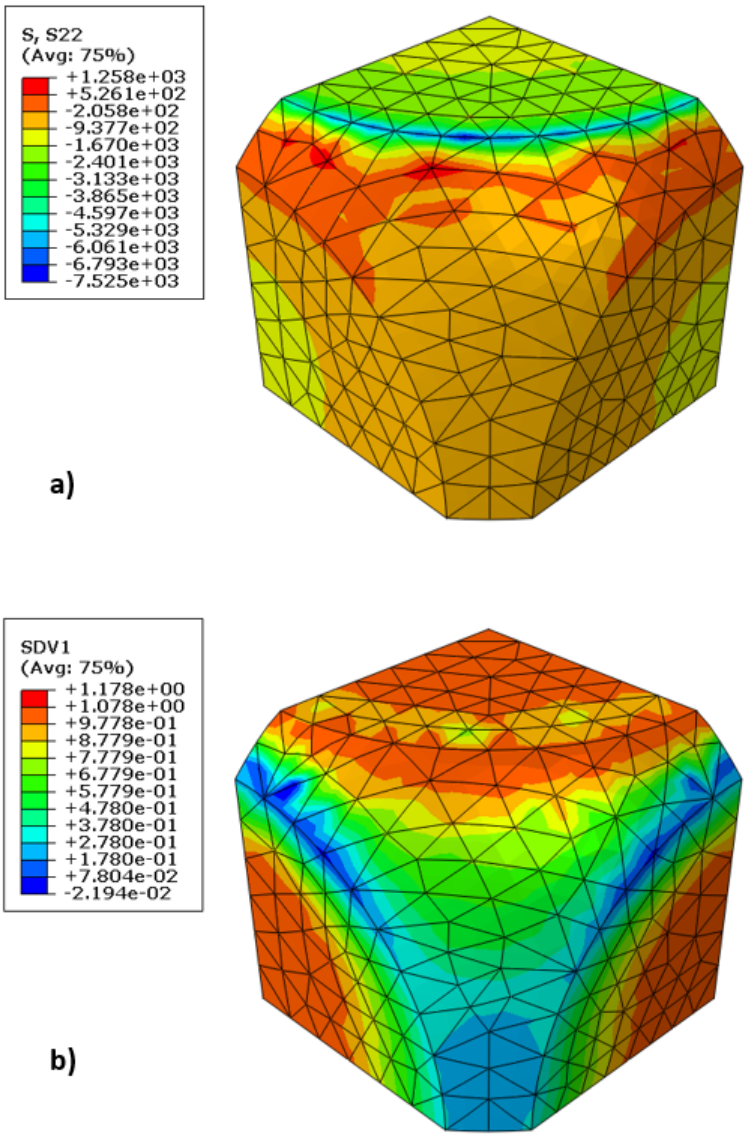

Figure 5.6: Distributions of a) axial stress and b) martensitic volume fraction in the UC at the end of the loading step.

In Figure 5.7, numerical approaches are compared in terms of their predictions on

the evolution of porosity. To estimate the evolution of the porosity using the unit-cell model, the total volume of the unit cell (V_{tot}) and its solid part (V^s_{tot}) at each increment are needed. The total volume of the solid part can be calculated as sum of the element's volumes provided as a field output by Abaqus. The total volume of the unit-cell is approximated by multiplying the edge lengths (L_x, L_y, L_z) of the UC at each increment. The porosity is then calculated with the formula $\phi = (V_{tot} - V^s_{tot})/V_{tot}$. On the other hand, the porosity is an internal state variable in the effective model, therefore, it is automatically recorded as a user-defined variable through the UMAT. According to Figure 5.7, the numerical results are close to each other; there is a maximum 7% difference between the numerical predictions of the models.

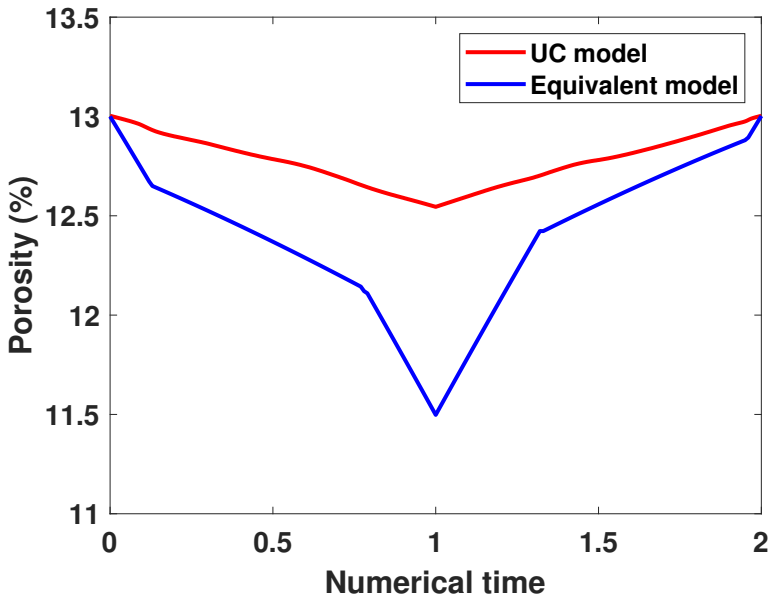

Figure 5.7: Numerical predictions of the unit-cell and the equivalent models for the evolution of porosity during loading/unloading of initially 13% porous NiTi alloy.

As a conclusion, the phenomenological model proposed in Chapter 4 is validated using both experimental results from literature and the numerical results obtained from the unit-cell model. The effective model can provide numerical estimates very close to the unit cell model. When compared to the unit-cell modeling, it is found very practical to estimate the global results of porous SMAs such as stress-strain, phase transformation or evolution of porosity.

6. CONCLUSION

This thesis provides a comprehensive investigation of the shape memory characteristics and the mechanical behavior of NiTi alloys produced using powder metallurgy. The experimental part of the study contributes to the literature of spark plasma sintered NiTi alloys by analyzing the effect of heat treatment on phase transformation, pseudoelastic deformation and shape memory effect. In the modeling part, a new constitutive model for the mechanical behavior of porous NiTi SMAs is proposed. Main findings of the present work and the future direction are summarized as follows:

Transformation characteristics of the powder manufactured NiTi alloy depends on many parameters related to the initial powder, and its processing. The sintering parameters applied to the present NiTi powders to increase sample density were significantly different from those reported in the literature for a similar powder size. It is recognized that even the size of the sintering mold has a significant effect on the sintering parameters, hence the resulting microstructure and the shape memory behavior. In this study, NiTi compacts did not show the shape memory characteristics readily, and needed to post-treatment after spark plasma sintering. The sintered compacts were heat treated in three categories: in the first category, the samples were subjected to aging around an hour, without any homogenization. In the second category, the samples were subjected to 2 h of homogenization and then an hour of aging. In the third category, the samples were subjected to longer homogenization (5 h) and aging (1-24 h). Effect of different aging temperatures and duration were tested through various analyzes. According to the results, the spark plasma sintered NiTi alloy responded to heat treatment similar to the bulk NiTi in the literature. The calorimetric (DSC) and microscopic (XRD, SEM, EDX) analyzes have shown the microstructural evolution: aging without prior homogenization resulted in a heterogeneous microstructure, therefore, identification of the transformation sequence and the temperatures were difficult. Homogenization and then aging in a certain temperature interval resulted in the DSC plots with expected phase transformation peaks between austenite, marten-

site and R-phases. The target of aging was to achieve the age (precipitation) hardening mechanism, therefore to increase the strength of the alloy. In NiTi alloys, precipitation hardening is accompanied with formation of the intermediate R-phase. DSC plots of the homogenized and then aged samples have shown the indication of the R-phase formation. The R-phase was clearly detected in the XRD spectrum of the sample which was subjected to 5 h of homogenization, and then 24 h of aging at 350°C. The effect of age hardening was quantified by the hardness measurements obtained through instrumented micro-indentation; this heat treatment yield a pronounced increase in the hardness. It is important that the age hardening mechanism was only effective when the samples were subjected to homogenization treatment prior to aging.

Stress-strain responses of the heat treated samples were tested through uniaxial compression. According to the results, the pseudoelastic strain recovery was improved through heat treatment in accordance with the hardening mechanism. The highest strain recovery was achieved from the sample which was subjected to the long time homogenization and aging, which increased the hardness. Nevertheless, the samples have shown partial pseudoelastic behavior. It was attributed to the low Ni concentration in the NiTi matrix (49-50 at.%) according to EDX measurements. The EDX analyzes also showed that the long time heat treatment in the air has resulted a severe oxidation on the specimen surface. The surface oxidation of NiTi alloys is a common technique to prevent excessive Ni release from the matrix, which is critical for biomedical applications. However, an initial heat treatment of the SPSed NiTi in a vacuum environment, and then a short time aging in the air would be more preferential since severe oxidation might affect the inner microstructure as well. According to the experimental analyzes mentioned above, lower powder size, higher Ni concentration and eliminating excessive oxidation were found favorable to enhance the shape memory characteristics, especially the pseudoelastic behavior, of NiTi alloys obtained through spark plasma sintering. Finally, it is observed that the SPSed NiTi shows almost a perfect shape memory effect. The residual strains at the end of unloading were removed by reheating the samples above A_f, and then cooling back to the room temperature regardless of the heat treatment applied.

In Chapters 4 and 5, the mechanical behavior of porous NiTi alloy is studied numerically. A new phenomenological (effective) model has been proposed which includes the porosity as an internal state variable similar to the poromechanics approach developed by O. Coussy [52]. The effective model was validated using experimental results from the literature, and numerical results obtained from the unit cell method presented in Chapter 5. It is shown that the uniaxial stress-strain simulations obtained with the effective model provides a good agreement with the experimental data, as well as with the predictions of the unit cell model, when there is inelastic deformation as well. The proposed model is found a more practical way to estimate the global behavior of porous NiTi alloys since the unit cell technique requires a significant computation time. On the other hand, the effective model cannot provide local stress-strain distribution around the pores which can be studied by using the unit cell model. The numerical results obtained with the effective phenomenological model can be improved by considering different pore shapes through the micromechanical homogenization technique (Mori-Tanaka) adopted in the model. It gives a great potential to the phenomenological model to study on the shape optimization of porous NiTi alloys. On the other hand, simulation of more complex loading cases, including the plastic deformation of pores, with the proposed model can be considered as a future study.

The phenomenological model, together with Mori-Tanaka homogenization, approximates the effective stiffness of porous structures in a reasonable extent. However, the model results deviate from the experimental ones when the porosity increases; the Mori-Tanaka homogenization appears to be more powerful for smaller amounts of porosity. A future study can be carried out to improve the predictions of the model for the effective stiffness when the porosity is larger. On the other hand, the numerical results obtained for the compressive strength of the porous NiTis were very close to the experimental results; the model were successful even in the range of the compressive strength of the human bone.

The poromechanics-based formulation can be very useful in possible biomedical applications of porous NiTi SMAs. It would be of special importance to combine the

present model, which is based on the skeleton deformation, with fluid state equations to simulate the mechanical behavior of NiTi-based implants under real operating conditions (in the human body). The capability of the effective model to differentiate the deformation of the skeleton and the pores is worth noting.

REFERENCES

1. Otsuka, K. and X. Ren, "Physical Metallurgy of Ti-Ni-based Shape Memory Alloys", *Progress in Materials Science*, Vol. 50, No. 5, pp. 511–678, 2005.

2. Patoor, E., D. C. Lagoudas, P. B. Entchev, L. C. Brinson and X. Gao, "Shape Memory Alloys, Part I: General Properties and Modeling of Single Crystals", *Mechanics of Materials*, Vol. 38, No. 5, pp. 391–429, 2006.

3. Silberstein, B. M. and V. Gunter, "Shape-memory Implants in Spinal Surgery: Long-term Results (Experimental and Clinical Studies)", *Shape Memory Implants*, pp. 147–152, Springer, 2000.

4. Elahinia, M. H., M. Hashemi, M. Tabesh and S. B. Bhaduri, "Manufacturing and Processing of NiTi Implants: A Review", *Progress in Materials Science*, Vol. 57, No. 5, pp. 911–946, 2012.

5. Bansiddhi, A., T. Sargeant, S. Stupp and D. Dunand, "Porous NiTi for Bone Implants: A Review", *Acta Biomaterialia*, Vol. 4, No. 4, pp. 773–782, 2008.

6. Chen, L.-J., L. Ting, Y.-m. Li, H. Hao and Y.-h. Hu, "Porous Titanium Implants Fabricated by Metal Injection Molding", *Transactions of Nonferrous Metals Society of China*, Vol. 19, No. 5, pp. 1174–1179, 2009.

7. Yuan, B., M. Zhu and C. Y. Chung, "Biomedical Porous Shape Memory Alloys for Hard-tissue Replacement Materials", *Materials*, Vol. 11, No. 9, p. 1716, 2018.

8. Bram, M., A. Ahmad-Khanlou, A. Heckmann, B. Fuchs, H. Buchkremer and D. Stöver, "Powder Metallurgical Fabrication Processes for NiTi Shape Memory Alloy Parts", *Materials Science and Engineering: A*, Vol. 337, No. 1-2, pp. 254–263, 2002.

9. Zhu, S., X. Yang, F. Hu, S. Deng and Z. Cui, "Processing of Porous TiNi Shape Memory Alloy from Elemental Powders by Ar-sintering", *Materials Letters*, Vol. 58, No. 19, pp. 2369–2373, 2004.

10. Van Humbeeck, J., "Additive Manufacturing of Shape Memory Alloys", *Shape Memory and Superelasticity*, Vol. 4, No. 2, pp. 309–312, 2018.

11. Torres, Y., J. J. Pavón, I. Nieto and J. A. Rodríguez, "Conventional Powder Metallurgy Process and Characterization of Porous Titanium for Biomedical Applications", *Metallurgical and Materials Transactions B: Process Metallurgy and Materials Processing Science*, Vol. 42, No. 4, pp. 891–900, 2011.

12. Zhang, Y., *Low Cycle Fatigue of Shape Memory Alloys*, Ph.D. Thesis, Université Paris-Saclay (ComUE), 2018.

13. Lexcellent, C., S. Leclercq, B. Gabry and G. Bourbon, "The Two Way Shape Memory Effect of Shape Memory Alloys: An Experimental Study and A Phenomenological Model", *International Journal of Plasticity*, Vol. 16, No. 10-11, pp. 1155–1168, 2000.

14. Liu, Y., Y. Liu and J. Van Humbeeck, "Two-way Shape Memory Effect Developed by Martensite Deformation in NiTi", *Acta Materialia*, Vol. 47, No. 1, pp. 199–209, 1998.

15. Zaki, W. and Z. Moumni, "A Three-dimensional Model of the Thermomechanical Behavior of Shape Memory Alloys", *Journal of the Mechanics and Physics of Solids*, Vol. 55, No. 11, pp. 2455–2490, 2007.

16. Liu, Y. and S. P. Galvin, "Criteria for Pseudoelasticity in Near-equiatomic NiTi Shape Memory Alloys", *Acta Materialia*, Vol. 45, No. 11, pp. 4431–4439, 1997.

17. Zhu, S., X. Yang, D. Fu, L. Zhang, C. Li and Z. Cui, "Stress–strain behavior of porous NiTi alloys prepared by powders sintering", *Materials Science and Engi-*

neering: A, Vol. 408, No. 1-2, pp. 264–268, 2005.

18. Bansiddhi, A. and D. C. Dunand, "Shape-memory NiTi Foams Produced by Solid-state Replication with NaF", *Intermetallics*, Vol. 15, No. 12, pp. 1612–1622, 2007.

19. Zhao, Y., M. Taya, Y. Kang and A. Kawasaki, "Compression Behavior of Porous NiTi Shape Memory Alloy", *Acta Materialia*, Vol. 53, No. 2, pp. 337–343, 2005.

20. Nemat-Nasser, S., Y. Su, W.-G. Guo and J. Isaacs, "Experimental Characterization and Micromechanical Modeling of Superelastic Response of a Porous NiTi Shape-Memory Alloy", *Journal of the Mechanics and Physics of Solids*, Vol. 53, No. 10, pp. 2320–2346, 2005.

21. Bram, M., M. Köhl, H. P. Buchkremer and D. Stöver, "Mechanical Properties of Highly Porous NiTi Alloys", *Journal of Materials Engineering and Performance*, Vol. 20, No. 4-5, pp. 522–528, 2011.

22. Guo, Z., H. Xie, F. Dai, H. Qiang, L. Rong, P. Chen and F. Huang, "Compressive Behavior of 64% Porosity NiTi Alloy: An Experimental Study", *Materials Science and Engineering: A*, Vol. 515, No. 1-2, pp. 117–130, 2009.

23. Saedi, S., S. E. Saghaian, A. Jahadakbar, N. S. Moghaddam, M. T. Andani, S. M. Saghaian, Y. C. Lu, M. Elahinia and H. E. Karaca, "Shape Memory Response of Porous NiTi Shape Memory Alloys Fabricated by Selective Laser Melting", *Journal of Materials Science: Materials in Medicine*, Vol. 29, No. 4, p. 40, 2018.

24. Lagoudas, D. C. and E. L. Vandygriff, "Processing and Characterization of NiTi Porous SMA by Elevated Pressure Sintering", *Journal of Intelligent Material Systems and Structures*, Vol. 13, No. 12, pp. 837–850, 2002.

25. Greiner, C., S. M. Oppenheimer and D. C. Dunand, "High Strength, Low Stiffness, Porous NiTi with Superelastic Properties", *Acta Biomaterialia*, Vol. 1, No. 6, pp. 705–716, 2005.

26. Chen, G., K.-D. Liss and P. Cao, "In Situ Observation and Neutron Diffraction of NiTi Powder Sintering", *Acta Materialia*, Vol. 67, pp. 32–44, 2014.

27. Li, D. S., Y. P. Zhang, G. Eggeler and X. P. Zhang, "High Porosity and High-strength Porous NiTi Shape Memory Alloys with Controllable Pore Characteristics", *Journal of Alloys and Compounds*, Vol. 470, No. 1-2, pp. 5–9, 2009.

28. Saedi, S., S. E. Saghaian, A. Jahadakbar, N. Shayesteh Moghaddam, M. Taheri Andani, S. M. Saghaian, Y. C. Lu, M. Elahinia and H. E. Karaca, "Shape Memory Response of Porous NiTi Shape Memory Alloys Fabricated by Selective Laser Melting", *Journal of Materials Science: Materials in Medicine*, Vol. 29, No. 4, 2018.

29. Ashrafi, M. J., J. Arghavani, R. Naghdabadi and F. Auricchio, "A Three-dimensional Phenomenological Constitutive Model for Porous Shape Memory Alloys Including Plasticity Effects", *Journal of Intelligent Material Systems and Structures*, Vol. 27, No. 5, pp. 608–624, 2016.

30. Zhang, L., Y. Zhang, Y. Jiang and R. Zhou, "Superelastic Behaviors of Biomedical Porous NiTi Alloy with High Porosity and Large Pore Size Prepared by Spark Plasma Sintering", *Journal of Alloys and Compounds*, Vol. 644, pp. 513–522, 2015.

31. Sepe, V., F. Auricchio, S. Marfia and E. Sacco, "Homogenization Techniques for the Analysis of Porous SMA", *Computational Mechanics*, Vol. 57, No. 5, pp. 755–772, 2016.

32. Entchev, P. B. and D. C. Lagoudas, "Modeling of Transformation-induced Plasticity and Its Effect on the Behavior of Porous Shape Memory Alloys. Part II: Porous SMA Response", *Mechanics of Materials*, Vol. 36, No. 9, pp. 893–913, 2004.

33. Zhao, Y. and M. Taya, "Analytical Modeling for Stress-strain Curve of a Porous NiTi", *Journal of Applied Mechanics*, Vol. 74, No. 2, pp. 291–297, 2007.

34. Zhu, Y., "A Model Considering Hydrostatic Stress of Porous NiTi Shape Memory Alloy", *Acta Mechanica Solida Sinica*, Vol. 24, No. 4, pp. 289–298, 2011.

35. Gong, S., Z. Li and Y. Zhao, "An Extended Mori–Tanaka Model for the Elastic Moduli of Porous materials of Finite Size", *Acta Materialia*, Vol. 59, No. 17, pp. 6820–6830, 2011.

36. Qidwai, M. A., P. B. Entchev, D. C. Lagoudas and V. G. DeGiorgi, "Modeling of the Thermomechanical Behavior of Porous Shape Memory Alloys", *International Journal of Solids and Structures*, Vol. 38, No. 48-49, pp. 8653–8671, 2001.

37. Ravari, M. K., M. Kadkhodaei and A. Ghaei, "A Unit Cell Model for Simulating the Stress-Strain Response of Porous Shape Memory Alloys", *Journal of Materials Engineering and Performance*, Vol. 24, No. 10, pp. 4096–4105, 2015.

38. Cissé, C., W. Zaki and T. Ben Zineb, "Development and Implementation of an Effective Constitutive Model for Architected Cellular Iron-based Shape Memory Alloys: Pressure Dependency and Transformation-Plasticity Interaction", *Journal of Intelligent Material Systems and Structures*, Vol. 30, No. 12, pp. 1789–1822, 2019.

39. Panico, M. and L. C. Brinson, "Computational Modeling of Porous Shape Memory Alloys", *International Journal of Solids and Structures*, Vol. 45, No. 21, pp. 5613–5626, 2008.

40. Zhu, S., C. Bouby, A. Cherouat and T. B. Zineb, "3D Reconstitution and Numerical Analysis of Superelastic Behavior of Porous Shape Memory Alloy", *International Journal of Solids and Structures*, Vol. 168, pp. 109–122, 2019.

41. DeGiorgi, V. G. and M. A. Qidwai, "A Computational Mesoscale Evaluation of

Material Characteristics of Porous Shape Memory Alloys", *Smart Materials and Structures*, Vol. 11, No. 3, p. 435, 2002.

42. Deshpande, V. S. and N. A. Fleck, "Isotropic Constitutive Models for Metallic Foams", *Journal of the Mechanics and Physics of Solids*, Vol. 48, No. 6, pp. 1253–1283, 2000.

43. Gibson, L., "Mechanical Behavior of Metallic Foams", *Annual Review of Materials Science*, Vol. 30, No. 1, pp. 191–227, 2000.

44. Ashrafi, M., J. Arghavani, R. Naghdabadi and S. Sohrabpour, "A 3-D Constitutive Model for Pressure-dependent Phase Transformation of Porous Shape Memory Alloys", *Journal of the Mechanical Behavior of Biomedical Materials*, Vol. 42, pp. 292–310, 2015.

45. Ashrafi, M., J. Arghavani, R. Naghdabadi and F. Auricchio, "A Three-dimensional Phenomenological Constitutive Model for Porous Shape Memory Alloys Including Plasticity Effects", *Journal of Intelligent Material Systems and Structures*, Vol. 27, No. 5, pp. 608–624, 2016.

46. Olsen, J. S. and Z. L. Zhang, "Effect of Spherical Micro-voids in Shape Memory Alloys Subjected to Uniaxial Loading", *International Journal of Solids and Structures*, Vol. 49, No. 14, pp. 1947–1960, 2012.

47. Gurson, A. L., "Continuum Theory of Ductile Rupture by Void Nucleation and Growth", *Journal of Engineering Materials and Technology*, Vol. 99, No. 76, pp. 2–15, 1977.

48. Halphen, B. and Q. S. Nguyen, "Sur les Matériaux Standard Généralisés", *Journal de Mécanique*, Vol. 14, No. 1, pp. 39–63, 1975.

49. Viet, N. and W. Zaki, "A Thermomechanical Constitutive Model for Porous SMAs Accounting for the Influence of Void Evolution", *Mechanics of Materials*, Vol. 155,

p. 103779, 2021.

50. Safaei, K., H. Abedi, M. Nematollahi, F. Kordizadeh, H. Dabbaghi, P. Bayati, R. Javanbakht, A. Jahadakbar, M. Elahinia and B. Poorganji, "Additive Manufacturing of NiTi Shape Memory Alloy for Biomedical Applications: Review of the LPBF Process Ecosystem", *JOM*, pp. 1–16, 2021.

51. Zaki, W., S. Zamfir and Z. Moumni, "An Extension of the ZM Model for Shape Memory Alloys Accounting for Plastic Deformation", *Mechanics of Materials*, Vol. 42, No. 3, pp. 266–274, 2010.

52. Coussy, O., *Poromechanics*, John Wiley & Sons, 2004.

53. Ye, L. L., Z. G. Liu, K. Raviprasad, M. X. Quan, M. Umemoto and Z. Q. Hu, "Consolidation of MA Amorphous NiTi Powders by Spark Plasma Sintering", *Materials Science and Engineering A*, Vol. 241, No. 1-2, pp. 290–293, 1998.

54. Liu, B., S. Huang, L. Chen, J. Van Humbeeck and J. Vleugels, "Rapid Synthesis of Dense NiTi Alloy Through Spark Plasma Sintering of a TiH2/Ni Powder Mixture", *Materials Letters*, Vol. 191, pp. 89–92, 2017.

55. Velmurugan, C., V. Senthilkumar, K. Biswas and S. Yadav, "Densification and Microstructural Evolution of Spark Plasma Sintered NiTi Shape Memory Alloy", *Advanced Powder Technology*, Vol. 29, No. 10, pp. 2456–2462, 2018.

56. Shearwood, C., Y. Q. Fu, L. Yu and K. A. Khor, "Spark Plasma Sintering of TiNi Nano-powder", *Scripta Materialia*, Vol. 52, No. 6, pp. 455–460, 2005.

57. Salvetr, P., T. F. Kubatík, D. Pignol and P. Novák, "Fabrication of Ni-Ti Alloy by Self-Propagating High-Temperature Synthesis and Spark Plasma Sintering Technique", *Metallurgical and Materials Transactions B: Process Metallurgy and Materials Processing Science*, Vol. 48, No. 2, pp. 772–778, 2017.

58. Yuan, B., X. P. Zhang, C. Y. Chung and M. Zhu, "The Effect of Porosity on Phase Transformation Behavior of Porous Ti-50.8 at.% Ni Shape Memory Alloys Prepared by Capsule-free Hot Isostatic Pressing", *Materials Science and Engineering A*, Vol. 438-440, pp. 585–588, 2006.

59. Khalil-Allafi, J., A. Dlouhy and G. Eggeler, "Ni4Ti3-Precipitation During Aging of NiTi Shape Memory Alloys and Its Influence on Martensitic Phase Transformations", *Acta Materialia*, Vol. 50, No. 17, pp. 4255–4274, 2002.

60. Gall, K., K. Juntunen, H. J. Maier, H. Sehitoglu and Y. I. Chumlyakov, "Instrumented Micro-indentation of NiTi Shape-Memory Alloys", *Acta Materialia*, Vol. 49, No. 16, pp. 3205–3217, 2001.

61. Dlouhy, A., J. Khalil-Allafi and G. Eggeler, "Multiple-step Martensitic Transformations in Ni-rich NiTi Alloys–A in-situ Transmission Electron Microscopy Investigation", *Philosophical Magazine*, Vol. 83, No. 3, pp. 339–363, 2003.

62. Frick, C. P., A. M. Ortega, J. Tyber, A. E. M. Maksound, H. J. Maier, Y. Liu and K. Gall, "Thermal Processing of Polycrystalline NiTi Shape Memory Alloys", *Materials Science and Engineering A*, Vol. 405, No. 1-2, pp. 34–49, 2005.

63. Nemat-Nasser, S., Y. Su, W. G. Guo and J. Isaacs, "Experimental Characterization and Micromechanical Modeling of Superelastic Response of a Porous NiTi Shape-Memory Alloy", *Journal of the Mechanics and Physics of Solids*, Vol. 53, No. 10, pp. 2320–2346, 2005.

64. Butler, J., P. Tiernan, A. Gandhi, K. McNamara and S. Tofail, "Production of Nitinol Wire from Elemental Nickel and Titanium Powders Through Spark Plasma Sintering and Extrusion", *Journal of Materials Engineering and Performance*, Vol. 20, No. 4-5, pp. 757–761, 2011.

65. Soba, R., Y. Tanabe, T. Yonezawa, J. Umeda and K. Kondoh, "Microstructures

and Mechanical Properties of Shape Memory Alloy Using Pre-mixed TiNi Powders with TiO2 Particles", *Funtai Oyobi Fummatsu Yakin/Journal of the Japan Society of Powder and Powder Metallurgy*, Vol. 64, No. 11, pp. 589–594, 2017.

66. Salvetr, P., J. Dlouhỳ, A. Školáková, F. Prša, P. Novák, M. Karlík and P. Haušild, "Influence of Heat Treatment on Microstructure and Properties of NiTi46 Alloy Consolidated by Spark Plasma Sintering", *Materials*, Vol. 12, No. 24, p. 4075, 2019.

67. Zhang, L., Z. Y. He, Y. Q. Zhang, Y. H. Jiang and R. Zhou, "Enhanced in Vitro Bioactivity of Porous NiTi-HA Composites with Interconnected Pore Characteristics Prepared by Spark Plasma Sintering", *Materials and Design*, Vol. 101, pp. 170–180, 2016.

68. Zhao, Y. and M. Taya, "Processing of Porous NiTi by Spark Plasma Sintering Method", *Smart Structures and Materials 2006: Active Materials: Behavior and Mechanics*, Vol. 6170, No. April 2006, p. 617013, 2006.

69. Zhang, L., Z. He, J. Tan, Y. Zhang, M. Stoica, K. Prashanth, M. Cordill, Y. Jiang, R. Zhou and J. Eckert, "Rapid fabrication of function-structure-integrated NiTi alloys: Towards a Combination of Excellent Superelasticity and Favorable Bioactivity", *Intermetallics*, Vol. 82, pp. 1–13, 2017.

70. McNeese, M. D., D. C. Lagoudas and T. C. Pollock, "Processing of TiNi from elemental powders by hot isostatic pressing", *Materials Science and Engineering A*, Vol. 280, No. 2, pp. 334–348, 2000.

71. Saedi, S., A. S. Turabi, M. T. Andani, C. Haberland, H. Karaca and M. Elahinia, "The Influence of Heat Treatment on the Thermomechanical Response of Ni-rich NiTi Alloys Manufactured by Selective Laser Melting", *Journal of Alloys and Compounds*, Vol. 677, pp. 204–210, 2016.

72. Munir, Z., U. Anselmi-Tamburini and M. Ohyanagi, "The Effect of Electric Field and Pressure on the Synthesis and Consolidation of Materials: A review of the Spark Plasma Sintering Method", *Journal of Materials Science*, Vol. 41, No. 3, pp. 763–777, 2006.

73. Olevsky, E. A., W. L. Bradbury, C. D. Haines, D. G. Martin and D. Kapoor, "Fundamental Aspects of Spark Plasma Sintering: I. Experimental Analysis of Scalability", *Journal of the American Ceramic Society*, Vol. 95, No. 8, pp. 2406–2413, 2012.

74. Standard, A., "E399, Standard Test Method for Linear-Elastic Plane-Strain Fracture Toughness KIC of Metallic Materials", *ASTM book of standards, West Conshohocken, PA. ASTM International*, 2012.

75. Yu, Z., Z. Xu, Y. Guo, R. Xin, R. Liu, C. Jiang, L. Li, Z. Zhang and L. Ren, "Study on Properties of SLM-NiTi Shape Memory Alloy Under the Same Energy Density", *Journal of Materials Research and Technology*, Vol. 13, pp. 241–250, 2021.

76. Schöller, E., L. Krone, M. Bram, H. Buchkremer and D. Ståaver, "Metal Injection Molding of Shape Memory Alloys Using Prealloyed NiTi Powders", *Journal of Materials Science*, Vol. 40, No. 16, pp. 4231–4238, 2005.

77. Schüller, E., M. Bram, H. Buchkremer and D. Stöver, "Phase Transformation Temperatures for NiTi Alloys Prepared by Powder Metallurgical Processes", *Materials Science and Engineering: A*, Vol. 378, No. 1-2, pp. 165–169, 2004.

78. Saedi, S., A. S. Turabi, M. T. Andani, C. Haberland, M. Elahinia and H. Karaca, "Thermomechanical Characterization of Ni-rich NiTi Fabricated by Selective Laser Melting", *Smart Materials and Structures*, Vol. 25, No. 3, p. 035005, 2016.

79. Mentz, J., J. Frenzel, M. F. Wagner, K. Neuking, G. Eggeler, H. P. Buchkremer

and D. Stöver, "Powder Metallurgical Processing of NiTi Shape Memory Alloys with Elevated Transformation Temperatures", *Materials Science and Engineering A*, Vol. 491, No. 1-2, pp. 270–278, 2008.

80. Otsuka, K. and C. M. Wayman, *Shape Memory Materials*, Cambridge University Press, 1999.

81. Aboutalebi, M. R., M. Karimzadeh, M. T. Salehi, S. M. Abbasi and M. Morakabati, "Influences of Aging and Thermomechanical Treatments on the Martensitic Transformation and Superelasticity of Highly Ni-rich Ti-51.5 at.% Ni Shape Memory Alloy", *Thermochimica Acta*, Vol. 616, pp. 14–19, 2015.

82. Foroozmehr, A., A. Kermanpur, F. Ashrafizadeh and Y. Kabiri, "Investigating Microstructural Evolution During Homogenization of the Equiatomic NiTi Shape Memory Alloy Produced by Vacuum Arc Remelting", *Materials Science and Engineering: A*, Vol. 528, No. 27, pp. 7952–7955, 2011.

83. Saedi, S., A. S. Turabi, M. T. Andani, N. S. Moghaddam, M. Elahinia and H. E. Karaca, "Texture, Aging, and Superelasticity of Selective Laser Melting Fabricated Ni-rich NiTi Alloys", *Materials Science and Engineering A*, Vol. 686, No. January, pp. 1–10, 2017.

84. Chu, C. L., J. C. Chung and P. K. Chu, "Effects of Heat Treatment on Characteristics of Porous Ni-rich NiTi SMA Prepared by SHS Technique", *Transactions of Nonferrous Metals Society of China (English Edition)*, Vol. 16, No. 1, pp. 49–53, 2006.

85. Qin, R., F. Jiang, M. Cao, Y. Li, H. Zhang, C. Guo and Z. Wang, "Preparation, Microstructure and Compressive Property of NiTi Alloy Hollow Spheres Fabricated by Powder Metallurgy", *Materials Today Communications*, Vol. 30, p. 103039, 2022.

86. Bram, M., A. Ahmad-Khanlou, A. Heckmann, B. Fuchs, H. P. Buchkremer and D. Stöver, "Powder Metallurgical Fabrication Processes for NiTi Shape Memory Alloy Parts", *Materials Science and Engineering A*, Vol. 337, No. 1-2, pp. 254–263, 2002.

87. Pattabi, M., K. Ramakrishna and K. Mahesh, "Effect of Thermal Cycling on the Shape Memory Transformation Behavior of NiTi Alloy: Powder X-ray Diffraction Study", *Materials Science and Engineering: A*, Vol. 448, No. 1-2, pp. 33–38, 2007.

88. Kim, J., Y. Liu and S. Miyazaki, "Ageing-induced Two-stage R-phase Transformation in Ti–50.9 at.% Ni", *Acta Materialia*, Vol. 52, No. 2, pp. 487–499, 2004.

89. Silva, J. D., S. C. Martins, N. I. de Azevedo Lopes, P. D. Resende, L. A. Santos and V. T. L. Buono, "Effects of Aging Treatments on the Fatigue Resistance of Superelastic NiTi Wires", *Materials Science and Engineering: A*, Vol. 756, pp. 54–60, 2019.

90. Uchil, J., F. B. Fernandes and K. Mahesh, "X-ray Diffraction Study of the Phase Transformations in NiTi Shape Memory Alloy", *Materials Characterization*, Vol. 58, No. 3, pp. 243–248, 2007.

91. Vojtěch, D., M. Voděrová, J. Fojt, P. Novák and T. Kubásek, "Surface Structure and Corrosion Resistance of Short-time Heat-treated NiTi Shape Memory Alloy", *Applied Surface Science*, Vol. 257, No. 5, pp. 1573–1582, 2010.

92. Firstov, G., R. Vitchev, H. Kumar, B. Blanpain and J. Van Humbeeck, "Surface Oxidation of NiTi Shape Memory Alloy", *Biomaterials*, Vol. 23, No. 24, pp. 4863–4871, 2002.

93. Mahmud, A., Z. Wu, J. Zhang, Y. Liu and H. Yang, "Surface Oxidation of NiTi and Its Effects on Thermal and Mechanical Properties", *Intermetallics*, Vol. 103, pp. 52–62, 2018.

94. Chu, C., S. Wu and Y. Yen, "Oxidation Behavior of Equiatomic TiNi Alloy in High Temperature Air Environment", *Materials Science and Engineering: A*, Vol. 216, No. 1-2, pp. 193–200, 1996.

95. Plant, S. D., D. M. Grant and L. Leach, "Behaviour of Human Endothelial Cells on Surface Modified NiTi Alloy", *Biomaterials*, Vol. 26, No. 26, pp. 5359–5367, 2005.

96. Liu, R., D. Li, Y. Xie, R. Llewellyn and H. Hawthorne, "Indentation Behavior of Pseudoelastic TiNi Alloy", *Scripta Materialia*, Vol. 41, No. 7, pp. 691–696, 1999.

97. Samal, S., O. Molnárová, F. Prša, J. Kopeček, L. Heller, P. Šittner, M. Škodová, L. Abate and I. Blanco, "Net-shape NiTi Shape Memory Alloy by Spark Plasma Sintering Method", *Applied Sciences*, Vol. 11, No. 4, p. 1802, 2021.

98. Simo, J. C. and T. J. Hughes, *Computational Inelasticity*, Vol. 7, Springer Science & Business Media, 2006.

99. Maitournam, H., *Matériaux et Structures Anélastiques*, 2017.

100. Zaki, W., *Comportement Thermo-mécanique des Matériaux à Mémoire de Forme: Modélisation Macroscopique, Chargement Cyclique et Fatigue*, Ph.D. Thesis, Ecole Polytechnique, 2006.

101. Qu, J. and M. Cherkaoui, *Fundamentals of Micromechanics of Solids*, Wiley Hoboken, 2006.

102. Mura, T., *Micromechanics of Defects in Solids*, Springer Science & Business Media, 2013.

103. Gu, X., W. Zaki, C. Morin, Z. Moumni and W. Zhang, "Time Integration and Assessment of a Model for Shape Memory Alloys Considering Multiaxial Nonproportional Loading Cases", *International Journal of Solids and Structures*, Vol. 54,

pp. 82–99, 2015.

104. Ezaz, T., J. Wang, H. Sehitoglu and H. Maier, "Plastic Deformation of NiTi Shape Memory Alloys", *Acta Materialia*, Vol. 61, No. 1, pp. 67–78, 2013.

105. Šittner, P., P. Sedlák, H. Seiner, P. Sedmák, J. Pilch, R. Delville, L. Heller and L. Kadeřávek, "On the Coupling Between Martensitic Transformation and Plasticity in NiTi: Experiments and Continuum Based Modelling", *Progress in Materials Science*, Vol. 98, pp. 249–298, 2018.

106. Li, S., "Boundary Conditions for Unit Cells from Periodic Microstructures and Their Implications", *Composites Science and technology*, Vol. 68, No. 9, pp. 1962–1974, 2008.

107. Li, S. and A. Wongsto, "Unit Cells for Micromechanical Analyses of Particle-reinforced Composites", *Mechanics of Materials*, Vol. 36, No. 7, pp. 543–572, 2004.

108. Cissé, C., W. Zaki and T. Ben Zineb, "Development and Implementation of an Effective Constitutive Model for Architected Cellular Iron-based Shape Memory Alloys: Pressure Dependency and Transformation-Plasticity Interaction", *Journal of Intelligent Material Systems and Structures*, Vol. 30, No. 12, pp. 1789–1822, 2019.

109. Lubarda, V., "On Thermodynamic Potentials in Linear Thermoelasticity", *International Journal of Solids and Structures*, Vol. 41, No. 26, pp. 7377–7398, 2004.

APPENDIX A:

A.1. Theoretical Background on Constitutive Modeling

A.1.1. Thermoelastic Constitutive Relation

In thermoelasticity, thermodynamics and continuum mechanics are used together to determine the equilibrium state of a body by a finite number of independent variables, namely macroscopic (state) variables such as temperature (T) and strain (ε_{ij}).

When studying the deformation of solids, Helmholtz free energy $\psi(\varepsilon_{ij}, T)$ is used as a thermodynamic potential, related to the internal energy $u(\varepsilon_{ij}, s)$ by the relation

$$\psi = u - Ts. \tag{A.1}$$

By differentiating the free energy as

$$d\psi = du - sdT - Tds, \tag{A.2}$$

and using

$$du = \sigma_{ij} d\varepsilon_{ij} + Tds, \tag{A.3}$$

the incremental change of Helmholtz free energy is written as

$$d\psi = \sigma_{ij} d\varepsilon_{ij} - sdT. \tag{A.4}$$

This relation indicates the physical meaning of Helmholtz free energy: the incremental change in Helmholtz free energy is equal to the energy available to do work at constant temperature.

Since dψ is a total differential, following relations can be written:

$$\frac{\partial \psi}{\partial T} = -s, \tag{A.5}$$

$$\frac{\partial \psi}{\partial \varepsilon_{ij}} = \sigma_{ij}. \tag{A.6}$$

As shown, Helmholtz free energy is used as the thermodynamic potential for determining σ_{ij} and s when ε_{ij} and T are chosen as independent state variables [109].

The free energy ψ must therefore be formulated in terms of strain and temperature; it is needed in the derivation of stress-strain relation of thermoelastic bodies. Expansion of $\psi(\varepsilon_{i,j}, T)$ in the vicinity of $(\varepsilon^0_{ij}, T^0)$, i.e. the reference state, up to second order terms gives

$$\begin{aligned}\psi(\varepsilon_{i,j}, T) &= \psi^0(\varepsilon^0_{ij}, T^0) + \left(\frac{\partial \psi}{\partial \varepsilon_{ij}}\right)_{T^0} : (\varepsilon_{ij} - \varepsilon^0_{ij}) + \left(\frac{\partial \psi}{\partial T}\right)_{\varepsilon^0_{ij}} (T - T^0) \\ &+ \frac{1}{2}(\varepsilon_{ij} - \varepsilon^0_{ij}) : \left(\frac{\partial^2 \psi}{\partial \varepsilon_{ij} \partial \varepsilon_{mn}}\right)_{T^0} : (\varepsilon_{mn} - \varepsilon^0_{mn}) \\ &+ \frac{1}{2}\left(\frac{\partial^2 \psi}{\partial T^2}\right)_{\varepsilon^0_{ij}} (T - T^0)^2 + \left(\frac{\partial^2 \psi}{\partial \varepsilon_{ij} \partial T}\right)_{\varepsilon^0_{ij}, T^0} : (\varepsilon_{ij} - \varepsilon^0_{ij})(T - T^0)\end{aligned} \tag{A.7}$$

where $\varepsilon^0_{ij} = 0$ assuming initially stress free state. Using Equations A.5 and A.6 in Equation A.7,

$$\begin{aligned}\psi(\varepsilon_{i,j}, T) &= \psi^0(\varepsilon^0_{ij}, T^0) + \sigma^0_{ij} : \varepsilon_{ij} - s^0(T - T^0) + \frac{1}{2}\varepsilon_{ij} : \left(\frac{\partial \sigma_{mn}}{\partial \varepsilon_{ij}}\right) : \varepsilon_{mn} \\ &- \frac{1}{2}\left(\frac{\partial s}{\partial T}\right)_{\varepsilon^0_{ij}} (T - T^0)^2 - \left(\frac{\partial s}{\partial \varepsilon_{ij}}\right)_{\varepsilon^0_{ij}, T^0} : \varepsilon_{ij}(T - T^0)\end{aligned} \tag{A.8}$$

is obtained.

Thermodynamic relations give [109]

$$\left(\frac{\partial s}{\partial T}\right)_{\varepsilon_{ij}} = \left(\frac{\partial u}{\partial T}\right)_{\varepsilon_{ij}} = \frac{c_v}{T}, \tag{A.9}$$

and,

$$-\left(\frac{\partial s}{\partial \varepsilon_{ij}}\right)_T = \left(\frac{\partial \sigma_{ij}}{\partial T}\right)_{\varepsilon_{ij}} = -\kappa_T \alpha_0 \delta_{ij}, \tag{A.10}$$

where c_v and κ_T are the specific heat and the thermal expansion coefficient. Therefore,

$$\begin{aligned}\psi(\varepsilon_{i,j}, T) &= \psi^0(\varepsilon^0_{ij}, T^0) - s^0(T - T^0) + \frac{1}{2}\varepsilon_{ij} : \left(\frac{\partial \sigma_{mn}}{\partial \varepsilon_{ij}}\right) : \varepsilon_{mn} - \frac{c^0_v}{2T^0}(T - T^0)^2 \\ &\quad -\kappa_T \alpha_0 \varepsilon_{ij}\delta_{ij}(T - T^0).\end{aligned} \tag{A.11}$$

Introducing the following relation for linear-elastic materials,

$$\frac{\partial \sigma_{mn}}{\partial \varepsilon_{ij}} = K_{mnij}, \tag{A.12}$$

where K_{mnij} represents the elastic stiffness tensor, and $\varepsilon_{ij}\delta_{ij} = \varepsilon_{kk}$, the free energy function can be written as

$$\begin{aligned}\psi(\varepsilon_{i,j}, T) &= \psi^0(\varepsilon^0_{ij}, T^0) - s^0(T - T^0) + \frac{1}{2}\varepsilon_{ij} K_{mnij} \varepsilon_{mn} - \frac{c^0_v}{2T^0}(T - T^0)^2 \\ &\quad -\kappa_T \alpha_0 \varepsilon_{kk}(T - T^0).\end{aligned} \tag{A.13}$$

Using Equation A.6, the thermoelastic stress-strain relation for anisotropic materials is derived as

$$\sigma_{mn} = K_{mnij}\varepsilon_{ij} - \kappa_T \alpha_0 \delta_{mn}(T - T^0). \tag{A.14}$$

For the isotropic case, using Lame constants, the stress-strain relation for linearly elastic and homogeneous medium can be written as

$$\sigma_{mn} = 2\mu\varepsilon_{mn} + \lambda\varepsilon_{kk}\delta_{mn} - (3\lambda + 2\mu)\alpha_0 \delta_{mn}(T - T^0). \tag{A.15}$$

In terms of engineering constants, E and ν, the stress-strain relation takes the following

from:

$$\sigma_{mn} = \frac{E}{1+\nu}\left[\varepsilon_{mn} + \frac{\nu}{E}\sigma_{kk}\delta_{mn} - \frac{1}{3}\alpha_0(T-T^0)\delta_{mn}\right]. \tag{A.16}$$

Similarly, the strain can be written as

$$\varepsilon_{mn} = \frac{1+\nu}{E}\sigma_{mn} - \frac{\nu}{E}\sigma_{kk}\delta_{mn} + \frac{1}{3}\alpha_0(T-T^0)\delta_{mn}. \tag{A.17}$$

In Equation A.17, the last term represents the strain due to thermal expansion or contraction of a thermoelastic body.

The elastic part of strain can be obtained by subtracting the thermal part from the total one as follows:

$$\varepsilon^{el}_{mn} = \varepsilon_{mn} - \varepsilon^{th}_{mn}. \tag{A.18}$$

Therefore,

$$\varepsilon^{el}_{mn} = \frac{1+\nu}{E}\sigma_{mn} - \frac{\nu}{E}\sigma_{kk}\delta_{mn} \tag{A.19}$$

which can be written in the tensor form as

$$\boldsymbol{\varepsilon}^{el} = \boldsymbol{M} : \boldsymbol{\sigma} \quad \text{or} \quad \boldsymbol{\sigma} = \boldsymbol{K} : \boldsymbol{\varepsilon}^{el}, \tag{A.20}$$

where stiffness ($\boldsymbol{K}$) and compliance ($\boldsymbol{M}$) tensors are functions of the engineering constants E and ν.

Equation A.20 is in the form of the stress-strain relation derived for linear elastic bodies. It is shown by this derivation that this stress-strain relation can also be used for inelastically deformed bodies as long as the strain tensor represents the linear elastic portion of the total strain.

A.2. Summary of the Phenomenological SMA Model of Zaki and Moumni

In the followings, the summary of the phenomenological SMA model developed by Zaki and Moumni will be summarized. Additional detail can be found in [15] and [51].

Helmholtz free energy:

For the SMAs, the Helmholtz free energy is written as

$$\begin{aligned}\psi &\stackrel{\text{def}}{=} \psi(T, \boldsymbol{\varepsilon}_A, \boldsymbol{\varepsilon}_M, z, \boldsymbol{\varepsilon}_{ori}, \boldsymbol{\varepsilon}_{pl}) \\ &= (1-z)\left(\frac{1}{2}(\boldsymbol{\varepsilon}_A - \boldsymbol{\varepsilon}_{pl}) : \boldsymbol{K}_A : (\boldsymbol{\varepsilon}_A - \boldsymbol{\varepsilon}_{pl})\right) \\ &\quad + z\left(\frac{1}{2}(\boldsymbol{\varepsilon}_M - \boldsymbol{\varepsilon}_{ori} - \boldsymbol{\varepsilon}_{pl}) : \boldsymbol{K}_M : (\boldsymbol{\varepsilon}_M - \boldsymbol{\varepsilon}_{ori} - \boldsymbol{\varepsilon}_{pl})\big] + C(T)\right) \\ &\quad + \left(G\frac{z^2}{2} + \frac{z}{2}\big[\alpha z + \beta(1-z)\big]\big[\frac{2}{3}\boldsymbol{\varepsilon}_{ori} : \boldsymbol{\varepsilon}_{ori}\big]\right) + \frac{H_1}{2}(\frac{2}{3}\boldsymbol{\varepsilon}_{pl} : \boldsymbol{\varepsilon}_{pl}) \end{aligned} \tag{A.21}$$

that gives the stress-strain relation as

$$\boldsymbol{\sigma} = \boldsymbol{K}_{eqv} : (\boldsymbol{\varepsilon} - z\boldsymbol{\varepsilon}_{ori} - \boldsymbol{\varepsilon}_{pl}), \tag{A.22}$$

where

$$\boldsymbol{K}_{eqv} = \left[(1-z)\boldsymbol{K}_A^{-1} + z\boldsymbol{K}_M^{-1}\right]^{-1}. \tag{A.23}$$

Similarly, the thermodynamic forces are expressed as

$$\begin{aligned} A_z &= \frac{1}{2}\left(EL_{MA}\boldsymbol{s} : \boldsymbol{s} + (\frac{1}{3}EL_{MA} + P_{MA})tr(\boldsymbol{\sigma})^2\right) - C(T) + \boldsymbol{s} : \boldsymbol{\varepsilon}_{ori} \\ &\quad -Gz - [\alpha z + \beta(\frac{1}{2} - z)][\frac{2}{3}\boldsymbol{\varepsilon}_{ori} : \boldsymbol{\varepsilon}_{ori}], \end{aligned} \tag{A.24}$$

$$\boldsymbol{A}_{ori} = \boldsymbol{s}z - \frac{2}{3}z(\alpha z + \beta(1-z))\boldsymbol{\varepsilon}_{ori} - \frac{2}{3}\mu\left[\frac{\boldsymbol{\varepsilon}_{ori}}{\sqrt{\frac{2}{3}\boldsymbol{\varepsilon}_{ori} : \boldsymbol{\varepsilon}_{ori}}}\right], \tag{A.25}$$

$$\boldsymbol{A}_{pl} = \boldsymbol{s} - \frac{2}{3}H_1\boldsymbol{\varepsilon}_{pl}. \tag{A.26}$$

Dissipation pseudopotential:

A dissipation pseudopotential is defined as

$$D = \big[a(1-z)+bz\big]|\dot{z}| + z^2 Y_{ori}\sqrt{\frac{2}{3}\dot{\boldsymbol{\varepsilon}}_{ori} : \dot{\boldsymbol{\varepsilon}}_{ori}} + \big[(1-z)Y_{pl}^{A} + zY_{pl}^{M}\big]\sqrt{\frac{2}{3}\dot{\boldsymbol{\varepsilon}}_{pl} : \dot{\boldsymbol{\varepsilon}}_{pl}} \quad \text{(A.27)}$$

Limit functions:

Limit functions for the phase transformation and the plasticity are derived as follows:

The limit function for the forward phase transformation is

$$\begin{aligned} F_z^1 &= \frac{1}{2}\bigg(EL_{MA}\boldsymbol{s} : \boldsymbol{s} + (\frac{1}{3}EL_{MA} + P_{MA})tr(\boldsymbol{\sigma})^2\bigg) - C(T) + \boldsymbol{s} : \boldsymbol{\varepsilon}_{ori} - Gz - [\alpha z \\ &\quad +\beta(\frac{1}{2} - z)][\frac{2}{3}\boldsymbol{\varepsilon}_{ori} : \boldsymbol{\varepsilon}_{ori}] - [a(1-z)+bz] \leq 0. \end{aligned} \quad \text{(A.28)}$$

The limit function for the reverse phase transformation is

$$\begin{aligned} F_z^2 &= -\frac{1}{2}\bigg(EL_{MA}\boldsymbol{s} : \boldsymbol{s} + (\frac{1}{3}EL_{MA} + P_{MA})tr(\boldsymbol{\sigma})^2\bigg) + C(T) - \boldsymbol{s} : \boldsymbol{\varepsilon}_{ori} + Gz + [\alpha z \\ &\quad +\beta(\frac{1}{2} - z)][\frac{2}{3}\boldsymbol{\varepsilon}_{ori} : \boldsymbol{\varepsilon}_{ori}] - [a(1-z)+bz] \leq 0. \end{aligned} \quad \text{(A.29)}$$

The limit function for the martensite orientation is

$$\begin{aligned} F_{tr} &= \Big\|A_{ori}\Big\|_{VM} - z^2 Y_{ori} \\ &= \bigg\|\boldsymbol{s}z - \frac{2}{3}z(\alpha z + \beta(1-z))\boldsymbol{\varepsilon}_{ori} - \frac{2}{3}\mu\bigg[\frac{\boldsymbol{\varepsilon}_{ori}}{\sqrt{\frac{2}{3}\boldsymbol{\varepsilon}_{ori} : \boldsymbol{\varepsilon}_{ori}}}\bigg]\bigg\|_{VM} - z^2 Y_{ori}] \leq 0 \end{aligned} \quad \text{(A.30)}$$

The limit function for the plastic deformation is

$$\begin{aligned} F_{pl} &= \left\| A_{pl} \right\|_{VM} - \left[(1-z) Y_{pl}^{A} + z Y_{pl}^{M} \right] \\ &= \left\| \boldsymbol{s} - \frac{2}{3} H_1 \boldsymbol{\varepsilon}_{pl} \right\|_{VM} - \left[(1-z) Y_{pl}^{A} + z Y_{pl}^{M} \right] \leq 0. \end{aligned} \tag{A.31}$$

The limit function governing the martensite orientation is simplified as [15]

$$\begin{aligned} F_{ori} &= \frac{F_{tr}}{z} = \left\| \boldsymbol{A}_{ori} \right\|_{VM} - z Y_{ori} \\ &= \left\| \boldsymbol{s} - \frac{2}{3} (\alpha z + \beta (1-z)) \boldsymbol{\varepsilon}_{ori} - \frac{2}{3} \frac{\mu}{z} \left[\frac{\boldsymbol{\varepsilon}_{ori}}{\sqrt{\frac{2}{3} \boldsymbol{\varepsilon}_{ori} : \boldsymbol{\varepsilon}_{ori}}} \right] \right\|_{VM} - z Y_{ori}. \end{aligned} \tag{A.32}$$

Martensite is assumed to be completely oriented as soon as it is formed. In terms of modeling, it means

$$\varepsilon_0 = \sqrt{\frac{2}{3} \boldsymbol{\varepsilon}_{ori} : \boldsymbol{\varepsilon}_{ori}}. \tag{A.33}$$

In this case, the limit function for orientation is reduced to

$$F_{ori} = \left\| \boldsymbol{s} - \frac{2}{3 \varepsilon_0^2} (\boldsymbol{\sigma} : \boldsymbol{\varepsilon}_{ori}) \boldsymbol{\varepsilon}_{ori} \right\|_{VM} - z Y_{ori}. \tag{A.34}$$

Complementary laws:

The evolutions of $\boldsymbol{\varepsilon}_{ori}$ and $\boldsymbol{\varepsilon}_{pl}$ follow the normality rules as expressed in Equation

4.68 and 4.69, and the complete set of complementary laws are listed as

$$\dot{z} \geq 0, \quad F_z^1 \leq 0, \quad \dot{z}F_z^1 = 0, \tag{A.35}$$

$$\dot{z} \leq 0, \quad F_z^2 \leq 0, \quad \dot{z}F_z^2 = 0, \tag{A.36}$$

$$\eta \geq 0, \quad F_{ori} \leq 0, \quad \eta F_{ori} = 0, \tag{A.37}$$

$$\gamma \geq 0, \quad F_{pl} \leq 0, \quad \gamma F_{pl} = 0. \tag{A.38}$$

A.2.1. Numerical Implementation and Algorithmic Setup

Incremental formulation:

The phenomenological model is implemented into a user defined material subroutine (UMAT) using fortran programming language, similar to the procedure outlined in Chapter 4. The applied loading is divided into N increments; starting from the known initial state ($n = 0$), the problem is solved iteratively for $n = 1...N$ using elastic predictor-plastic corrector method (return mapping algorithm-RMA). The continuum problem is transformed into a discrete formulation using implicit backward-Euler integration scheme. The formulation is summarized below; n represents the increment number while (k) is for the iteration.

- Assume elastic increment and calculate trial stress as

$$\begin{aligned} z_{n+1}^{(0)} = z_n, \quad \boldsymbol{\varepsilon}_{n+1}^{ori(0)} = \boldsymbol{\varepsilon}_n^{ori}, \quad \boldsymbol{\varepsilon}_{n+1}^{pl(0)} = \boldsymbol{\varepsilon}_n^{pl}, \quad \boldsymbol{K}_{eqv}{}_{n+1}^{(0)} = \boldsymbol{K}_{eqv}{}_n, \\ \boldsymbol{\sigma}_{n+1}^{(0)} = \boldsymbol{K}_{eqv}{}_{n+1}^{(0)} : \left[\boldsymbol{\varepsilon}_{n+1} - z_{n+1}^{(0)}\boldsymbol{\varepsilon}_{n+1}^{ori(0)} - \boldsymbol{\varepsilon}_{n+1}^{pl(0)}\right]. \end{aligned} \tag{A.39}$$

- During elastic loading, limit functions must satisfy

$$F_z\left(\boldsymbol{\sigma}_{n+1}^{(k)}, z_{n+1}^{(k)}, \boldsymbol{\varepsilon}_{pl}^{(k)}{}_{n+1}, \boldsymbol{\varepsilon}_{ori\,n+1}^{(k)}\right) \leq 0, \tag{A.40}$$

$$F_{pl}\left(\boldsymbol{\sigma}_{n+1}^{(k)}, z_{n+1}^{(k)}, \boldsymbol{\varepsilon}_{pl}^{(k)}{}_{n+1}, \boldsymbol{\varepsilon}_{ori\,n+1}^{(k)}\right) \leq 0, \tag{A.41}$$

$$F_{ori}\left(\boldsymbol{\sigma}_{n+1}^{(k)}, z_{n+1}^{(k)}, \boldsymbol{\varepsilon}_{pl}{}_{n+1}^{(k)}, \boldsymbol{\varepsilon}_{ori\,n+1}^{(k)}\right) \leq 0. \tag{A.42}$$

When an inelastic deformation mechanism is active, its limit function reduces to an equality, and the stress increment must be corrected by calculating the increments of ISVs. To calculate the increments, the limit functions are approximated using first-order Taylor series expansions in the neighborhood of $\left(\boldsymbol{\sigma}_{n+1}^{(k-1)}, z_{n+1}^{(k-1)}, \boldsymbol{\varepsilon}_{pl}{}_{n+1}^{(k-1)}, \boldsymbol{\varepsilon}_{ori}^{(k-1)}{}_{n+1}\right)$ as

$$\begin{aligned} &F_z^{k-1} + \frac{\partial F_z}{\partial \boldsymbol{\sigma}}^{k-1} : \Delta\boldsymbol{\sigma}^k + \frac{\partial F_z}{\partial z}^{k-1} \Delta z^k + \frac{\partial F_z}{\partial \boldsymbol{\varepsilon}_{pl}}^{k-1} : \Delta\boldsymbol{\varepsilon}_{pl}^k \\ &+ \frac{\partial F_z}{\partial \boldsymbol{\varepsilon}_{ori}}^{k-1} : \Delta\boldsymbol{\varepsilon}_{ori}^k = 0, \end{aligned} \tag{A.43}$$

$$\begin{aligned} &F_{pl}^{k-1} + \frac{\partial F_{pl}}{\partial \boldsymbol{\sigma}}^{k-1} : \Delta\boldsymbol{\sigma}^k + \frac{\partial F_{pl}}{\partial z}^{k-1} \Delta z^k + \frac{\partial F_{pl}}{\partial \boldsymbol{\varepsilon}_{pl}}^{k-1} : \Delta\boldsymbol{\varepsilon}_{pl}^k \\ &+ \frac{\partial F_{pl}}{\partial \boldsymbol{\varepsilon}_{ori}}^{k-1} : \Delta\boldsymbol{\varepsilon}_{ori}^k = 0, \end{aligned} \tag{A.44}$$

$$\begin{aligned} &F_{ori}^{k-1} + \frac{\partial F_{ori}}{\partial \boldsymbol{\sigma}}^{k-1} : \Delta\boldsymbol{\sigma}^k + \frac{\partial F_{ori}}{\partial z}^{k-1} \Delta z^k + \frac{\partial F_{ori}}{\partial \boldsymbol{\varepsilon}_{pl}}^{k-1} : \Delta\boldsymbol{\varepsilon}_{pl}^k \\ &+ \frac{\partial F_{ori}}{\partial \boldsymbol{\varepsilon}_{ori}}^{k-1} : \Delta\boldsymbol{\varepsilon}_{ori}^k = 0. \end{aligned} \tag{A.45}$$

In equations above, the $n+1$ subscript is eliminated for better readability, and $\Delta\alpha^{(k)} = \alpha^{(k)} - \alpha^{(k-1)}$ is the increment of a variable α at iteration k.

The normality rules in discrete form can be written as

$$\Delta\boldsymbol{\varepsilon}_{pl}{}^{(k)} = \gamma^{(k)} \boldsymbol{N}_{pl}^{(k)}, \tag{A.46}$$

$$\Delta\boldsymbol{\varepsilon}_{ori}{}^{(k)} = \eta^{(k)} \boldsymbol{N}_{ori}^{(k)}, \tag{A.47}$$

where $\gamma^{(k)}$ and $\eta^{(k)}$ are the discrete inelastic multipliers used to express the discrete normality rules at iteration k. $\boldsymbol{N}_{pl}$ and $\boldsymbol{N}_{ori}$ are approximated at iteration k by their values at the previous iteration, with the initial values corresponding to an elastic prediction. Therefore,

$$F_z^{k-1} + \frac{\partial F_z}{\partial \boldsymbol{\sigma}}^{k-1} : \Delta\boldsymbol{\sigma}^k + \frac{\partial F_z}{\partial z}^{k-1} \Delta z^k + \gamma^k \frac{\partial F_z}{\partial \boldsymbol{\varepsilon}_{pl}}^{k-1} : \boldsymbol{N}_{pl}^{k-1}$$
$$+\eta^k \frac{\partial F_z}{\partial \boldsymbol{\varepsilon}_{ori}}^{k-1} : \boldsymbol{N}_{ori}^{k-1} = 0, \tag{A.48}$$
$$F_{pl}^{k-1} + \frac{\partial F_{pl}}{\partial \boldsymbol{\sigma}}^{k-1} : \Delta\boldsymbol{\sigma}^k + \frac{\partial F_{pl}}{\partial z}^{k-1} \Delta z^k + \gamma^k \frac{\partial F_{pl}}{\partial \boldsymbol{\varepsilon}_{pl}}^{k-1} : \boldsymbol{N}_{pl}^{k-1}$$
$$+\eta^k \frac{\partial F_{pl}}{\partial \boldsymbol{\varepsilon}_{ori}}^{k-1} : \boldsymbol{N}_{ori}^{k-1} = 0, \tag{A.49}$$
$$F_{ori}^{k-1} + \frac{\partial F_{ori}}{\partial \boldsymbol{\sigma}}^{k-1} : \Delta\boldsymbol{\sigma}^k + \frac{\partial F_{ori}}{\partial z}^{k-1} \Delta z^k + \gamma^k \frac{\partial F_{ori}}{\partial \boldsymbol{\varepsilon}_{pl}}^{k-1} : \boldsymbol{N}_{pl}^{k-1}$$
$$+\eta^k \frac{\partial F_{ori}}{\partial \boldsymbol{\varepsilon}_{ori}}^{k-1} : \boldsymbol{N}_{ori}^{k-1} = 0. \tag{A.50}$$

The equation set in A.48- A.50 is written in the array form for the ease of numerical implementation as follows

$$\begin{bmatrix} C_{11} & C_{12} & C_{13} \\ C_{21} & C_{22} & C_{23} \\ C_{31} & C_{32} & C_{33} \end{bmatrix} \begin{Bmatrix} \Delta z^k \\ \gamma^k \\ \eta^k \end{Bmatrix} = \begin{Bmatrix} -F_z^{k-1} \\ -F_{pl}^{k-1} \\ -F_{ori}^{k-1} \end{Bmatrix}, \tag{A.51}$$

where

$$C_{11} = -\boldsymbol{F}_{z,\sigma}^{k-1} : \boldsymbol{K}_{eqv}^{k-1} : \boldsymbol{R}^{k-1} + F_{z,z}^{k-1}, \tag{A.52}$$

$$C_{12} = -\boldsymbol{F}_{z,\sigma}^{k-1} : \boldsymbol{K}_{eqv}^{k-1} : \boldsymbol{N}_{pl}^{k-1} + \boldsymbol{F}_{z,\epsilon_{pl}}^{k-1} : \boldsymbol{N}_{pl}^{k-1}, \tag{A.53}$$

$$C_{13} = -\boldsymbol{F}_{z,\sigma}^{k-1} : \boldsymbol{K}_{eqv}^{k-1} : z\boldsymbol{N}_{ori}^{k-1} + \boldsymbol{F}_{z,\epsilon_{ori}}^{k-1} : \boldsymbol{N}_{ori}^{k-1}, \tag{A.54}$$

$$C_{21} = -\boldsymbol{F}_{pl,\sigma}^{k-1} : \boldsymbol{K}_{eqv}^{k-1} : \boldsymbol{R}^{k-1} + F_{pl,z}^{k-1}, \tag{A.55}$$

$$C_{22} = -\boldsymbol{F}_{pl,\sigma}^{k-1} : \boldsymbol{K}_{eqv}^{k-1} : \boldsymbol{N}_{pl}^{k-1} + \boldsymbol{F}_{pl,\epsilon_{pl}}^{k-1} : \boldsymbol{N}_{pl}^{k-1}, \tag{A.56}$$

$$C_{23} = -\boldsymbol{F}_{pl,\sigma}^{k-1} : \boldsymbol{K}_{eqv}^{k-1} : z\boldsymbol{N}_{ori}^{k-1} + \boldsymbol{F}_{pl,\epsilon_{ori}}^{k-1} : \boldsymbol{N}_{ori}^{k-1}, \tag{A.57}$$

$$C_{31} = -\boldsymbol{F}_{ori,\sigma}^{k-1} : \boldsymbol{K}_{eqv}^{k-1} : \boldsymbol{R}^{k-1} + F_{ori,z}^{k-1}, \tag{A.58}$$

$$C_{32} = -\boldsymbol{F}_{ori,\sigma}^{k-1} : \boldsymbol{K}_{eqv}^{k-1} : \boldsymbol{N}_{pl}^{k-1} + \boldsymbol{F}_{ori,\epsilon_{pl}}^{k-1} : \boldsymbol{N}_{pl}^{k-1}, \tag{A.59}$$

$$C_{33} = -\boldsymbol{F}_{ori,\sigma}^{k-1} : \boldsymbol{K}_{eqv}^{k-1} : z\boldsymbol{N}_{ori}^{k-1} + \boldsymbol{F}_{ori,\epsilon_{ori}}^{k-1} : \boldsymbol{N}_{ori}^{k-1}. \tag{A.60}$$

The time discrete stress-strain relation is obtained as

$$\Delta\boldsymbol{\sigma}^{k} = -\boldsymbol{K}_{eqv}^{k-1} : \left[\boldsymbol{R}^{k-1}\Delta z^{k} + \gamma^{k}\boldsymbol{N}_{pl}^{k-1} + z^{k-1}\eta^{k}\boldsymbol{N}_{ori}^{k-1}\right], \tag{A.61}$$

where

$$\boldsymbol{R}^{k-1} = \left(\left[\boldsymbol{K}_{M}^{-1} - \boldsymbol{K}_{A}^{-1}\right] : \boldsymbol{\sigma}^{k-1} + \boldsymbol{\varepsilon}_{ori}^{k-1}\right). \tag{A.62}$$

Therefore, Δz^{k}, γ^{k} and η^{k} can be calculated by using the available matrix operations in Fortran's mathematical library.

- A continuous material Jacobian is derived as

$$\boldsymbol{J}_{n+1} = \left(\frac{d\boldsymbol{\sigma}}{d\boldsymbol{\varepsilon}}\right)_{n+1}, \tag{A.63}$$

where the time-continuous stress–strain relation is

$$d\boldsymbol{\sigma} = \boldsymbol{K}_{eqv} : \left[d\boldsymbol{\varepsilon} - \boldsymbol{R}dz - \gamma\boldsymbol{N}_{pl} - z\eta\boldsymbol{N}_{ori}\right]. \tag{A.64}$$

The load increment must satisfy $dF_z = dF_{pl} = dF_{ori} = 0$. Therefore,

$$\frac{\partial F_z}{\partial \boldsymbol{\sigma}} : d\boldsymbol{\sigma} + \frac{\partial F_z}{\partial z} dz + \frac{\partial F_z}{\partial \boldsymbol{\varepsilon}_{pl}} : \gamma \boldsymbol{N}_{pl} + \frac{\partial F_z}{\partial \boldsymbol{\varepsilon}_{ori}} : \eta \boldsymbol{N}_{ori} = 0, \tag{A.65}$$

$$\frac{\partial F_{pl}}{\partial \boldsymbol{\sigma}} : d\boldsymbol{\sigma} + \frac{\partial F_{pl}}{\partial z} dz + \frac{\partial F_{pl}}{\partial \boldsymbol{\varepsilon}_{pl}} : \gamma \boldsymbol{N}_{pl} + \frac{\partial F_{pl}}{\partial \boldsymbol{\varepsilon}_{ori}} : \eta \boldsymbol{N}_{ori} = 0, \tag{A.66}$$

$$\frac{\partial F_{ori}}{\partial \boldsymbol{\sigma}} : d\boldsymbol{\sigma} + \frac{\partial F_{ori}}{\partial z} dz + \frac{\partial F_{ori}}{\partial \boldsymbol{\varepsilon}_{pl}} : \gamma \boldsymbol{N}_{pl} + \frac{\partial F_{ori}}{\partial \boldsymbol{\varepsilon}_{ori}} : \eta \boldsymbol{N}_{ori} = 0. \tag{A.67}$$

Using Equations A.65-A.67 together with Equation A.64, the Jacobian is derived as

$$\begin{aligned} \boldsymbol{J} =& \boldsymbol{K}_{eqv} - \Big(\boldsymbol{K}_{eqv} : \boldsymbol{R} \Big) \otimes \Big(C^{inv}(1,:) \boldsymbol{F} \Big) - \Big(\boldsymbol{K}_{eqv} : \boldsymbol{N}_{pl} \Big) \otimes \Big(C^{inv}(2,:) \boldsymbol{F} \Big) \\ & - z \Big(\boldsymbol{K}_{eqv} : \boldsymbol{N}_{ori} \Big) \otimes \Big(C^{inv}(3,:) \boldsymbol{F} \Big), \end{aligned} \tag{A.68}$$

where $\boldsymbol{C}^{inv}$ is the inverse of the coefficient matrix whose elements are provided above. And,

$$\boldsymbol{F} = \begin{Bmatrix} -\bar{\boldsymbol{K}}_{eqv} : \boldsymbol{F}_{z,\sigma} \\ -\bar{\boldsymbol{K}}_{eqv} : \boldsymbol{F}_{pl,\boldsymbol{\sigma}} \\ -\bar{\boldsymbol{K}}_{eqv} : \boldsymbol{F}_{ori,\boldsymbol{\sigma}} \end{Bmatrix}. \tag{A.69}$$

The algorithm of the numerical model is presented in Figure A.1.

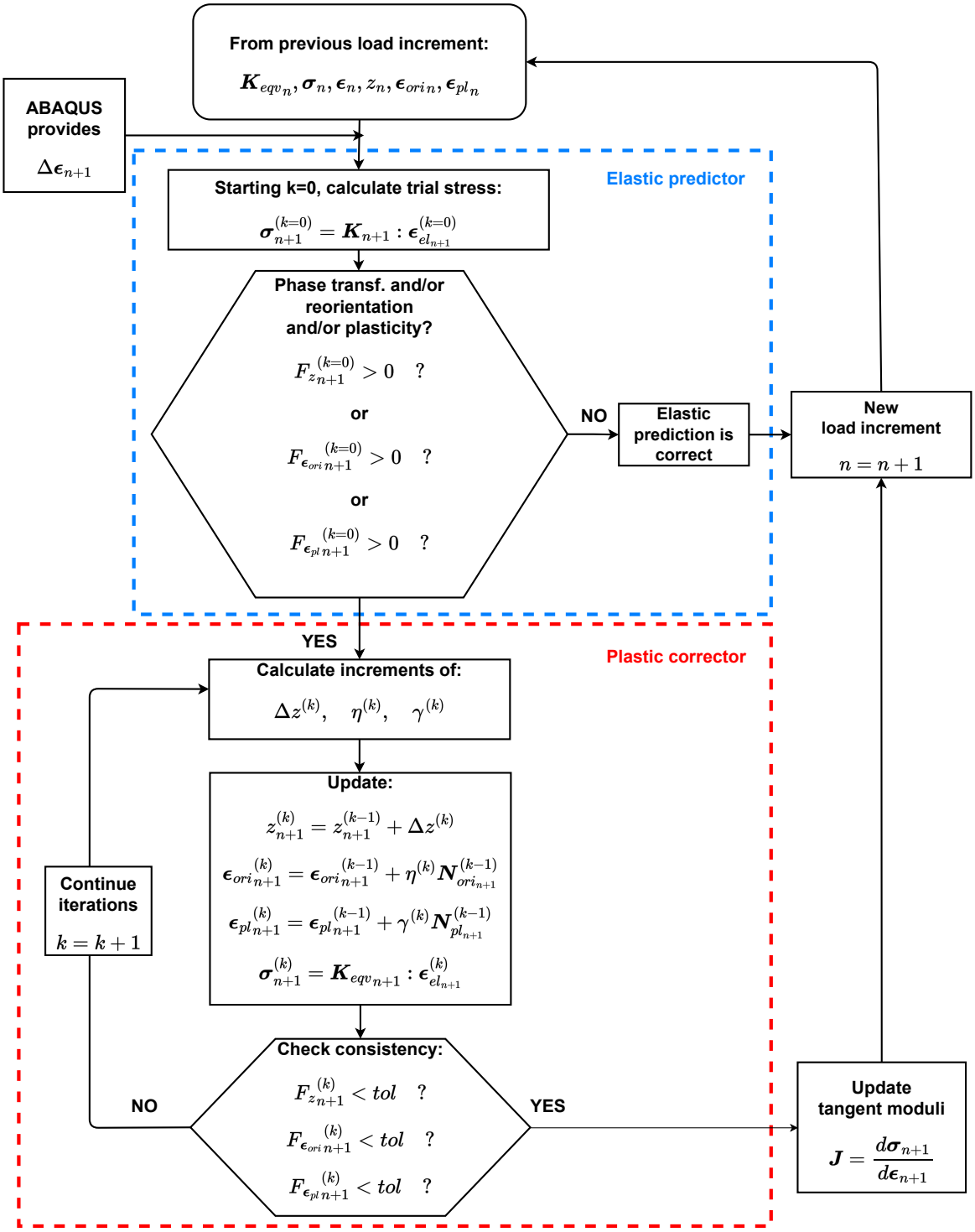

Figure A.1: Return mapping algorithm for UMAT used in dense SMA modeling.

A.3. Permission for Reuse

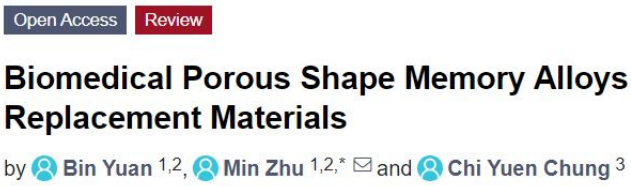

Figure A.2: Proof of permission for reuse for some figures from an open-access journal. Related Figures: 1.1, 1.2 and 1.6.a.

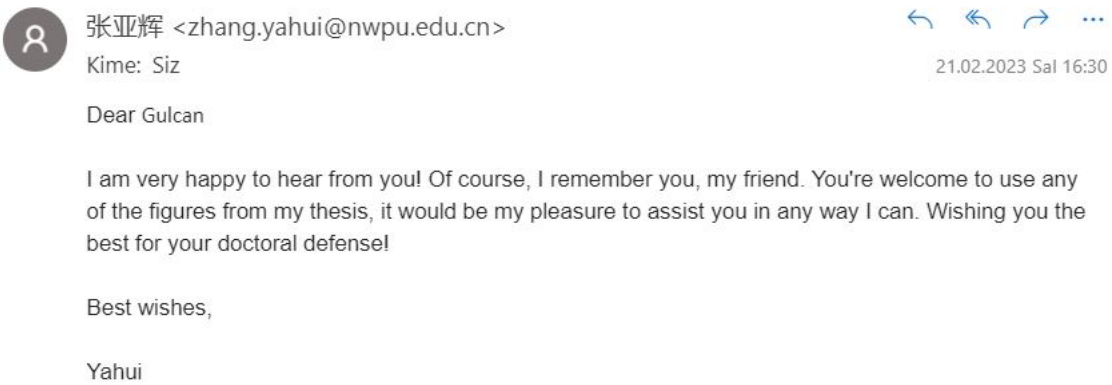

Figure A.3: Proof of permission for reuse for Figure 1.3.

ELSEVIER LICENSE
TERMS AND CONDITIONS

Feb 15, 2023

This Agreement between Boğaziçi University -- Gülcan Özerim Bekiloğlu ("You") and Elsevier ("Elsevier") consists of your license details and the terms and conditions provided by Elsevier and Copyright Clearance Center.

License Number	5490160388199
License date	Feb 15, 2023
Licensed Content Publisher	Elsevier
Licensed Content Publication	Acta Biomaterialia
Licensed Content Title	High strength, low stiffness, porous NiTi with superelastic properties

Figure A.4: Proof of permission for reuse for Figure 1.5.a.

ELSEVIER LICENSE
TERMS AND CONDITIONS

Feb 15, 2023

This Agreement between Boğaziçi University -- Gülcan Özerim Bekiloğlu ("You") and Elsevier ("Elsevier") consists of your license details and the terms and conditions provided by Elsevier and Copyright Clearance Center.

License Number	5490160569117
License date	Feb 15, 2023
Licensed Content Publisher	Elsevier
Licensed Content Publication	Journal of Alloys and Compounds
Licensed Content Title	Superelastic behaviors of biomedical porous NiTi alloy with high porosity and large pore size prepared by spark plasma sintering

Figure A.5: Proof of permission for reuse for Figures 1.5.b and 1.6.b.

ELSEVIER LICENSE
TERMS AND CONDITIONS

Feb 15, 2023

This Agreement between Boğaziçi University -- Gülcan Özerim Bekiloğlu ("You") and Elsevier ("Elsevier") consists of your license details and the terms and conditions provided by Elsevier and Copyright Clearance Center.

License Number	5490180701839
License date	Feb 15, 2023
Licensed Content Publisher	Elsevier
Licensed Content Publication	Progress in Materials Science
Licensed Content Title	Physical metallurgy of Ti–Ni-based shape memory alloys

Figure A.6: Proof of permission for reuse for Figure 2.4.

CCC Marketplace

This is a License Agreement between Boğaziçi University ("User") and Copyright Clearance Center, Inc. ("CCC") on behalf of the Rightsholder identified in the order details below. The license consists of the order details, the Marketplace Permissions General Terms and Conditions below, and any Rightsholder Terms and Conditions which are included below.

All payments must be made in full to CCC in accordance with the Marketplace Permissions General Terms and Conditions below.

Order Date	16-Feb-2023	Type of Use	Republish in a thesis/dissertation
Order License ID	1324633-1		
ISBN-13	9780470298114	Publisher	John Wiley & Sons
		Portion	Image/photo/illustration

LICENSED CONTENT

Publication Title	Poromechanics	Country	United Kingdom of Great Britain and Northern Ireland
Author/Editor	Coussy, Olivier		
Date	12/10/2007	Rightsholder	John Wiley & Sons - Books
Language	English	Publication Type	e-Book

Figure A.7: Proof of permission for reuse for Figure 4.1.